UNIVERSITY OF OKLAHOMA
GRADUATE COLLEGE

# Investigation of Surface Phonon Polariton Modes in 4H-SiC Structures

A DISSERTATION

SUBMITTED TO THE GRADUATE FACULTY

in partial fulfillment of the requirements for the

Degree of

DOCTOR OF PHILOSOPHY

By Nazli Rasouli Sarabi
Norman, Oklahoma
2025

INVESTIGATION OF SURFACE PHONON POLARITON MODES IN 4H-SiC STRUCTURES

A DISSERTATION APPROVED FOR THE

SCHOOL OF ELECTRICAL AND COMPUTER ENGINEERING

BY THE COMMITTEE CONSISTING OF

Dr. Joseph G. Tischler, Chair

Dr. Randa Shehab

Dr. Zhisheng Shi

Dr. Binbin Weng

*To my mother's boundless love, to Hadi, the love of my life, to Selen, the light of my days, and to the spirit of my father, whose presence lives on in every step I take.*

## Acknowledgments

I would like to begin by expressing my deepest gratitude to my advisor, Dr. Joseph Tischler, for his continuous guidance, encouragement, and support throughout my doctoral studies. His expertise, patience, and dedication have been a constant source of inspiration, and I feel truly fortunate to have had the opportunity to work under his mentorship.

I am also sincerely thankful to my committee members, Dr. Renda Shehab, Dr. Zhisheng Shi, and Dr. Binbin Weng, for their valuable advice, insightful comments, and kind support during the development of my dissertation. Their perspectives have greatly enriched this work.

I am grateful to the Gallogly College of Engineering for financial support through the Clyde L. Farrar Scholarship, William H. Barkow Scholarship, Nettie Vincent Boggs Scholarship, and P.H. Robinson Fellowship. I also wish to express my gratitude for the generous support of the Farzaneh family through the Farzaneh Scholarship. Additionally, I would like to thank the Department of Physics and Astronomy for providing travel grants that enabled me to attend conferences and present my research. My appreciation also extends to the School of Electrical and Computer Engineering (ECE), and especially to Dr. Hjalti Sigmarsson and Dr. Rodney C. Keele, for their kind help and support throughout my studies.

I would like to express my sincere thanks to Dr. Larson and the staff at the Noble Microscopy Lab for their expertise and assistance in material characterization. My gratitude also goes to the cleanroom staff, especially Dr. Gang Yang, for their training and support in device fabrication and characterization, which played a crucial role in the success of this research.

Beyond academics, I am thankful to all of my friends for their encouragement, kindness, and support, which made this journey more meaningful.

Most importantly, I am profoundly grateful to my family. To my husband, Hadi, for his unwavering love, patience, and support, and to my daughter, Selen, who has been my greatest source of joy and inspiration. To my parents, for their unconditional support throughout my life. I dedicate this dissertation to the memory of my beloved father, whose boundless love, sacrifices, and wisdom continue to illuminate my path. Though he is no longer with me, his spirit lives on in every achievement, and it is to him that I owe the strength to persevere.

Table of Contents

**List of figures**

## Abstract

One of the fundamental challenges in nanophotonics is the diffraction limit, which prevents light from being confined and controlled in dimensions smaller than about half its wavelength. This limitation has long been a serious limitation to achieving control of light at the nanoscale. One promising solution to overcome this problem is surface polaritons. These are hybrid excitations that arise from the interaction of photons with collective electronic or ionic oscillations in materials and allow light to be confined and guided in dimensions much smaller than the diffraction limit. Phonon-polaritons (PhPs) are hybrid photon-phonon waves found in polar dielectric materials. Unlike surface plasmons, surface phonon polaritons (SPhPs) have very low losses in the mid-infrared to terahertz range, without compromising their strong electromagnetic field confinement. The realization of nanoscale light control requires a detailed study of surface phonon polaritons (SPhPs), how they are excited, propagated, and interact with other excitations in solids. Despite all the progress in the field of nanoscale light control, many questions remain that indicate the need for further investigation of SPhPs. In this thesis, I investigate SPhPs in 4H-SiC and introduce a new method for detecting and reconstructing SPhP eigenmodes using confocal Raman microscopy. We show that, contrary to previous expectations, Raman-active phonons couple to localized SPhPs, allowing for the three-dimensional reconstruction of SPhP eigenmodes using visible and near-infrared light. This approach provides a powerful tool for imaging nanophotonic modes. While localized SPhPs have been extensively studied, the experimental observation of traveling SPhPs in isotropic nanostructured dielectric material has remained elusive. Here, I present and characterize traveling SPhPs in one-dimensional gratings, showing that their group velocity, propagation length, and confinement can be tuned through geometry. This discovery offers a new pathway for developing SPhP-based interconnects in nanophotonic circuitry. Finally, this dissertation investigates the interaction between free carriers and optical phonons in doped 4H-SiC epitaxial layers. While the coupling of longitudinal optical phonons (LO) with plasmons in polar semiconductors is well known and widely studied in the scientific literature, the results obtained from the Raman studies of this research reveal a new and unreported phenomenon.

Specifically, it was observed that by changing the doping concentration in 4H-SiC epitaxial layers, the frequency of the phonon mode $E_1$(TO) undergoes a shift. This result is against the common understanding that transverse optical phonons are unable to couple with free carriers. The discovery of this phenomenon not only challenges the conventional idea but also opens new opportunities for controlling the phonon–electron interaction in polar semiconductors. Such a capability could enable the development of new concepts in engineering the optical and electronic responses of materials at the nanoscale. These findings advance the fundamental physics of light-matter interactions and open new opportunities for designing next-generation nanophotonic devices in sensing, communications, and quantum technologies.

# Chapter 1

## Motivation for Nanoscale Light Manipulation

Conventional optical devices play a key role in scientific and technological advancements, enabling major progress in fields like microscopy, telecommunications, and medical imaging. Their applications range from showing microscopic biological structures to supporting global data transmission and enhancing precision in different optical systems. Despite many advancements in optical technology that have enhanced our understanding and improved our capabilities, conventional optical devices face considerable challenges in overcoming Abbe's diffraction limit.

The Abbe diffraction limit constrains the resolution of optical systems. According to Ernst Abbe's findings in 1873, the minimum achievable resolution of an optical device is determined by the wavelength of the incident light and is given by [1]:

$$d = \frac{\lambda}{2NA} \qquad 1.1$$

where d is the smallest observable feature size, λ is the wavelength of light, and NA is the numerical aperture of the optical system. Based on this equation, visible light, with wavelengths ranging from 400 nm to 700 nm, enables optical microscopes to resolve objects on the micrometer scale, like cells and bacteria. But for smaller objects like proteins or viruses, optical systems do not have the required resolution to clearly visualize them.

This equation also suggests that as the wavelength increases, the resolution decreases, making it difficult to achieve nanoscale precision, particularly in the infrared (IR) range. In the mid-infrared (Mid-IR) and far-infrared (Far-IR) regions, where wavelengths range from a few micrometers to several tens of micrometers, conventional optical systems fail to resolve nanoscale features. This

limitation presents a major challenge for applications that need high spatial resolution, like sub-wavelength imaging, on-chip optical circuits, and nanophotonic sensors.

The main goal of nanophotonics is to overcome this limitation by enabling the confinement and manipulation of light at the nanoscale [2-4]. In recent decades, advancements in optical engineering have resulted in the development of compact and high-performance optical devices that can be used in single-molecule sensing[5, 6], quantum computing[7], nanoscale imaging[8], and more.

Research in the naophotonics area is mostly focused on the visible range, and technology has advanced significantly in this spectral region; however, the infrared (IR) region has remained largely unexplored. The main challenge for the limited research in this frequency range is the need to achieve extremely small length scales in the IR region, as shown in Equation 1. However, during the past decade, scientists have shown more interest in the IR region because of its importance for applications in military, health care, and industry (like chemical sensing, spectroscopy, communications, and thermal imaging), making progress in this field crucial.

Although some research has been done in this area in the last few years, it is still a very hot topic with many challenges that need to be explored. This is the reason I am focusing on the mid-IR region for my thesis, to develop new approaches that address existing limitations.

## 1.1 Surface Plasmon Polaritons:

Researchers have studied different ways to overcome the diffraction limit and achieve nanoscale control of light. Plasmon polaritons can be considered as a solution to this problem that has received a lot of attention. Surface plasmon polaritons (SPPs) are electron density waves that are formed by the coupling of incident light with electron oscillation[9, 10]. These hybrid light-matter excitations happen when photons of light interact with the collective oscillations of free electrons at the interface between materials with opposite permittivities, such as metal ($\varepsilon < 0$) and air ($\varepsilon > 0$). SPPs propagate along the interface with a much shorter wavelength than the incident light,

which enables the sub-wavelength confinement of electromagnetic waves. This property makes it possible to create ultra-compact photonic devices, plasmonic waveguides, and highly sensitive biosensors. By engineering the metal-dielectric interface, researchers can improve SPP propagation length, confinement, and interactions with optical elements[11, 12]. Metals show high reflectivity at frequencies below the plasma frequency, which happens due to the coherent oscillation of electrons opposing the incident electromagnetic (EM) field. This results in negative permittivity, a property required for the excitation of surface polaritons. However, at longer wavelengths, metals show extremely high negative permittivity. This limits their practical application mainly to the visible and near-infrared (NIR) regions[13, 14]. Moreover, plasmons are based on the coupling of free carriers with light, and the electron scattering time is typically within 10–100 femtoseconds (fs)[15-17]. Shorter lifetimes of polariton modes result in higher losses, which is a major drawback for plasmonic materials.

## 1.2 Surface Phonon Polariton:

Polar dielectrics solve the problem of high losses in plasmonic materials. Polar dielectrics achieve sub-diffraction confinement by coupling the vibration of atoms to long-wavelength incident fields, rather than using free carriers like metals. This results in sub-diffraction confinement with significantly lower losses in the mid-infrared (Mid-IR) and far-infrared (Far-IR) spectral ranges. This frequency range has many applications, such as medical imaging, infrared detectors, and imaging through opaque objects[18].

Surface phonon polaritons (SPhPs) are surface waves that result from the interaction between polar dielectric phonons and incident light in the mid-IR to far-IR spectral range[18, 19]. These SPhP modes can only be excited within the frequency range between the transverse optical (TO) and longitudinal optical (LO) phonons, known as the Reststrahlen band[20].

As discussed in the earlier discussion on SPP, a basic requirement for exciting surface polariton modes is the presence of materials with negative permittivity. Polar dielectrics in the Reststrahlen

band behave like metals and enable the excitation of surface polaritons. The Reststrahlen band is defined by the frequency range between the TO and LO phonon modes, where TO phonons correspond to atomic vibrations with wave vectors perpendicular to the incident field and LO phonons correspond to vibrations parallel to the field. In the Reststrahlen band, the electron cloud in polar covalent bonds becomes asymmetrically distributed between atoms, causing a charge separation between adjacent atoms. This results in one atom behaving as a negatively charged ion and the other as a positively charged ion. The interaction of incident light with the polar dielectric surface causes the positively charged ions to move in its direction and the negatively charged ions move in the opposite direction. This screening effect induces near-total reflectivity and negative permittivity in the Reststrahlen band, thereby enabling the excitation of low-loss surface waves.

For example, in silicon carbide (SiC), a polar dielectric used in this dissertation, silicon atoms behave like positively charged ions and carbon atoms act as negatively charged ions. The Reststrahlen band for SiC is shown in Figure 2.1, highlighting the frequency range between the TO and LO phonon modes where this behavior occurs.

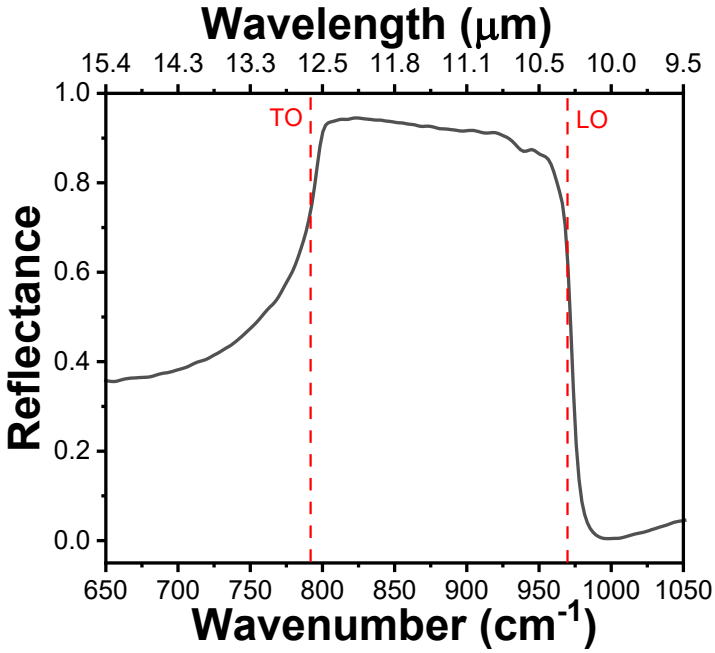

*Figure 1.1.1 Reststrahlen band of 4H-SiC, indicating TO and LO phonon modes.*

Since the scattering of the phonons, which happens on the order of a few picoseconds, determines the optical losses of surface polariton modes, this results in higher lifetimes of the phonon modes and significantly reduces losses compared to plasmonic materials. This allows for the excitation of surface waves with lower loss and higher quality factors[21-23]. Hence, polar dielectrics are promising candidates for nanophotonic applications in the Mid-IR to THz range offering better performance in sensing, imaging, and optical field confinement.

## 1.3 Crystal structure of SiC

As previously mentioned, SiC is a polar dielectric that can support surface phonon polaritons (SPhPs), and in this thesis, I focus specifically on 4H-SiC. In this section, I will discuss the properties and structure of SiC in more detail.

Silicon carbide (SiC) is a ceramic compound made up of silicon (Si) and carbon (C) atoms with hardness and thermal stability. One of the properties of SiC is that it keeps its structural strength even at temperatures above 1000°C. Wide-bandgap and indirect-bandgap nature of SiC provides outstanding electronic properties, making it ideal for use in electronic and optoelectronic applications. SiC with electrical properties such as high electron mobility, strong electrical conductivity, and high breakdown voltages is a good candidate for devices that need to perform effectively in high-temperature and high-power settings. SiC-based devices can support high current densities with little need for cooling. They can be used in applications like UV photodetectors, high-power Schottky diodes, RF and microwave devices, and several other purposes in electronic devices [24, 25].

The crystal structure of SiC, as shown in Fig. 1, has a tetrahedral arrangement, where each carbon (C) atom is bonded to four silicon (Si) atoms, or each silicon atom is bonded to four carbon atoms.

Polytypism is a property of SiC, meaning it can crystallize in different structural forms while keeping the same chemical composition. SiC has more than 200 known polytypes, each with a different stacking order along the c-axis. All SiC polytypes are made up of closely packed planes of Si-C bilayers, but variations in the stacking order of these bilayers create different polytypes. There are three possible stacking positions for these atomic layers, labeled A, B, and C, which determine the final crystal structure. The most common SiC polytypes are 3C-SiC, 2H-SiC, 4H-SiC, and 6H-SiC. In this notation, the letter shows the crystal system (C for cubic, H for hexagonal), and the number represents the number of Si-C bilayers per unit cell. In the basal plane, all polytypes have the same atomic arrangement; the main difference is in the stacking sequence along the c-axis, which impacts their electronic band structure, phonon dispersion, and other physical properties[26, 27].

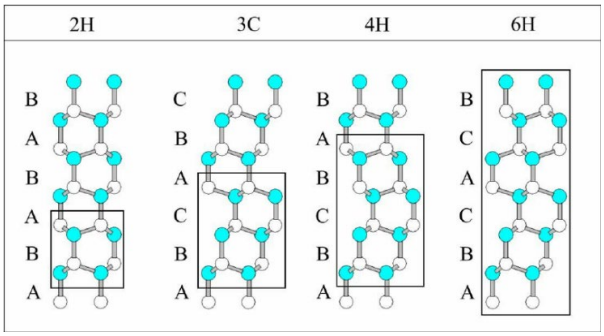


*Figure 1.2.1. Four common polytypes of SiC*

4H-SiC is often preferred for high-power semiconductor applications because of its greater electron mobility along the c-axis and higher breakdown field compared to 6H-SiC. In this study, I used 4H-silicon carbide (SiC) because it is an exceptional material for SPhP applications. It has a wide Reststrahlen (RS) band and low energy losses [2]. Also, the RS band is less complex in 4H SiC because it has only one zone-folded phonon, and this characteristic simplifies the analysis of phonon behavior in a 1D grating structure, as well as the study of their coupling to bulk modes, which will be explained in detail in the following chapters.

## 1.4 Dissertation Overview

In this research, I study surface phonon polaritons in silicon carbide (SiC) using different experimental techniques and theoretical models. This work focuses on new possibilities for nanophotonic applications in areas such as chemical sensing and optical components. Chapter 2 explains the theoretical basis for the interaction of electromagnetic waves with surface waves, beginning with the Maxwell equations. This is the fundamental theory that explains surface wave propagation. Then, it discusses Fourier spectroscopy, a method for analyzing surface wave spectral characteristics. The theory of Raman scattering and a detailed analysis of phonon modes in SiC are also introduced in this section. These theories are important for understanding the material's vibrational modes and their impact on polariton propagation.

Chapter 3 explains the experimental and simulation techniques used to study phonon polaritons in SiC. In this study, I used Fourier-transform infrared (FTIR) spectroscopy and Raman spectroscopy to investigate the light-matter interaction. I explain the importance of these techniques in probing material properties at smaller scales. This section also explains the fabrication process of one-dimensional (1D) gratings using two-photon polymerization lithography and the reactive ion etching (RIE) process. For the simulation part of this work, I used finite element method software COMSOL Multiphysics to simulate the far-field reflection spectrum. In this section, the simulation setup and the modulation used will be explained.

In Chapter 4, we used confocal Raman microscopy for mapping surface phonon polaritons (SPhPs) in nanostructures of indium phosphide (InP) and 4H-silicon carbide (4H-SiC). This work showed unexpected coupling between Bulk Raman modes and Surface phonon polariton modes. These findings suggest that Confocal Raman microscopy enables the non-destructive mapping of surface phonon polariton modes.

Chapter 5 studies the behaviour of different surface phonon polariton modes in 1D gratings and shows the appearance of a traveling mode in the structure. By studying the effect of grating

parameters on the propagation length and confinement of SPhP modes along the surface, we find new ways for controlling the flow of light at the nanoscale. These findings can be applied to the design of nanophotonic devices, such as sensors and waveguides.

In Chapter 6, I analyze the electron-phonon coupling in SiC, with a focus on the transverse optical phonon mode with E2 symmetry. The analysis indicates unusual coupling behavior that may result in new interactions between electrons and phonons, potentially improving the performance of optoelectronic devices. To gain a better understanding of electron-phonon interactions in materials like SiC, this chapter shows theoretical models and experimental findings.

The last chapter provides a brief conclusion for this thesis and discusses the importance of the research. It also presents future directions in nanophotonics and potential advancements in the field.

# Chapter 2

## 2.1 Phonons in polar crystals

In the following part, I want to briefly review phonons and talk about acoustic and optical phonons. Phonons are quantized vibrations of atoms in a crystal. They come from the collective oscillations of atoms about their equilibrium positions, held in place by interatomic forces. When atoms in a solid are moved from their equilibrium place, they experience restoring forces that cause them to vibrate at specific frequencies—these are the phonon modes. There are 2 types of phonons in a crystal: Acoustic and optical phonons. In a crystal with N atoms, there are 3 acoustic modes and 3N-3 optical modes. In acoustic modes, all atoms move coherently related to their equilibrium position. They oscillate together in the same direction, much like sound waves propagating through a material. If these motions are in the wave propagation direction, it is called longitudinal acoustic (LA) modes, and if the motion of the atoms is perpendicular, it is called transversal acoustic (TA) modes.

In optical modes, unlike acoustic modes, the movement of the atoms in the basis of the crystal lattice is out of phase with each other. Typically, atoms of different types (such as positive and negative ions) oscillate in opposite directions. Depending on the symmetry and bonding properties of the material, some of these vibrational modes result in temporary dipole moments. These modes are known as infrared-active phonons and can interact with incident electromagnetic waves, particularly within the mid- to far-infrared spectral range (typically 10–1000 $cm^{-1}$). This ability to couple with light is why these modes are known as "optical."

In optical modes, unlike acoustic modes, the atoms within the basis of the crystal lattice move out of phase with each other. Typically, atoms of different types (such as positive and negative ions) oscillate in opposite directions. Depending on the material's symmetry and bonding characteristics, some of these vibrational modes can form temporary dipole moments. These modes, which are infrared-active phonons, can couple with incoming electromagnetic waves, particularly in the mid-

to far-infrared spectral range (typically 10–1000 $cm^{-1}$). This ability to couple with light is why these modes are referred to as "optical."

Similar to acoustic modes, optical modes can also be classified as transverse or longitudinal, based on the direction of atomic vibration relative to wave propagation. In longitudinal optical (LO) modes, the induced dipoles oscillate along the direction of propagation, whereas in transverse optical (TO) modes, the dipoles oscillate perpendicular to it. Since electromagnetic waves in free space are purely transverse, they couple more efficiently with TO phonons than with LO phonons. Nevertheless, both TO and LO phonons can be infrared active. LO modes, in particular, play a crucial role in the infrared response of polar crystals, where differences in atomic size or electronegativity introduce polarity into the bonds, leading to phenomena such as LO-TO splitting.

Analyzing the phonon dispersion plot shown in Figure 2.1, we observe that the acoustic modes exhibit zero frequency at the Γ point (the center of the Brillouin zone). This means that at the Γ point, acoustic phonons represent all the atoms moving together without creating a traveling wave. In contrast, optical modes maintain a nonzero frequency at the Γ point, reflecting the relative vibrations between at least two different atoms within the unit cell.

In polar crystals, a frequency gap can be seen between the longitudinal optical (LO) and transverse optical (TO) modes at the Γ point. The LO mode is found at a higher frequency than the TO mode. This splitting is because of the creation of microscopic dipole moments within the crystal. In the LO mode, atoms vibrate in opposite directions along the direction of wave propagation, producing internal electric fields. These fields make it harder for the atoms to keep vibrating, so a stronger restoring force is needed. In comparison, in TO modes, the atomic vibrations are perpendicular to the propagation direction, so this additional electric field does not affect them.

This frequency gap is known as the Reststrahlen band and is characteristic of polar dielectrics. In nonpolar crystals, on the other hand, no intrinsic dipoles are formed between atoms. Therefore, no such splitting happens, and the LO and TO modes are degenerate.

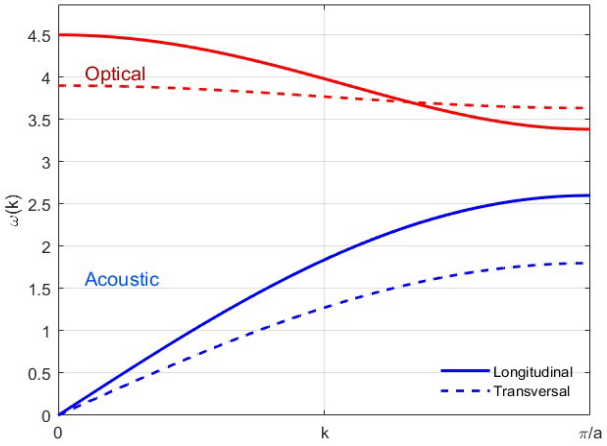


*Figure 2.1 Phonon dispersion of a diatomic lattice, illustrating acoustic (blue) and optical (red) branches. Solid and dashed lines correspond to longitudinal and transverse modes, respectively.*

## 2.2 Maxwell's equation for Surface phonon polariton

In this section, we explore surface phonon polaritons (SPhPs), focusing on their fundamental nature, dispersion characteristics, and propagation behavior in polar dielectric materials.

SPhP are coupled modes of an oscillating surface dipole and a photon, which result in a highly confined electromagnetic wave, propagating along the interface between two distinct materials. Surface dipole excitation is shown in Figure 2.2.

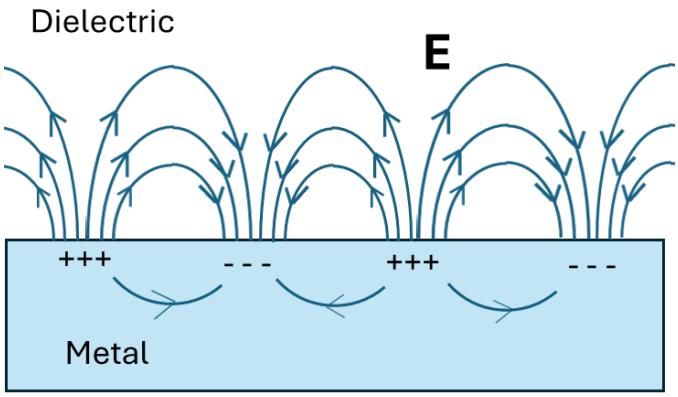


*Figure 2.2 Surface dipole excitation at the metal–air interface with the associated electric field distribution.*

At the interface between two materials, the incident electromagnetic field causes the polarization to oscillate, resulting in the oscillation of charge density. These oscillating charges create an electric field in the direction opposing the incoming wave. This electric field penetrates into both materials near the interface but decays exponentially as it moves away from the surface. Coupling of incoming light with the surface dipole oscillations results in the excitation of surface phonon polaritons (SPhPs) at the material interface. The electric field of the SPhP lies in the x-z plane, with no field component in the y direction. As a result, it can only be excited by waves with an electric field in the x-z plane. In this case, the magnetic field is directed along the y-axis, and excitation can only occur with P-polarized light. As shown in [28, 29], S-polarized light cannot excite any SPhP modes. In the following, this will be demonstrated by solving Maxwell's equations[29]. We begin by applying Maxwell's equations to a flat interface between a polar dielectric with negative permittivity and a dielectric with positive permittivity. By solving the wave equation for each medium and applying the boundary conditions, we can explain how these modes are excited and determine the conditions necessary for the existence of surface phonon polariton modes. Furthermore, this analysis helps determine the mode's confinement and propagation length along the interface between two materials with permittivities of opposite signs.

In the absence of free charges and currents, Maxwell's equations reduce to:

$$\nabla . \boldsymbol{D} = 0 \qquad 2.1$$

$$\nabla . \boldsymbol{B} = 0 \qquad 2.2$$

$$\nabla \times \boldsymbol{E} = -\frac{\partial \boldsymbol{B}}{\partial t} \qquad 2.3$$

$$\nabla \times \boldsymbol{H} = -\frac{\partial \boldsymbol{D}}{\partial t} \qquad 2.4$$

Assuming linear, isotropic media, we relate the fields through:

$$\boldsymbol{D} = \varepsilon \boldsymbol{E} \, , \boldsymbol{B} = \mu \boldsymbol{H} \qquad 2.5$$

We begin by deriving the electromagnetic wave equation. Taking the curl of Eq.2.3, and using Eq.2.4, we get:

$$\nabla \times (\nabla \times \boldsymbol{E}) = -\mu_0 \frac{\partial^2 \boldsymbol{D}}{\partial t^2} \qquad 2.6$$

Using the vector identity $\nabla \times (\nabla \times \boldsymbol{E}) = \nabla(\nabla \boldsymbol{E}) - \nabla^2 \boldsymbol{E}$ and assuming no external excitation $\nabla . \boldsymbol{D} = 0$, this simplifies to:

$$\nabla^2 \boldsymbol{E} - \mu_0 \varepsilon \frac{\partial^2 \boldsymbol{E}}{\partial t^2} = 0 \qquad 2.7$$

We need to solve this equation separately for the two media, ensuring that the boundary conditions at the interface are satisfied.

Assuming the electric field has a harmonic time dependence: $\boldsymbol{E}(\boldsymbol{r}, t) = \boldsymbol{E}(\boldsymbol{r}) e^{-i\omega t}$, Eq. 2.7 becomes:

$$\nabla^2 \boldsymbol{E} + \varepsilon \mu_0 \omega^2 \boldsymbol{E} = 0 \qquad 2.8$$

Defining $k_0 = \frac{\omega}{c}$, the free space wave number, we write:

$$\nabla^2 \boldsymbol{E} + k_0^2 \varepsilon \boldsymbol{E} = 0 \qquad 2.9$$

we consider a planar interface at $z = 0$ between a dielectric ($z > 0$) and a metal ($z < 0$). We assume wave propagation in the x-direction and there's no variation in the y-direction, so the dielectric constant depends only on z: $\varepsilon = \varepsilon(z)$. The wave equation for this configuration is as follows:

$$E(x, y, z) = E(z) e^{i k_x x} \qquad 2.10$$

where $k_x$ is the propagation constant along $x$ and describes how the wave travels along the interface. By replacing the electric field expression in Eq.2.9, we obtain the following form of the wave equation:

$$\frac{\partial^2 E(z)}{\partial z^2} + \left(k_0^2 \varepsilon - {k_x}^2\right) E = 0 \qquad 2.11$$

Maxwell's equations support two polarization modes: transverse magnetic (TM) and transverse electric (TE). For TM (p-polarized) modes, the nonzero field components are $E_x, E_z$ , and , $H_y$ and the equations governing the magnetic field component $H_y$ are:

$$E_x = -i \frac{1}{\omega \varepsilon_0 \varepsilon} \frac{\partial H_y}{\partial z} \qquad 2.12$$

$$E_z = \frac{-k_x}{\omega \varepsilon_0 \varepsilon} H_y \qquad 2.13$$

And the wave equation for $H_y$ becomes:

$$\frac{\partial^2 H_y}{\partial z^2} + \left(k_0^2 \varepsilon - {k_x}^2\right) H_y = 0 \qquad 2.14$$

We solve this equation in both media and apply boundary conditions for $H_y$ and $\varepsilon_i E_z$ at the interface. The complete calculation can be found in [10]. These continuity conditions yield:

$$A_1 = A_2 \; and \; \frac{k_2}{k_1} = -\frac{\varepsilon_2}{\varepsilon_1} \qquad 2.15$$

This result indicates that the existence of confined surface waves requires the two media to have permittivities of opposite sign: one with a negative real permittivity and the other with a positive real permittivity. For SPhPs, this condition is satisfied in polar dielectrics within the Reststrahlen band, where $Re(\varepsilon_1) < 0$ and $\varepsilon_2 > 0$. In the following, we will derive the dielectric function of a polar dielectric to explain the origin of its negative permittivity in this spectral range.

From the boundary conditions, the dispersion relation for SPhPs at the interface becomes:

$$k_{sphp} = k_x = k_0 \sqrt{\frac{\varepsilon_1 \varepsilon_2}{\varepsilon_1 + \varepsilon_2}} \qquad 2.16$$

Now, we want to take a look at TE mode to see if this mode can excite SPhP modes. We apply the same continuity condition at the interface this time for $E_y \; and \; Hx$ . This results in the following equation:

$$A_1 = A_2, \; A_1(k_1 + k_2) = 0 \qquad 2.17$$

To achieve field confinement, the electromagnetic wave must decay exponentially away from the interface in both media. This requires the real parts of the normal wavevector components, $Re(k_1) \; and \; Re(k_2)$, to be positive. Applying this condition to the Eq.2.17, yields only $A_1 = 0$, which indicates that no confined surface wave can exist. Therefore, only TM modes can support surface phonon polaritons.

## 2.3 Dielectric function

In polar dielectric materials, the interaction between the electromagnetic field and the lattice vibrations plays a crucial role in determining the optical response in the infrared spectral range. Unlike nonpolar dielectrics, polar materials have ionic bonds. During atomic vibrations, these bonds cause a separation of positive and negative charges, which generates dipole moments. These oscillating dipoles can strongly couple to the incident light in the frequencies range between the transverse and longitudinal optical phonons. This behavior is described by the dielectric function of the material, which is modeled using the Lorentz oscillator model. The Lorentz model connects the optical phonon frequencies to the dielectric constants of the material at low and high frequencies.[30]

$$\boldsymbol{E}q = m\omega_0^2\boldsymbol{r}_0^2 + m\Gamma\boldsymbol{r}_0' + m\boldsymbol{r}_0'' \qquad 2.18$$

In this equation, q represents the atomic charge, m the mass of the atom, $\omega_0$ the resonance frequency, $\boldsymbol{r}$ the displacement from equilibrium, and $\Gamma$ the damping constant. This equation shows the response of the atoms to an external electric field, considering the restoring force from their resonance frequency and the damping effect caused by energy loss. Supposing that the displacement of a bound charge oscillates at the same frequency as the electric field, the induced dipole moment per atom is:

$$\boldsymbol{p}(t) = \alpha(\omega)\boldsymbol{r_0} \qquad 2.19$$

$\alpha(\omega)$is the frequency-dependent polarizability of the atoms, and it relates the microscopic displacement to the applied electric field. From the driven damped harmonic oscillator model, the polarizability is given by:

$$\alpha(\omega) = \frac{q^2}{m\varepsilon_0(\omega_0^2 - \omega^2 - i\Gamma\omega)} \qquad 2.20$$

Using the relations $\varepsilon = 1 + \chi$ and $\chi = N\alpha(\omega)$ , where N is the number of oscillating atoms, we can express the electric permittivity as follows:

$$\varepsilon(\omega) = 1 + N \propto (\omega) = 1 + N\frac{q^2}{m\varepsilon_0(\omega_0^2 - \omega^2 - i\Gamma\omega)} \qquad 2.21$$

To account for contributions from higher-frequency electronic polarizability, the dielectric constant at high frequencies $\varepsilon_\infty$ is added. This gives the final expression:

$$\varepsilon(\omega) = \varepsilon_\infty + N\frac{q^2}{m\varepsilon_0(\omega_0^2 - \omega^2 - i\Gamma\omega)} \qquad 2.22$$

This expression describes how the material's permittivity varies with frequency due to atomic-scale interactions with the field. From Maxwell's equations, and $\nabla \cdot \boldsymbol{D} = 0$ and assuming a plane wave $\boldsymbol{D} = \varepsilon \boldsymbol{E_0} e^{i(\boldsymbol{kr} - \omega t)}$, we get:

$$\varepsilon(\boldsymbol{k}.\boldsymbol{E}) = 0 \qquad 2.23$$

This condition is satisfied when either $k \perp E$ or $\varepsilon = 0$. The first case means the electric field is perpendicular to the direction of wave propagation, which is true for transverse waves and transverse optical (TO) phonon modes. Because of this, TO modes can interact with the electric field and appear as a peak in the dielectric function, making them infrared active.

When $\varepsilon = 0$, this condition corresponds to a longitudinal wave, which occurs at the longitudinal optical (LO) phonon frequency, i.e., $\varepsilon(\omega_{L_0}) = 0$. By applying these conditions and setting the damping constant to zero, Eq.2.22 becomes:

$$(\omega_{L0}^2 - \omega_{TO}^2)\varepsilon_\infty = \frac{Nq^2}{m\varepsilon_0} \qquad 2.24$$

This equation connects the LO and TO phonons through the material constant. Substituting Eq. 2.24 into Eq. 2.23 gives the following expression for the dielectric function of a polar crystal.

$$\varepsilon(\omega) = \varepsilon_{\infty} \frac{\omega^2 - \omega_{LO}^2 - i\Gamma\omega}{\omega^2 - \omega_{TO}^2 - i\Gamma\omega} \qquad 2.25$$

This equation describes the permittivity of polar crystals. The dielectric permittivity for SiC is plotted in Figure 2.3 , showing a negative real part between $\omega_{TO}$ and $\omega_{LO}$ (the Reststrahlen band), enabling SPhP excitation.

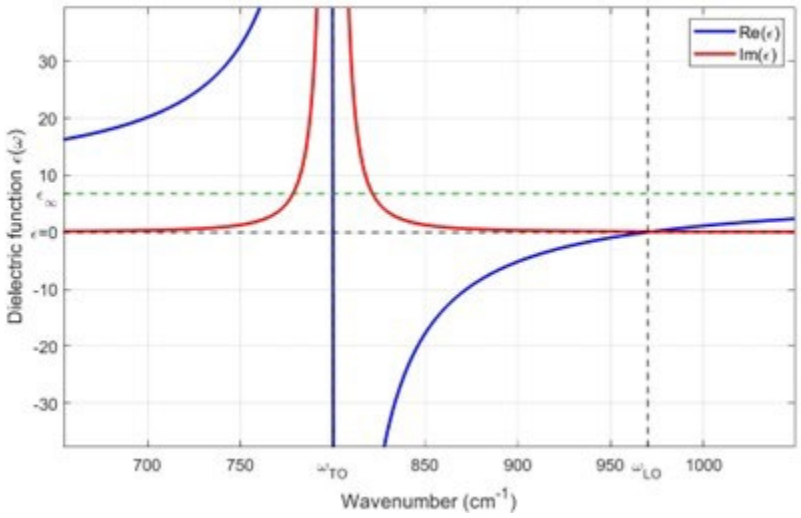


*Figure 2.3 Dielectric function of 4H-SiC in the Reststrahlen region.*

## 2.4 Dispersion Relation of Surface Phonon Polaritons:

To better understand the nature of surface phonon polaritons, the dispersion relation is examined in more detail. The dispersion is plotted based on Eq.2.16, assuming a lossless dielectric medium. In this plot, the blue curve shows how the normalized in-plane wavevector $k/k_0$ varies with

frequency. The red and green dashed lines represent the transverse optical (TO) and longitudinal optical (LO) phonon frequencies, $\omega_{TO}$ $and$ $\omega_{LO}$, respectively. The black dashed line indicates the light line, defined by $k = k_0$.

SPhP modes only exist in the frequency range between $\omega_{TO}$and $\omega_{LO}$, where the dielectric permittivity becomes negative. This range is known as the Reststrahlen band, a region in which strong coupling between electromagnetic waves and optical phonons occurs. In this band, by increasing the frequency, the wavevector $k$ grows rapidly, indicating that the mode becomes more tightly confined to the interface. As shown in Figure 2.4, the SPhP dispersion curve lies to the right of the light line with $k > k_0$, which shows that these modes are non-radiative and bound to the surface, ensuring energy stays localized near the interface and allowing for subwavelength control of light. Furthermore, the dispersion plot shows no intersection between the light line and SPhP dispersion curve. This means that direct excitation of SPhP modes is not possible as it requires momentum greater than that of light in air. As a result, additional techniques are needed to overcome this momentum mismatch and add extra momentum to the light line.

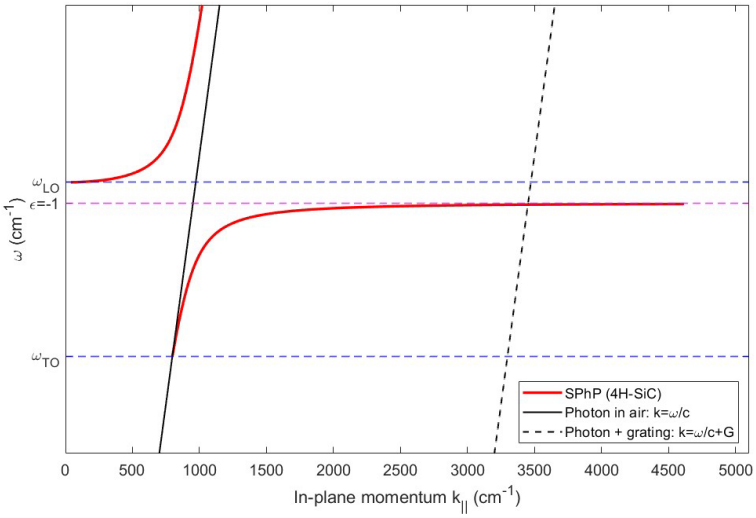

*Figure 2.4 Dispersion relation of lossless surface phonon polaritons (SPhPs) in 4H-SiC. The SPhP dispersion curve (red) lies between the TO and LO phonon frequencies. The black solid line shows the light dispersion in air, while the black dashed line represents the grating-assisted photon momentum that enables coupling to the SPhP branch.*

To make this possible, setups like prism or grating couplers are used. In prism-based methods, the Otto configuration [31] or the Kretschmann configuration [32] is often used. But these methods are not compatible with miniaturized or on-chip photonic systems. Another method involves using a rough surface to excite SPhPs [33]. The main disadvantage of this method is its limited control over the excited mode. The reason is that the light scatters randomly from the rough surface, and only some of the scattered waves gain enough momentum to excite the SPhP. The issue is that we can't control exactly how much momentum is added or the direction and wavevector of the excited mode. Another method is applying a periodic modulation like a diffraction grating on the surface of the dielectric. This periodic structure introduces discrete momentum components that can either increase or decrease the in-plane momentum of incoming photons, enabling phase matching.

In this thesis, the grating method is used to provide the additional momentum needed to excite surface phonon polaritons (SPhPs). In the following chapters, I will talk about the fabrication process of these gratings and demonstrate how different grating parameters can be adjusted to optimize the coupling efficiency and the propagation characteristics of SPhPs.

## 2.5 Theory of Grating Coupling:

Here, I introduce the basic theory behind optical gratings and explain how they can provide the additional momentum required to couple light to surface phonon polaritons (SPhPs) [34]. To demonstrate this concept, I use a simple grating structure with adjustable parameters (Fig. X), which helps illustrate how gratings effectively overcome the momentum mismatch between incident light and SPhPs.

When the light interacts with a grating, the periodic gratings diffract the beam in many directions. This diffraction happens as a result of the interference of the waves that are scattered by the periodic structure of the grating. The main beam that continues along the direction of the incident wave is known as the zero-order, and the other beams that come out at angles on either side are called first-order, second-order, and so on. Each higher diffraction order corresponds to a greater angular deviation from the original path, caused by the exchange of momentum between the light wave and the grating. This happens because the grating grooves effectively add to or subtract from the light wave's momentum, redirecting it into new paths where constructive interference can take place.

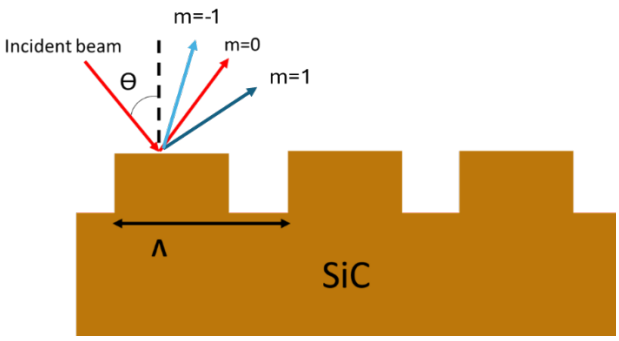


*Figure 2.5 Schematic illustration of grating-assisted coupling used to overcome momentum mismatch, showing the zeroth (m = 0) and first (m =± 1) diffraction orders.*

In the presence of a grating, the surface can be seen as a periodic perturbation that scatters incoming photons, enabling them to gain or lose discrete amounts of momentum. This modification allows light to couple to SPhPs, which possess a larger in-plane momentum than freely propagating photons.

For incoming light at an incident angle θ, the in-plane wavevector of the incident light is:

$$k_x = k_0 n_d \sin\theta \qquad 2.26$$

Which $k_0 = \frac{2\pi}{\lambda}$ is the wave number of light in vacuum. When a light wave with an in-plane momentum component impinges upon a grating, it can undergo diffraction. Each diffraction order corresponds to the incident wave gaining or losing momentum in integer multiples of the grating's wavevector G:

$$G = \frac{2\pi}{\Lambda} \qquad 2.27$$

Here, $\Lambda$ is the grating period. The condition for coupling between the diffracted light and SPhPs is given by [35]:

$$k_{sphp} = k_x \pm mG = k_0 n_d \sin\theta \pm m\frac{2\pi}{\Lambda} \qquad 2.28$$

This equation shows that the grating adjusts the momentum mismatch by modifying the in-plane component of the light's wave vector such that it matches the SPhP wave vector $k_{sphp}$.

# Chapter 3

## 3.1 FTIR:

In this section, I will explain the reflection spectrum measurement by Fourier Transform Infrared (FTIR) spectroscopy. Here, I will explain the Bruker FTIR system used in this measurement and explain how reflection spectra are obtained over a selected frequency range. These spectra show important information for analyzing optical phonons and the properties of surface phonon polaritons (SPhPs).

FTIR spectroscopy is one of the most widely used techniques for measuring infrared spectra. In the IR range, materials exhibit characteristic absorption features that help us investigate their composition and physical properties. The technique is based on the interaction of infrared light with lattice phonon modes, which absorb specific wavelengths. Analyzing the absorption or reflection spectra gives us valuable structural and dynamic information. As discussed in the previous chapter, SPhPs are electromagnetic modes that result from the coupling between infrared radiation and optical phonon modes. The measurement of the reflection spectrum using FTIR gives important insights into these interactions.

### 3.1.1 Theoretical Framework:

FTIR spectroscopy uses interferometry to gather data from all wavelengths at once along the optical path during each measurement. The main component responsible for this is the Michelson interferometer, which creates an interferogram by modulating the infrared beam through interference. This raw signal encodes the phase differences between two light beams. Mathematically, the interferogram is an autocorrelation of this optical field, shows how light waves interfere at varying optical path lengths.

To understand the relationship between the interferogram and the spectrum, we assume that the electric field of the IR wave is a superposition of all frequencies.[36]:

$$E(r,t) = \frac{1}{2\pi} \int_{-\infty}^{\infty} \sqrt{B(\omega)} e^{i(\omega t - q.r)}\, d\omega \qquad 3.1$$

B(ω) is the spectrum of the electromagnetic radiation, and our goal is to determine this function from the measured data.

The time-averaged detected intensity as a function of time delay is given by:

$$I(\tau) = \frac{I_0}{2} + \frac{C}{16\pi^2 T} \int_{-\infty}^{\infty} B(\omega)\, cos(\omega\tau)\, d\omega \qquad 3.2$$

Here $I_0$, is the time-averaged total intensity of the two combined beams and represents the constant background in the interferogram. The second term, with a cosine transform of the spectrum B(ω), explains how different frequency components interfere constructively or destructively depending on the optical path difference τ. In this way, the interferogram encodes the frequency content of the infrared light.

After subtracting the constant baseline and taking the Fourier transform, the spectrum can be extracted:

$$B(\omega) = \frac{32\pi T}{C} \int_{-\infty}^{\infty} \left[ I(\tau) - \frac{I_0}{2} \right] e^{-i\omega\tau}\, d\tau \qquad 3.3$$

This process is explained by the Wiener–Khinchin theorem, which states that the Fourier transform of the interferogram gives the frequency-dependent power spectrum, i.e., the infrared spectrum. This fundamental principle explains why the technique is called "Fourier transform infrared

spectroscopy" (FTIR): In this method, the Fourier transform is used to convert the raw signal in the time domain into a meaningful spectrum in the frequency domain.

Since the range of mirror movement is limited, integration is performed over a limited range, which results in spectral broadening and reduced resolution. This is analogous to applying a rectangular window to an ideal interferogram, whose Fourier transform produces sidelobes. To reduce these unwanted effects, apodization functions are used to taper the interferogram smoothly [36].

### 3.1.2 Experimental setup

Having reviewed the theory regarding the relationship between the interferogram and the spectral content of infrared radiation, we now turn to the details of data collection. In a typical setup, like the Bruker system used in this study, the infrared source is a globar, a broadband thermal emitter, located at the focal point of the L1 lens. The beam enters the interferometer, where a beamsplitter divides it into two paths, as illustrated in the accompanying figure. A KBr beamsplitter was used in this study. It is half-polished and coated to be partially reflective and partially transmissive, allowing the beam to split evenly.

Two beams reach the detector after traveling different optical paths. One beam is reflected by a fixed mirror, and the other beam passes through a splitter and hits a moving mirror. The moving mirror modulates their relative phase by changing the optical path difference (Δ) between the two beams. Changing the optical path difference causes different wavelengths to interfere constructively or destructively at different positions. This results in the formation of an interferogram that contains spectral information. The schematic of this setup is illustrated in Figure 3.1.

In the Bruker FTIR system, a built-in helium-neon (HeNe) laser is used to precisely control the position and speed of the moving mirror. Because the HeNe laser has a fixed and known wavelength, it can be used to track the mirror movement precisely. This system ensures perfect

synchronization between the mirror movement and the data collection process, resulting in an interferogram that is recorded with high accuracy and reliability.

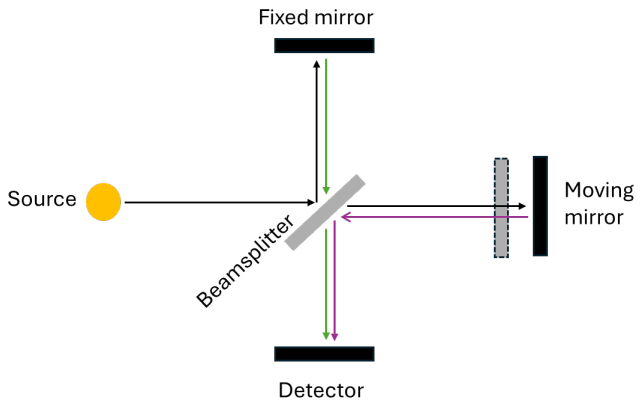


*3.1 Schematic of a Michelson interferometer used in FTIR.*

After the IR beam passes through the interferometer, it interacts with the sample. As a result of this interaction, an interferogram is created, which is then recorded and processed. This interaction can be studied in either transmission or reflection mode. In this study, we performed reflection measurements. The recombined and modulated beam is focused onto the sample surface, and the reflected light from the sample is collected and focused onto an IR photodetector. The mercury cadmium telluride (MCT) detector is used in our setup, and it needs to be cooled down with liquid nitrogen to 77 K to suppress thermal noise.

The objective used for broadband operation in this setup is a Cassegrain reflective metallic objective, as shown in fig. The reason for not using conventional refractive objectives is that they suffer from chromatic aberrations due to refractive index dispersion, and most materials used in conventional objectives have absorption bands in the mid-IR, limiting their effectiveness. One disadvantage of Cassegrain objectives is that they illuminate the sample with a range of angles and an average angle that isn't zero, as illustrated in Figure 3.2. This can cause issues in measurements that are highly sensitive to the angle of incoming light.

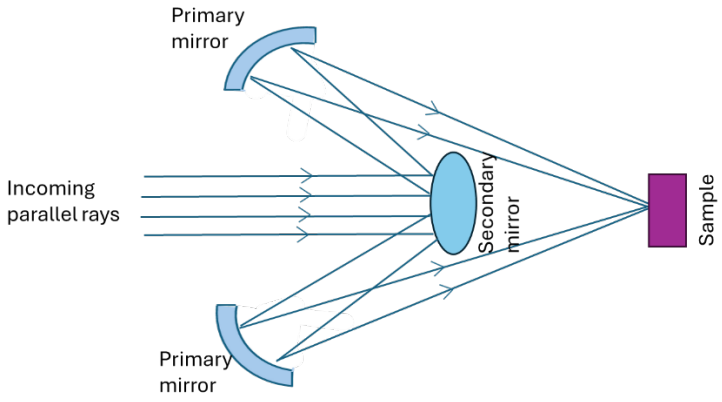


*3.2 Schematic cross-sectional view of a Cassegrain reflective objective commonly used in FTIR microscopy.*

### 3.1.3 Reference and Normalization

Accurate spectral analysis requires the collection of two interferograms: one from the sample and one from the reference. In this work, a gold mirror was used as the reference. To obtain the true reflectance spectrum, the sample data are normalized to the reference data. An example of this process is shown in Figure 3.3, where the raw data (including the sample and background) are compared with the corrected reflectance spectrum of 4H-SiC.

This method helps us to accurately extract reflection spectra, which contains the infrared light interaction with optical phonons and surface polaritons. These spectra include valuable information about the properties of materials at the nanoscale.

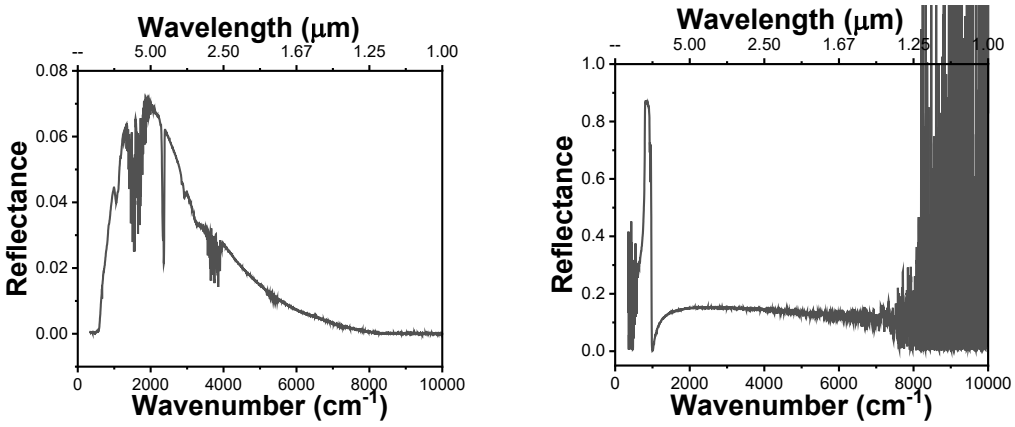


*3.3 (a) Raw FTIR data collected from the 4H-SiC sample. (b) Corrected reflectance spectrum obtained after normalizing the sample signal to the reference.*

In our lab, the FTIR spectrometer is coupled to a microscope for analyzing different sample gratings. In the next chapter, I will show that I have a sample with 14x14 different gratings, where each grating has a different height and pitch. So, it is very important to analyze the reflection spectrum of each sample separately and compare the results to see how grating parameters can affect the excitation of SPhP modes.

## 3.2 Comsol Simulation:

As already mentioned, the reflection spectrum is a useful method for understanding the coupling mechanism, identifying whether any SPhP excitation has occurred, and gaining a better understanding of the effects of grating parameters. To simulate the far-field reflection spectrum, we used the finite element method (FEM) software COMSOL Multiphysics and compared the results with experimental findings. In this section, I will explain the simulation setup and explain the theory behind the FEM method used in this simulation to provide insight into how it works.

COMSOL solves Maxwell's equations in complex geometries using the finite element method. In such geometries, it is very difficult to find an analytical solution to Maxwell's equations, so the finite element method (FEM) is used as a powerful method to solve this problem. As mentioned in the previous section, Maxwell's equations, which describe the propagation of electromagnetic waves, can be rewritten as boundary value problems involving coupled partial differential equations.

In the finite element method (FEM), the computational domain is divided into smaller components that are placed together as a mesh, and the components of the electric and magnetic fields in each component are approximated using interpolation functions. The Glerkin method [37], commonly used in the finite element method (FEM), is based on choosing test functions as basis functions and reducing the residual error by a weighted average. This makes the residual error orthogonal to the subspace formed by the basis functions. As a result, the problem can be written in matrix form, enabling efficient numerical calculation of field distributions. The complete explanation of this method can be found in [36].

FEM is a very effective method in electromagnetic simulations and can be used in desired geometries with complicated boundary conditions and inhomogeneous materials. It can be used for accurate modeling of nanophotonic and polaritonic systems. FEM allows arbitrary meshing using triangular (2D) or tetrahedral (3D) elements and is better suited for modeling curved and complex geometries. Due to the non-Cartesian meshing (unlike FDTD), FEM reduces simulation time for complex geometries.

Meshing can be considered as the main part of the FEM, because the accuracy and stability of the results depends directly on it. A finer mesh results in a better approximation of the field, especially in the regions with sharp variation, like on the grating surfaces. Another important factor in determining the mesh size is the excitation wavelength and skin depth. The skin depth shows how deep electromagnetic fields penetrate into the material and should be compared with the structure's dimensions to make sure the mesh is accurate. For materials like SiC in the mid-infrared range,

where surface phonon polaritons exist, the effective wavelength inside the material is significantly shorter than in free space. Therefore, the mesh was refined accordingly to resolve these subwavelength features. If the meshing is not small enough to cover this range, the results will not be reliable. Therefore, FEM is a powerful method for solving Maxwell's equations in complex geometries, but reliable results strongly depend on the meshing. To accurately model the periodic nature of the structure, periodic boundary conditions were applied on the lateral sides, and the mesh was constructed symmetrically within one unit cell. This meshing strategy ensures that surface phonon polariton modes, which are highly sensitive to both geometry and material dispersion, are correctly captured in the frequency-domain simulation.

For the simulation, we used the Radio Frequency module (RF Module) with electromagnetic waves, frequency domain (ewfd) analysis to study the system response over a range of frequencies. COMSOL has a CAD-like environment, which makes it easy to build the desired grating. For this work, I used AFM data of my grating and applied interpolation to create an exact replica in the simulation, matching the experimental sample. Only one period of the grating was modeled, and periodic boundary conditions were applied to simulate an infinite grating, replicating the experimental situation.

We used Floquet boundary conditions for this purpose. In this boundary condition, the light waves are defined in the following form: [38]

$$\vec{\psi} = e^{i\vec{k}\vec{r}} U_{\vec{k}}(\vec{r}) \qquad 3.4$$

Where $U_{\vec{k}}(\vec{r})$ modulates the wavefunction and is periodic with the periodicity of the crystal.

$$u(\vec{r}) = u(\vec{r} + \vec{a}) \qquad 3.5$$

Therefore:

$$\psi(\vec{r}) = \psi(\vec{r} + \vec{a}) \qquad 3.6$$

This theory is similar to Bloch's theory for the electron wavefunction in a periodic atomic crystal [39].

Then we need to define the permittivity for each area. The surrounding area is defined as air, and for the substrate, we used the wavelength-dependent permittivity of SiC, which we obtained from ellipsometry of the SiC sample. An in-plane wave is excited from the top port, and this port is also used for absorbing the reflected light and displaying the reflection spectrum. The in-plane wave is incident on the substrate with a frequency varying in the range of 9–11 μm, which is the range of the Reststrahlen band for SiC. The reflection spectrum is calculated, and the data is extracted within this range.

The angle of incidence is one of the important parameters, and we used different angles based on the objective that was used experimentally. For different analyses, we also sweep the angle of incidence to study the effect of changing this parameter, which will be explained thoroughly in Chapter 5. Also, in Chapter 5, for simulating the point excitation needed for analyzing the traveling wave, we used dipole mode excitation instead of port excitation. More details will be explained in that chapter.

## 3.3 Raman

### 3.3.1 Theory

Raman spectroscopy is a technique that provides information that adds to Fourier-transform infrared (FTIR) spectroscopy. Both methods probe the vibrational modes of materials through different physical mechanisms. As explained earlier, FTIR detects the absorption of infrared light caused by phonon excitation in the sample. Raman spectroscopy, on the other hand, probes phonon excitations through inelastic light scattering. This non-destructive optical technique is based on the interaction of monochromatic light with a sample. This method is based on measuring inelastically

scattered light, which results from the exchange of energy between an incident photon and a phonon (which is either excited or annihilated).

A phonon mode is Raman-active if it causes a change in the polarizability of the molecule, which is usually associated with symmetric vibrations. In contrast, infrared (IR) absorption depends on vibrations that cause a change in the dipole moment, which often arises from asymmetric vibrations. These differences make Raman and FTIR spectroscopy complementary techniques.

In this thesis, I use Confocal Raman Microscopy to study the Raman-active phonon modes in the 4H-SiC structure, visualize their spatial distribution, and explore the coupling mechanisms between bulk phonons and localized surface phonon polariton (SPhP) modes. To better understand the Raman measurements, I first review the elastic and inelastic scattering processes. Then, I talk about the principles of Raman spectroscopy and explain the experimental setup used to collect Raman data in this study.

When light is incident on a material, it may be absorbed, transmitted, or scattered. Normally, scattering does not happen in a homogeneous material because reflected light destructively interferes in all directions except the forward direction. However, thermal fluctuations of atoms can locally break this homogeneity, causing light scattering to happen even in a homogeneous material.[24, 40].

The light can be scattered elastically or inelastically. In elastic scattering, an incident photon excites the system to a virtual state. Since these virtual states are not real stationary states, the photon is re-emitted with the same frequency $\omega_L$ , as illustrated in Fig 3.4. Therefore, the energy of the incoming light matches the energy of the scattered light. This process is known as Rayleigh scattering.

There are also Stokes and anti-Stokes scattering, which are types of inelastic scattering processes. In Stokes scattering, part of the incident photon's energy is transferred to the crystal to excite an optical phonon mode. As a result, the scattered photon is emitted with lower energy (longer

wavelength) than the incident photon ($\omega_s = \omega_L - \omega_{phonon}$). In this process, the system absorbs energy to generate a phonon, which is indicated in the figure by the transition from the ground vibrational state to a higher vibrational state. In contrast, anti-Stokes scattering happens when a phonon in the lattice that has been previously excited by heat interacts with an incident photon. In this case, the photon gains energy from the phonon and is scattered with a higher energy (shorter wavelength) than the incident light ($\omega_s = \omega_L + \omega_{phonon}$). This means the system loses energy to the photon as the phonon is annihilated. This is shown in Figure 3.4 by the transition from an excited vibrational state to the ground state.

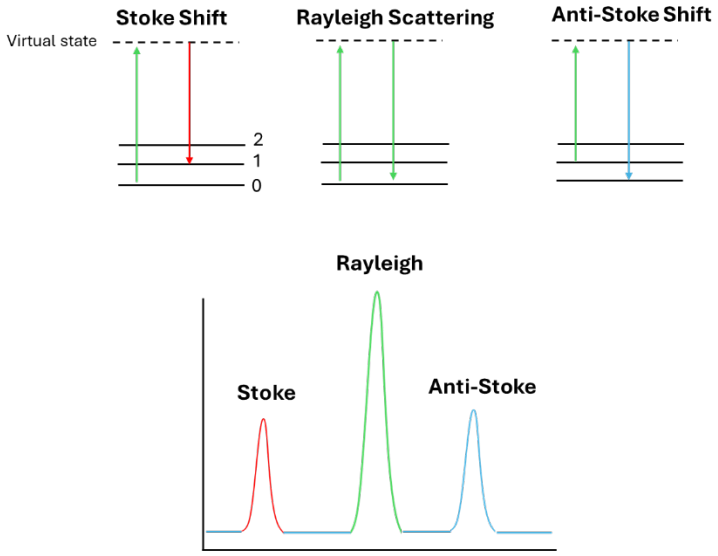


*3.4 Schematic representation of photon interactions in Raman spectroscopy. (Top) Energy level diagrams illustrate Stokes scattering, Rayleigh scattering, and anti-Stokes scattering. (Bottom) Corresponding Raman spectrum showing intensity versus energy shift for the three scattering processes.*

This implies that anti-Stokes scattering can only happen when thermally excited phonons already exist in the lattice. At room temperature, the number of these excited phonon states is usually lower

than the number of ground states. This makes the anti-Stokes signal weaker than the Stokes signal. In the Stokes process, the emitted photon has less energy compared to the anti-Stokes process. As a result, Stokes signals appear to the left of the Rayleigh scattering peak in a Raman spectrum, while anti-Stokes signals appear to the right, as shown in Figure 3.4. In this figure, $\omega_L$ represents the Rayleigh scattering, which corresponds to the frequency of elastically scattered light. This is the main scattering process, which does not involve any frequency shift. Only a small fraction of the photons undergo inelastic scattering, which is what we aim to detect in Raman spectroscopy. Consequently, Rayleigh scattering is the dominant process, and without blocking it, the Raman signal cannot be observed. As I will explain in more detail later, certain equipment is designed to block the Rayleigh scattering to enable the detection of the Raman signal. Raman scattering can occur as either first-order or higher-order. In first-order Raman scattering, only one phonon is involved in the process, while higher-order Raman scattering involves two or more phonons. Therefore, the energy shifts in higher-order Raman scattering are larger compared to the first-order case.

In Fig.3.4, the first-order Stokes process is shown by the peak at $\omega_L - \omega_i$ , and the first-order anti-Stokes process is shown by the peak at $\omega_L + \omega_i$. Higher-order Raman peaks, which require more than one phonon, would show up at even bigger shifts (e.g., $\omega_L \pm 2\omega_i$), but this image doesn't show them.

### 3.3.2 Instrumentation and setup for Raman scattering experiment

We used the WITec alpha300 to perform Raman spectroscopy measurements. This advanced system combines high-resolution optical microscopy with confocal Raman spectroscopy, enabling chemical analyses with precise spatial resolution. The experimental configuration is schematically shown in Figure 3.5. The system uses a laser excitation source, commonly a frequency-stabilized diode-pumped solid-state (DPSS) laser. A 532 nm green laser was used for this work, based on the bandgap energy of SiC and the spectrum requirements of the experiment. The laser emits a highly coherent and monochromatic beam, which is essential for Raman scattering experiments. The laser

beam was transmitted to the microscope base through a single-mode optical fiber and then collimated and directed using a set of mirrors and beam splitters.

The excitation beam was directed toward the sample through a diffraction-limited ZEISS EC Epiplan-APOCHROMAT 100× objective (NA = 0.9), which focuses the laser onto the sample surface. Raman scattering from the sample is recorded through the same objective lens in backscattering geometry. In the confocal configuration, light is collected only from the focal plane, which results in increased spatial resolution and reduced background noise. The backscattered signal passed through a beam splitter and was separated from the excitation light using appropriate notch or edge filters to remove the Rayleigh line. These long-pass filters block the laser line and pass the Stokes-shifted Raman signals.

Then the filtered Raman signal was coupled into a multimode optical fiber and directed to a high-throughput spectrometer. This spectrometer is equipped with a thermoelectrically cooled CCD detector, which is used to record spectral data. This system allowed for diffraction-limited spatial resolution and high signal collection efficiency, which are suitable for spectral and depth Raman mapping.

In our experiment, an analyzer (a detection polarizer) was always placed in the collection path to select a specific polarization direction of the scattered light. The polarization of incident light can be adjusted by inserting a half-wave plate into the excitation path, which allows the polarization direction of the incident laser light to be rotated as needed. The analyzer was located just before the spectrometer entrance, and the half-wave plate was placed in the laser excitation path prior to the beam entering the microscope objective, as shown in Fig 3.5. This configuration enabled precise control of both the incident and detected polarization states during Raman measurements.

Depending on the experimental objectives, some measurements in this study were conducted using unpolarized excitation, while others required polarized excitation to selectively excite and analyze different phonon modes in the material. This polarization-dependent approach enabled us to

distinguish between Raman-active vibrational modes that are sensitive to the orientation of the electric field.

A more detailed discussion of polarized measurements, in perpendicular and parallel polarization configuration, is presented in Chapter 6. The combination of the polarized and the unpolarized measurements allowed for detailed studies of the various phonon modes and allowed for the identification of novel unobserved phenomena in some specific phonon modes.

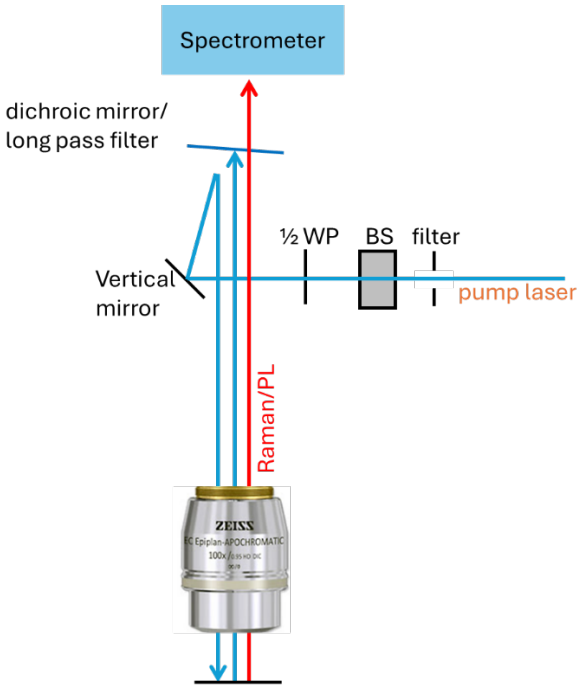


*3.5 Simplified optical schematic of the alpha300 R Raman microscope*

Raman measurements can be performed in different scattering configurations, such as backscattering and forward scattering. The backscattering configuration is used in this study. In this setup, the incident light is along the z-axis onto the sample surface, and the scattered light is

collected in the same direction but reflected in the opposite way. Several common measurement configurations are shown in Fig.3.6.

The polarization orientation of the incident and scattered light relative to the crystal axes of the sample affects the intensity of the detected Raman peaks. This dependence is because phonons in a crystal have certain symmetries that affect how they interact with light. These vibrational symmetries determine how the crystal's polarizability changes during the vibration, and only those modes that produce a change in polarizability matching the polarization configuration of the incident and scattered light will result in a strong Raman signal.

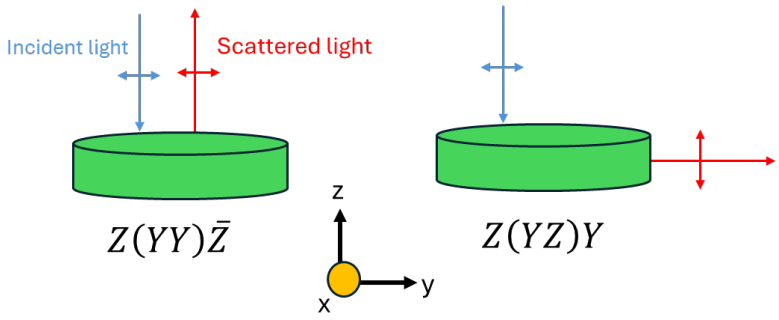


*3.6 Two possible Raman measurement configurations, where single arrows indicate the directions of incident and scattered light, and double arrows represent the polarization orientations*

To describe the polarization configuration in Raman experiments, Porto notation is commonly used [41]. A typical example looks like $x(yz)\bar{x}$, where the letters outside the parentheses indicate the propagation directions of the incident and scattered beams, and the letters inside represent their polarization directions. In this example, the incident light propagates along $x$ and is polarized along $y$, while the scattered light is collected along $-x$ with polarization along $z$.

By changing these measurement configurations, different Raman lines appear or disappear depending on the phonon symmetry. This approach provides a deeper understanding of the material, allowing for a detailed investigation of its lattice dynamics and crystal structure.

WITec Control software, called Project FIVE, is used to analyze the collected Raman spectrum. This software provides comprehensive data processing and visualization capabilities. Using Project FIVE, we were able to generate accurate 3D spatial maps of Raman signals, allowing us to visualize the distribution of different phonon modes at the sample level. In addition, the software has advanced capabilities for background removal, noise reduction, and spectral peak analysis, which increase the clarity and accuracy of the final results.

### 3.3.3 Classical Theory of Raman scattering

When an incident laser beam with electric field **E** interacts with a crystalline material, it does not necessarily produce a polarization field $P$ field parallel to E, because the electrical susceptibility tensor in crystals is anisotropic. Therefore, the direction and magnitude of P are determined by both the electric field and the directional properties of the susceptibility tensor, as shown in Equation x. This relationship is described by the material's electric susceptibility tensor $\chi$, which quantifies how easily the material becomes polarized under an electric field, linking the polarization and electric fields via [42, 43]:

$$P = \varepsilon_0 \chi E \qquad 3.7$$

This anisotropic behavior arises because the electric field of light interacts more with the electrons of the crystal, since the electrons react more quickly than the nuclei. However, the electron polarizability and therefore the susceptibility tensor $\chi$ depend on the position of the nuclei, it can be approximated around the equilibrium configuration using the Taylor expansion:

$$\chi(Q_s) \approx \chi_0 + \left(\frac{\partial \chi}{\partial Q_s}\right) Q_{0s}\, cos(\omega_s t) \qquad 3.8$$

Substituting this into the polarization equation and considering an oscillating electric field $E_{(t)} = E_0\, cos(\omega_L t)$, the total induced polarization becomes:

$$P(t) = \chi_0 E_0\, cos(\omega_L t) + \left(\frac{\partial \chi}{\partial Q_s}\right) Q_{0s}\, E_0\, cos(\omega_L t)\, cos(\omega_s t) \qquad 3.9$$

Applying trigonometric identities, this leads to new frequency components at $\omega_L + \omega_s$ and $\omega_L - \omega_s$, corresponding to anti-Stokes and Stokes Raman scattering, respectively. These frequency shifts result from the modulation of the crystal's susceptibility tensor by phonons. When multiple phonon modes are involved, the susceptibility is expanded over all vibrational coordinates, resulting in both first-order (linear in $Q_k$) and second-order (nonlinear in $Q_k$) Raman effects. In this study, I focus only on first-order Raman scattering.

### 3.3.4 Raman Intensity:

Raman spectroscopy results indicate that Stokes lines are typically more intense at low temperatures, whereas anti-Stokes lines are stronger at higher temperatures. This is because, in the anti-Stokes process, the annihilation of a phonon occurs, meaning that the system must already contain thermally excited phonons. This condition is more likely at higher temperatures. In contrast, Stokes scattering involves the creation of a phonon and does not require an excited phonon, so it occurs readily even at low temperatures. Therefore, the intensity of Stokes lines is high at low temperatures, while anti-Stokes lines become more prominent only when enough thermal energy is available to populate vibrational states. However, classical theory cannot explain this temperature dependence. According to classical dipole radiation theory, the intensity of Raman-scattered light is proportional to the square of the second derivative of the polarization, which leads to [44]:

$$I(\omega) \propto \omega^4 |p(\omega)|^2 \qquad 3.10$$

Since the frequency of the anti-Stokes component is higher than that of the Stokes component, classical theory predicts:

$$\frac{I_{anti-Stokes}}{I_{Stokes}} = \left(\frac{\omega_L + \omega_s}{\omega_L - \omega_s}\right)^4 \qquad 3.11$$

While this explains that anti-Stokes scattering is always weaker (because $\omega_s << \omega_L$), it fails to explain temperature dependence and relative intensities observed in experiments.

Quantum theory explains this temperature dependence by considering the thermal population of phonon states. The phonon occupation probability follows the Bose-Einstein distribution, which results in a temperature-dependent intensity ratio between anti-Stokes and Stokes lines. Although the exact derivation of this relation is beyond the scope of this section, the intensity ratio of these two lines is given by:

$$\frac{I_{anti-Stokes}}{I_{Stokes}} \propto \left(\frac{\omega_L + \omega_s}{\omega_L - \omega_s}\right)^4 \exp\left(-\frac{\hbar\omega_s}{k_B T}\right) \qquad 3.12$$

This expression accurately reflects the suppression of anti-Stokes scattering at low temperatures, where phonon populations are small, and its enhancement at higher temperatures.

### 3.3.5 Symmetry and the Role of Group Theory

This section focuses on the symmetry classification of phonons in the 4H polytype of silicon carbide (SiC) and shows how group theory is used to determine Raman-active, infrared-active, and silent modes. Here, we examine the 4H-SiC space group, analyze the vibrational modes at the Brillouin zone center (Γ-point), and explain how selection rules can be derived from group theory. This analysis is very important for the interpretation of experimental Raman and infrared spectra.

The vibrational properties of a crystal are connected to its symmetry. The full set of symmetry operations that leave the crystal structure unchanged defines its space group. At the center of the

Brillouin zone, translational symmetry no longer applies, and the space group reduces to a corresponding point group containing the principal symmetry elements governing the vibrational modes.

4H-SiC crystal shows the symmetry of the point group $C_{6v}$ at the Γ-point. This group includes several symmetry operations, such as the identity operation (E), rotations of 60°, 120°, and 180° ($C_6$, $C_3$, and $C_2$), along with vertical mirror planes commonly denoted as $\sigma_v$ and $\sigma_v'$. These symmetry operations determine how phonon modes transform and enable their classification using the irreducible representations of the group.

The unit cell of 4H-SiC contains eight atoms, resulting in 24 vibrational modes ($3N = 24$); three of these modes are acoustic and twenty-one are optical. At the Brillouin zone center (Γ-point), these vibrational modes decompose into the irreducible representations of the $C_{6v}$ point group as follows:

$$\Gamma_{vibration} = 4A_1 + 4B_1 + 4E_1 + 4E_2 \qquad 3.13$$

Each irreducible representation corresponds to a specific phonon symmetry and determines whether the mode is Raman active, infrared active, or optically inactive (silent). This classification is important for better understanding spectroscopic data and lattice dynamics in 4H-SiC.

To investigate more precisely which phonon modes are observable in Raman experiments and under what conditions they can be detected, we examine the mathematical structure of the Raman tensors associated with the symmetry operations of the $C_{6v}$ point group.

### 3.3.6 Raman Activity and Polarizability

The Raman tensor's components show how the polarizability of the material changes in response to each phonon mode. A mode is Raman active if its symmetry allows a non-zero component of

the Raman tensor, i.e., $\frac{\partial \chi_{jl}}{\partial Q_k} \neq 0$, where $\chi_{jl}$ is the electric susceptibility tensor and $Q_k$ is the normal coordinate associated with vibrational mode k. This condition means the mode can modulate the polarizability of the crystal and therefore scatter incident light in a Raman process. Raman activity thus depends on the symmetry of the mode and the structure of its associated Raman tensor.

In the $C_{6v}$ point group, the irreducible representations that contribute to Raman scattering are $A_1$, $E_1$, and $E_2$. Modes with symmetries $A_2$ , $B_1$ , and $B_2$ do not result in Raman activity under usual conditions due to their tensor symmetry.

### 3.3.7 Raman Tensor Forms and Experimental Selection Rules

The Raman activity of each vibrational mode in 4H-SiC is determined by the symmetry of its corresponding Raman tensor. The $A_1$ phonon modes have fully symmetric diagonal Raman tensors:

$$\chi_{A_1} = \begin{pmatrix} a & 0 & 0 \\ 0 & a & 0 \\ 0 & 0 & a \end{pmatrix} \qquad 3.14$$

This form contains non-zero diagonal components, specifically $\alpha_{xx} = \alpha_{yy}$ and $\alpha_{zz}$, which correspond to symmetric stretching or compression vibrations along the principal axes of the crystal. These modes are detected in parallel polarization configurations such as $z(xx)\bar{z}$ or $z(yy)\bar{z}$, where the incident and scattered light are polarized in the same direction.

$E_1$ modes are doubly degenerate and involve coupling between in-plane and out-of-plane motion. They have off-diagonal tensor components, such as:

$$\chi_{E_1} = \begin{pmatrix} 0 & 0 & c \\ 0 & 0 & 0 \\ c & 0 & 0 \end{pmatrix}, \begin{pmatrix} 0 & 0 & 0 \\ 0 & 0 & d \\ 0 & d & 0 \end{pmatrix} \qquad 3.15$$

These components require light polarization with a z-axis (out-of-plane) component.

Therefore, $E_1$ modes are not observed in standard backscattering along the z-direction but may be accessed using configurations like $x(zx)\bar{x}$ or $y(zy)\bar{y}$, which involve oblique incidence or side-collection.

$E_2$ modes are also doubly degenerate but are confined to in-plane motion. Their Raman tensor includes components like:

$$\chi_{E_2} = \begin{pmatrix} e & 0 & 0 \\ 0 & e & 0 \\ 0 & 0 & 0 \end{pmatrix}, \begin{pmatrix} 0 & f & 0 \\ f & 0 & 0 \\ 0 & 0 & 0 \end{pmatrix} \quad 3.16$$

Unlike $E_1$ modes, the $E_2$ vibrations are confined to the basal plane and result in changes to the in-plane components of the polarizability tensor. These modes are observable in both parallel and crossed polarization configurations such as $z(xx)\bar{z}$ and $z(xy)\bar{z}$ , making them useful for probing in-plane crystal properties and strain effects.

Modes with symmetries $A_2$, $B_1$, and $B_2$ are typically Raman inactive since they do not couple effectively to the incident light field via polarizability changes.

### 3.3.8 IR Active Modes

A vibrational mode is IR active if its symmetry matches one of the components of the dipole moment vector in the x, y, or z directions. This criterion arises because IR absorption occurs when the electric field of the incident light interacts with the dynamic dipole moment caused by the atomic displacements in a phonon mode. Only those modes that cause a net change in the dipole moment can interact with the IR field and thus be detected in the IR spectrum. In the 4H-SiC crystal, modes with $A_1$ symmetry are associated with dipole oscillations along the z-axis and are therefore infrared active along the c-axis of the crystal. Similarly, modes with $E_1$ symmetry transform like the in-plane x and y components of the dipole moment, and are therefore IR active

in the basal plane. This classification helps to identify the polarization orientation of IR-active phonons in experimental measurements.

### 3.3.9 Silent Modes

Modes that transform according to $B_1, B_2$ symmetry, or other representations that do not affect the dipole moment vector or the polarizability tensor, are known as 'silent' modes. They are not active in either the Raman or IR spectra. However, these modes may be involved in other physical processes, but do not appear directly in first-order spectroscopic measurements. By applying this symmetry-based classification, it is possible to identify and interpret the spectral lines observed in the Raman and infrared spectra, and thus to gain a detailed understanding of the lattice dynamics in the 4H-SiC structure.

### 3.3.10 Raman Intensity and Polarization Dependence

Whether a mode is observed in an experiment also depends on the polarization of the incident and scattered light, formalized by the Raman intensity expression:

$$I\chi = \left|e_s \cdot \chi^{(k)} \cdot e_i\right|^2 \qquad 3.17$$

where $\chi^{(k)}$ is the Raman tensor for mode k, and $e_i$ and $e_s$ are the polarization vectors of the incident and scattered light, respectively. The scalar product measures how the crystal symmetry couples to the experimental geometry, thereby dictating whether a mode will be observed.

In this thesis, we work exclusively with the backscattering configuration. Therefore, the analysis focuses on the Raman mode intensities observed in that specific geometry.

For example, in the z(xy)$\bar{z}$ configuration, the incident light is polarized along the x-axis and the scattered light is analyzed along the y-axis. This corresponds to polarization vectors $e_i = (1\ 0\ 0)$

and $e_s = (0\ 1\ 0)$. By substituting these vectors into Equation 4.6 and considering the Raman tensor of the $\mathbf{A_1}$ mode from 3.15, we get:

$$e_s \cdot \chi_{A_1} \cdot e_i = (1\ 0\ 0) \cdot \begin{pmatrix} a & 0 & 0 \\ 0 & a & 0 \\ 0 & 0 & a \end{pmatrix} \cdot \begin{pmatrix} 1 \\ 0 \\ 0 \end{pmatrix} = 0 \qquad 3.18$$

This result shows that the $A_1$ mode is symmetry-forbidden in the crossed polarization configuration. However, it is allowed in parallel polarization geometries, where both the incident and scattered light are polarized in the same direction. The resulting Raman intensity is $a^2$ when the light is polarized along the x-direction, and $b^2$ when it is polarized along the y-direction.

A summary of the allowed vibrational symmetries under various polarization configurations is provided in Table 3.1.

| Back scattering configuration | $z(xx)\bar{z}$ | $z(xy)\bar{z}$ | $z(yx)\bar{z}$ | $z(yy)\bar{z}$ |
|---|---|---|---|---|
| $A_1$ | $a^2$ | 0 | 0 | $b^2$ |
| $E_1$ | 0 | 0 | 0 | 0 |
| $E_2$ | $e^2$ | $f^2$ | $f^2$ | $e^2$ |

*3.1 Allowed vibrational symmetries detected under different polarization configurations.*

Symmetry analysis of the Raman tensor is a useful tool for predicting the phonon modes observed in backscattering experiments with different polarizations. By analyzing how the symmetry of a phonon mode influences the polarization of the incident and scattered light, it is possible to predict which Raman modes will appear in the spectrum and which will be forbidden. In the simulation part of this study, the presented theoretical framework was applied to model the Raman mapping of the 4H-SiC structure. By considering the polarization selection rules and Raman tensor

projections, we were able to simulate the spatial variations of different phonon modes across the sample and analyze their coupling with bulk phonon modes. The details of this simulation method, along with its results and applications, will be fully discussed in the next chapter.

## 3.4 Nanoscribe

The fabrication of 1D grating structures in this work was performed using the Photonic Professional GT2 Nanoscribe equipment and IP-Dip photoresist on a 4H-SiC substrate. Two-Photon Polymerization (2PP) is the physical process that enables high-resolution, three-dimensional direct laser writing in the Nanoscribe system. This section discusses the operating principles of the Nanoscribe system, the configuration and settings used during fabrication, and the approach taken to fabricate 1D grating structures.

Two-photon polymerization is a nonlinear optical process in which a molecule absorbs two lower-energy photons at the same time, usually in the near-infrared (NIR) range, to reach an excited electronic state and start photopolymerization. Two-photon polymerization (2PP) differs from conventional UV lithography in that UV lithography cures the entire exposed area, whereas 2PP initiates polymerization only within a highly confined region, or voxel, where the photon intensity is sufficient for absorption to occur. This voxel-level control lets you make features smaller than the diffraction limit and structure things in 3D very precisely inside a clear photoresist. In our configuration, the IP-Dip resin was used in dip-in laser lithography mode, where the photoresist serves as both immersion medium and printing substrate, enabling access to the full working distance of the objective. A high-numerical-aperture objective lens focuses femtosecond laser pulses into the resist, creating confined polymerization within sub-micron volumes. Despite a low average laser power, the pulse duration and repetition rate result in sufficient peak intensities to trigger nonlinear absorption in the resist. The Nanoscribe system has a galvanometric scanner for rapid lateral beam movement and a piezoelectric stage for accurate positioning in all three spatial

dimensions. This integrated configuration enables fast writing with submicron spatial accuracy, which is essential for fabricating complex 3D nanostructures as shown in Figure 3.7.

The fabricated 1D gratings work as coupling interfaces that allow incident light to excite surface phonon polariton modes on the SiC surface. By tuning grating parameters such as the pitch, height, and base width, we analyze the role of geometric design on coupling efficiency. This allows us to optimize the structure for specific spectral responses and field confinement and improve the system performance in polaritonic and sensing applications.

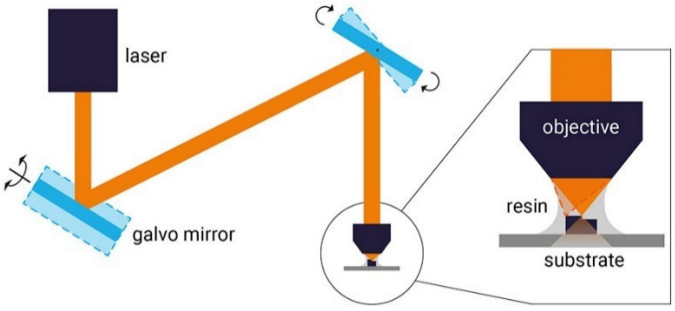


*Figure 3.7 Schematic of a Nanoscribe two-photon lithography system.*

For this purpose, we first designed the desired grating layout using NanoWrite, a software provided by Nanoscribe for preparing lithography jobs. NanoWrite converts user-defined 3D geometries into machine-readable slicing and hatching instructions that control the voxel exposure during the fabrication process. Before printing, the SiC substrate was cleaned using an oxygen plasma pre-clean (plasma preen) to enhance adhesion between the IP-Dip photoresist and the substrate surface. After the surface preparation, the Nanoscribe system was used to directly print the designed mask onto the 4H-SiC substrate. After the printing process was completed, the sample was placed in a suitable solvent to remove the unpolymerized IP-Dip. This step left hardened grating structures on the substrate surface, as shown in Figure 3.8.

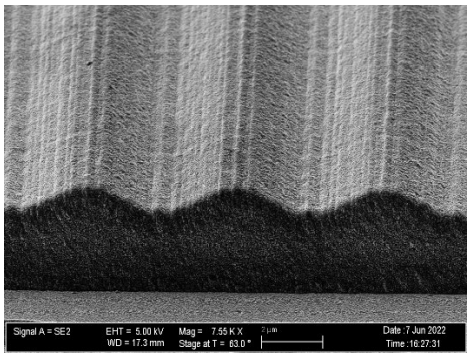


*3.8 Grating structures of polymerized IP-Dip on a 4H-SiC substrate after development using the Nanoscribe system.*

In this work, we used Reactive Ion Etching (RIE) to transfer our desired patterns into the SiC substrate. RIE is a dry etching method that uses gas-phase chemistry and plasma for material removal. In this method, radio frequency (RF) power is used to create a chemically reactive plasma in a low-pressure cylinder filled with certain gases. The plasma contains ions and reactive particles that interact with the surface of the material in two ways. One is a chemical reaction, where reactive radicals (neutral species) react with the substance to create byproducts that can be easily removed. The second way is Physical bombardment, where high-energy ions hit the surface, speeding up the etching process and helping in material removal. The combination of chemical and physical etching creates higher anisotropy (directional control), which makes this method very suitable for fabricating micro- and nanoscale structures with precise features and high aspect ratios.

In our case, the printed IP-Dip pattern acts as an etch mask during the RIE step. The polymerized resist provides sufficient selectivity and durability under optimized etching conditions, enabling the underlying SiC to be patterned with high fidelity. Parameters such as gas composition, RF power, chamber pressure, and etching time are important factors to ensure anisotropic etching, minimal surface roughness, and accurate pattern transfer. In this work, we adopted the reactive ion etching (RIE) recipe for SiC described by Sharac et al.[45]. In their method, a $CHF_3/O_2$ plasma mixture is used to find the best etch rate ratio between the IP-Dip resist and the SiC substrate. We

applied the same conditions in our process, as summarized in Table 3.2 and the general etching concept is illustrated in Figure 3.9.

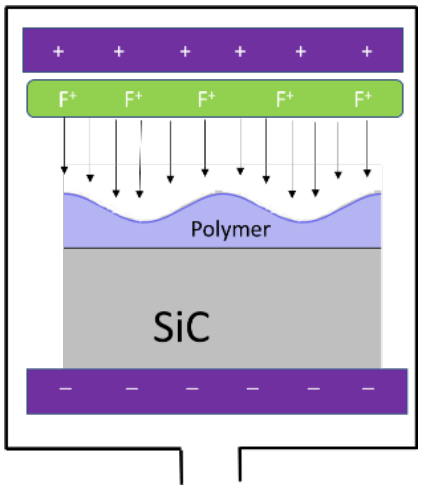


*Figure 3.9 Schematic of the RIE process using a patterned polymer mask to transfer structures onto the SiC substrate.*

Although the grating pattern was generally transferred to the SiC substrate, the resulting profile was different from the original sinusoidal design and appeared more triangular. Over-etching or an incorrect calculation of the etch rates for the resin and SiC could be some possible reasons for this distortion. If the etching time or rate is not properly matched, the resist mask can slowly wear away, resulting in unwanted side etching of the SiC substrate. This side etching changes the desired profile and causes the pattern to differ from the original design. Further optimization of the RIE parameters may be necessary to better preserve the accuracy of curved features and achieve more accurate transfer of 3D-printed geometries.

For this work, a 14×14 grating array was fabricated on the 4H-SiC substrate. Each grating unit measured 2×2 $\mu m^2$, with the pitch varying along the y-direction and the grating height adjusted along the x-direction, as shown in Fig. 3.10a.

| Material | SF6 | CHF3 | O2 | RIE (mW) | ICP (mW) | Pressure (Mtorr) | Temp. (°C) | Etch rate (nm/min) |
|---|---|---|---|---|---|---|---|---|
| SiC | 50 | 0 | 10 | 85 | 850 | 5 | 25 | 870 |

*3.2 Reactive ion etching (RIE) parameters for SiC using a $CHF_3/O_2$ plasma mixture, adapted from the method reported by Sharac et al.[45]*

This design allowed for a parametric study of grating geometry effects within a single structure. Figure 3.10b shows an AFM image of one grating, which shows the surface profile after etching. The corresponding cross-sectional view, with extracted height and period data, is presented in Fig. 3.10c.

In the next chapter, we will discuss in detail the effect of grating parameters on light and phonon coupling by analyzing their reflection spectra and simulation results.

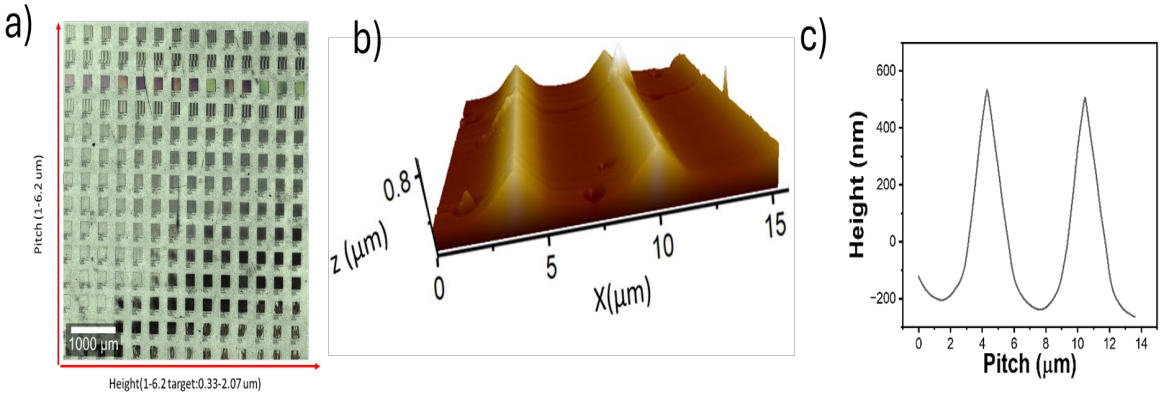


*3.10 (a) Schematic of the 14×14 grating array patterned on 4H-SiC, with varying pitch along the y-direction and grating height along the x-direction. (b) AFM image of a single grating unit after etching, showing the surface profile. (c) Cross-sectional AFM profile of the same grating, illustrating extracted height and period measurements.*

# Chapter 4

## 4.1 Mapping Phonon Polaritons with Visible Light

As discussed in Chapter 1, SPhPs have been shown to confine electromagnetic fields far below the diffraction limit, analogous to surface plasmon polaritons (SPPs), but without the strong optical losses associated with SPP modes [21, 46]. Furthermore, PhP modes are also spectrally tunable through tailoring nanostructure geometry [47], introducing free carriers [48, 49], and exploiting coupling to plasmons [50], zone-folded phonons [51], or other solid-state excitations [52-54]. These advantages have been leveraged to demonstrate the potential for PhPs in surface-enhanced sensing [55], nanophotonic circuits [56], super-resolution imaging [57], and nonlinear optics [58, 59].

The tunable and low-loss nature of PhP resonators also makes them an appealing platform for developing chip-scale mid-infrared (mid-IR) emitters [60, 61]. Efforts to demonstrate the viability of an electrically pumped PhP-based emitter have been impeded by the presumed weak interaction between phonons and PhP modes in bulk materials [61, 62]. Recent investigations have suggested that this limitation can be overcome via coupling of PhP modes to zone-folded longitudinal optical (ZFLO) phonons in 4H-Silicon Carbide (SiC) [48], although engineering such coupling places constraints on material selection and nanostructure morphology [51].

Assessing the promise of PhP modes as mid-IR emitters clearly requires an investigation of the interactions between electrons, phonons, and PhP modes. Studies on PhP-ZFLO [51] and PhP-electron interactions [48, 63] have been very important in this regard; however, full explorations of bulk phonon-PhP-electron coupling have remained limited. Practical challenges have played a role in this delay. Investigations of PhPs in dielectric nanostructures have increasingly revealed strong spatial dependence on light-matter interactions - for example, the strength of electron-phonon coupling in many nanostructures depends on the induced 3D charge distribution [48, 63, 64]. Therefore, any investigation into light-matter coupling would ideally demonstrate how the full

3D PhP eigenmodes interact with solid-state excitations to be complete.

To date, investigating PhP eigenmodes has primarily been accomplished using near-field IR microscopy, such as near-field scanning optical microscopy (NSOM) [65] and Nano-FTIR techniques[66]. Recently, monochromatic electron energy-loss spectroscopy (EELS) in scanning transmission electron microscope (STEM) setups has also been employed to visualize SPhP modes in nanostructured materials [67, 68]. This work was extended to a tomographic setup combining tilted EELS spectra with reconstruction algorithms in magnesium oxide nanostructures to first achieve a 3D mapping of SPhP eigenmodes [69].

Increasingly, these efforts have been augmented with the techniques of Raman spectroscopy, leveraging its ability to provide abundant information on light-matter interactions. Raman techniques have particularly been used to probe PhPs in 2D materials. Initial works demonstrated resonant Raman spectroscopy as a valuable tool to probe PhP modes at Van der Waals (VdW) material interfaces, revealing effects such as Raman activity of silent phonons [70], enhancement of PhP Raman features [71], and PhPs outside the Reststrahlen band [72]. Further, recent investigations have shown that conventional backscattering Raman can probe PhP modes in 2D gallium selenide, utilizing the polarizability selection rules [73]. Such techniques are not restricted to 2D materials, micro-Raman investigations of 4H-SiC nanopillars found that spatial dispersion of the permittivity in dielectric nanostructures can play a major role in the spectral behavior of PhPs [64]. This discovery highlights the fact that much of the physics related to the spatially dependent interactions of electrons, phonons, and SPhP modes in nanostructures remains uninvestigated. Therefore, efforts to understand the physics governing PhPs in nanostructures demand not only spectral probing of SPhP dispersion but also spatial mapping of light-matter interactions through the nanostructure volume with more sophisticated Raman techniques.

In this work, we report the mapping of SPhP electromagnetic fields in nanostructures of InP and 4H-SiC. We combined confocal Raman microscopy with an eigenmode reconstruction approach to provide a 3D view of localized polariton fields. Using this technique, we demonstrate that all Raman-active bulk phonon modes in both InP and 4H-SiC do couple to the localized surface

polariton modes, in contrast to the assumption that the longitudinal polarization field of the LO phonon is non-interacting with the transverse (and thus orthogonal) SPhP modes. Our Raman maps confirm that the polarizability selection rules form the dominant mechanism through which SPhPs couple to phonon modes.

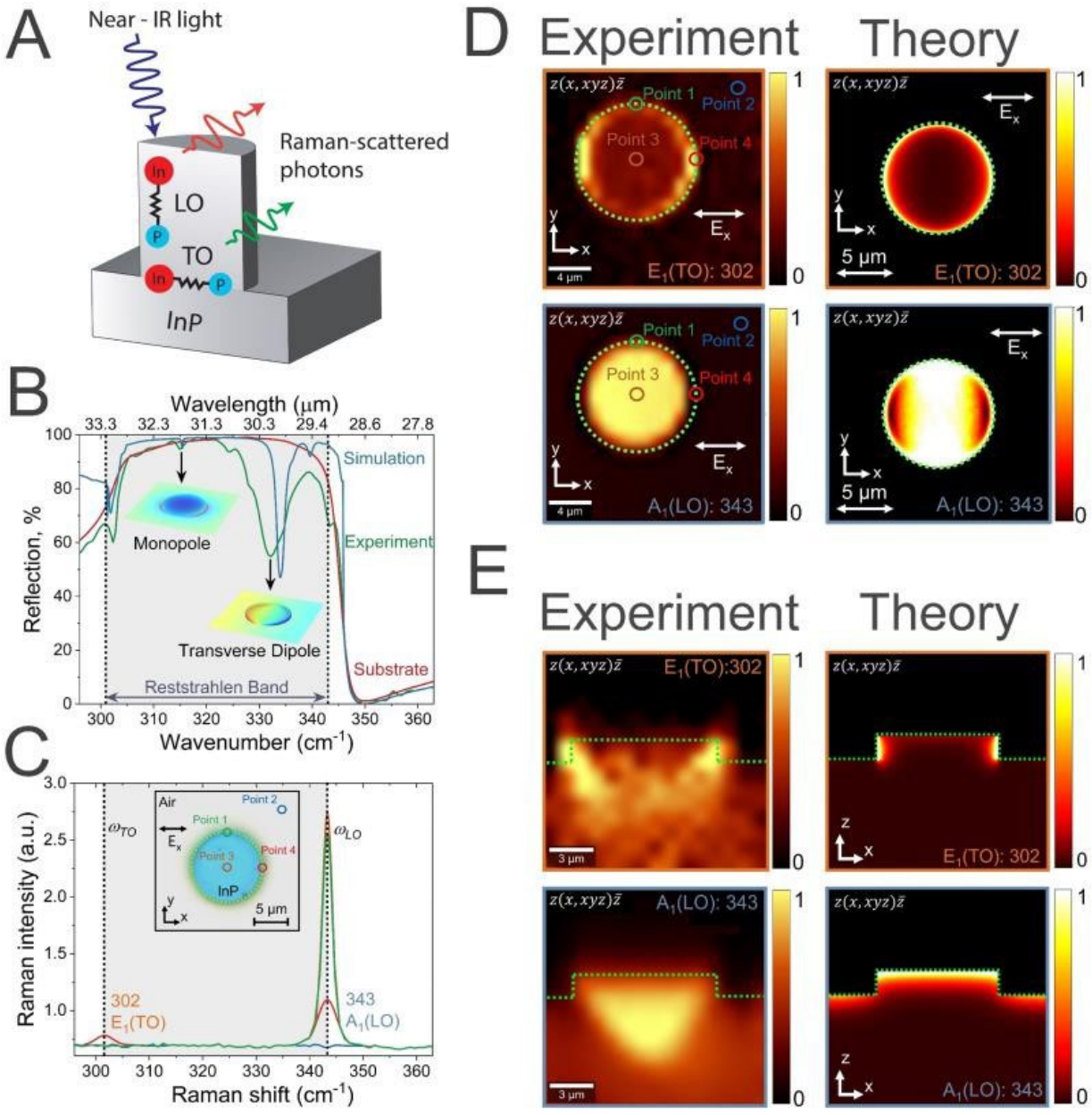

*Figure 4.1* ***Phonon-SPhP coupling in InP nanopillars.*** *(**A**) Illustration of confocal Raman measurements on InP pillars. Near-IR light focused by the microscope objective produces Raman scattering from longitudinal and transverse optical phonons (LO and TO). (**B**) FTIR reflection spectrum of a periodic array of InP pillars (green curve) compared to the simulated spectrum obtained using COMSOL (blue curve) and the FTIR reflection of the InP substrate (red curve). Insets: Charge distribution of monopole and transverse dipole resonances. (**C**) Unpolarized, backscattering micro-Raman spectra measured at 4 different points (as shown in the figure inset, taken at a focus position roughly 0.5 μm above the pillar -substrate interface) across the top face an InP pillar, showing the spatial dependence of the LO and TO phonon modes, which bound the Reststrahlen band (gray shaded region) in (**B**). (**D**) (left) Experimentally measured and (right) theoretically simulated Raman intensity maps obtained for the 302 $cm^{-1}$ E1(TO) (upper panels) and 343 $cm^{-1}$ A1(LO) (lower panels) phonon modes for an x-y cross-sectional view, showing the distinct localization of Raman intensity for each phonon mode. The dotted green lines represent the InP-air interface. (**E**) Same as (**D**) for a y-z cross-sectional view.*

For the specific case of the *A*1(LO) and *E*1(TO) phonon modes in 4H-SiC, electron-phonon coupling also plays a role, even for low-doped substrates. These results challenge the conventional understanding of SPhP-phonon coupling and indicate that electrically pumped SPhP mid-IR emitters might be achievable with dielectric nanostructures. Furthermore, our work provides a method for real-space mapping of SPhP eigenmodes in a manner analogous to tomographic EELS, but with no destructive sample preparation and not requiring the specialized equipment of highly monochromatic EELS. Thus, Raman imaging can be a complementary tool for visualizing SPhP modes, which also provides a natural platform for investigating the interactions between electrons, phonons, SPhPs, and other solid-state excitations.

## 4.2 Coupling between phonons and SPhPs – InP pillars

To investigate the correlation between Raman measurements and the near-field structure of the SPhP modes, we perform IR reflectance and scanning confocal Raman mapping measurements on arrays of cylindrical InP pillars with a radius of 10 μm and height of 1.5 μm, as depicted in Figure 4.1A (see methods measurement and sample details). To avoid photodoping and inadvertently phototuning the SPhP resonances while performing Raman measurements [48], we probe the

Raman spectra by employing a below-gap, near-IR laser centered at λ = 1064 nm.

As shown in Figure 4.1B, the measured IR reflectance spectrum for the InP pillar array (green curve) deviates significantly from measurements of the bare substrate (red curve), indicating the excitation of localized SPhP modes. These measurements are in excellent agreement with full-wave electromagnetic simulations (blue line). The InP pillars support two primary localized SPhP resonant modes superimposed on the highly reflective Reststrahlen band indicated by gray shading. Numerical calculations of the surface charge distribution at resonance indicate that the higher-energy resonance is a transverse dipole mode, consisting of charges localized at opposite ends of the pillar (see inset Figure 4.1B). The lower-energy resonance is a monopole mode, consisting of charge distributed across the pillar face (see inset Figure 4.1B). These mode profiles are similar to SPhP resonances observed in other nanopillar systems[21, 48]. The spatial profiles of these modes localized in the 10 μm radii pillars with an excitation wavelength of ~30 μm indicate the subdiffractional nature of the SPhP modes, and resonances at pillar radii below 1 μm are also observable (Fig. 4.7 ).

By scanning the sample and recording a Raman spectrum at each scan position, we obtain Raman images that reveal the full 3D spatial map of the phonon modes within the nanostructure. Figure 4.1C shows a first investigation of the Raman modes in the pillars: several micro-Raman spectra collected in the x-y plane at a focus point roughly 0.5 μm above the pillar-substrate interface. All of the Raman scans in Figure 4.1 were collected in the $z(x, xyz)\bar{z}$ geometry, where $z$ and $\bar{z}$ on either side of the parentheses denote the propagation direction of the incident and scattered light, $x$ denotes the polarization of the incident laser, and $xyz$ denotes the polarization of light collected for the detector (unpolarized, in this case). A representative $z(x, xyz)\bar{z}$ Raman spectrum for InP (Figure 4.1C, brown line corresponding to Point 3 at the pillar center) reveals only two phonon modes: $E1$(TO) and $A1$(LO), which bound the Reststrahlen band (Figure 4.1B), as expected for a polar zinc blende crystal such as bulk InP [74]. As shown in Figure 4.1C, distinct spectral responses are extracted at different positions on the pillar face. In particular, at point 1 on the top edge of the pillar (green curve), the TO phonon has much stronger Raman scattering, and the LO phonon

scattering becomes suppressed. This dramatic change in the spectral intensity indicates that the Raman scattering by phonons demonstrates remarkable spatial dependence in the nanostructure geometry, in contrast to the uniform Raman intensity of a bulk material.

To further understand the phonon scattering behavior, we show Raman spectral images in the same "top-down view" (x-y plane) at the same focus position on the z-axis as Figure 4.1C, with the incident light polarized in the x-direction. Figure 4.1D shows the experimental (left panels) and simulated (right panels) intensity maps for the TO (upper panels) and LO (lower panels) phonon modes. The maps demonstrate that the *E*1(TO) intensity is localized at the pillar edges and aligned with the laser polarization, similar to the SPhP transverse dipole mode (Figure 4.1B inset). In contrast, the *A*1(LO) mode Raman map reveals a nearly uniform scattering intensity for the LO mode across the pillar face, like the SPhP monopole mode (Figure 4.1B inset). Images taken in the "cross-sectional views" (x-z plane) further support this conclusion, indicating that the scattering from the phonon modes is localized in a manner analogous to the SPhP modes. The Raman images provide evidence for our surprising finding that the TO and LO phonons interact with the distinct SPhP modes of the pillar, where the Raman scattering from the TO and LO phonon modes predominantly assumes the field morphology of the dipole and monopole SPhP resonances, respectively.

## 4.3 Field Mapping Theory

To understand the SPhP response in the Raman maps, we demonstrate a basic, first-order reconstruction method to model the spatial distribution of the Raman intensity within the nanostructures. Our approach relies on the quasistatic approach, justified by the relatively large free-space wavelengths of the SPhPs on resonance, which are much larger than the pillar dimensions [75]. Following this assumption, we use a simple eigenmode reconstruction method to calculate the SPhP Raman response, inspired by EELS reconstructions of SPP and SPhP eigenmodes.

The basis for our approach comes from the polarizability selection rules, which have been used to calculate the Raman scattering intensities of propagating PhP modes in VdW materials [73]. We modify this approach to make it more suitable for describing localized SPhPs in nanostructures by

expressing the Raman response of the nanostructure in terms of its resonant eigenmodes. Based on our observations in Figure 4.1(B-D), we propose expressing the electric field which produces Raman scattering inside the nanostructure in terms of the SPhP eigenmodes, which have spatial distribution $\bar{\boldsymbol{u}}_k(\bar{\boldsymbol{r}})$; where $\bar{\boldsymbol{r}}$ is the volume coordinate and $k$ indexes the eigenmode (e.g, the monopole or dipole mode) [76, 77]. This approach assumes that the electromagnetic fields of the mid-IR SPhP modes dominate the visible/near-IR Raman response via polarizability coupling. We will demonstrate that this approach provides a method to reconstruct the Raman intensity in the InP pillars, but is not expected to generally hold in situations when others effects (Mie resonances [78], nonlinear effects [79], other solid state excitations [80, 81], etc.) have to be considered. Using these eigenmodes, we construct the Raman polarization ($\bar{\boldsymbol{P}}_R$) induced in the structure as a result of Raman scattering [78, 82]:

$$\bar{P}_R = \overline{\overline{\alpha^\sigma}} \cdot E(\bar{r}) = C_k^\sigma \overline{\overline{\alpha^\sigma}} \bar{u}_\kappa(\bar{r}) = \bar{P}_{R,k}^\sigma \qquad 4.1$$

where $\overline{\overline{\alpha^\sigma}}$ is the Raman polarizability tensor for phonon mode $\sigma$ (e.g, $A_1$(LO) or $E_1$(TO) for InP), $\bar{\boldsymbol{E}}(\bar{\boldsymbol{r}})$ is the electric field inside the nanostructure (due to the excitation laser), and $C_k^\sigma$ is a coefficient which describes the coupling between the polarizability tensor of phonon mode $\overline{\overline{\alpha^\sigma}}$ and eigenmode $\bar{\boldsymbol{u}}_k(\bar{\boldsymbol{r}})$. The last equality emphasizes that 4.1) describes the Raman polarizability that is generated when an SPhP eigenmode couples with a phonon mode, imparting a spatial profile to the induced Raman polarizability.

While Eq. (4.1) contains the essential physics of the reconstruction process, it is the time-averaged Raman intensity that is measured. Using this approach, we write the time-averaged Raman intensity signal (in a volume element $dV$) in terms of its proportionality to the time-average of the Raman polarization amplitude

$$\langle I_{R,k}^\sigma \rangle \propto \langle |\bar{p}_{R,K}^\sigma| \rangle^2 \qquad 4.2$$

Equation 4.2 describes the Raman intensity for phonon mode $\sigma$ when coupled to SPhP mode $k$. Due to the assumed incoherent nature of the coupling between bulk phonons and SPhPs [78], we obtain the final expression for the Raman intensity of a given phonon mode by summing over the eigenmode basis:

$$\langle S_R^\sigma \rangle = \Sigma_k \langle I_{R,K}^\sigma \rangle \qquad 4.3$$

Equation 2 is similar to the expression for the Raman intensity of PhPs in 2D materials, where instead we have explicitly expressed the electric field in terms of the SPhP eigenmodes, which is the natural approach for localized polaritons in nanostructures. This representation also emphasizes the formal analogy to EELS reconstruction of SPhP modes, where Raman intensity maps can be used to visualize the SPhP eigenmodes comparable to EELS tomography of the local electromagnetic response driving light-matter interactions, the electromagnetic local density of states [69]. Our theoretical formalism is thus based on the notion that the induced Raman polarization (and hence Raman intensity) exhibits spatial dependence consistent with coupling to the polarization of the SPhP eigenmodes. Therefore, the measured Raman intensity for a given phonon mode in an InP pillar can be reconstructed as the combination of the SPhP eigenmodes subjected to the Raman selection rules for that phonon symmetry contained in $\overline{\overline{\alpha^\sigma}}$.

We demonstrate that the spatially dependent Raman scattering originates in coupling to SPhPs by calculating the Raman polarization in the pillars. Full-wave electromagnetic simulations (COMSOL) are used to obtain the field distributions associated with the SPhP monopole and dipole modes. Then, using the Raman selection rules for each phonon mode, the Raman polarization for a given phonon mode is obtained via Eq. 4.1. The results of time-averaging the Raman polarization intensities and summing over the eigenmodes are presented in the right panels of Fig. 1D, E (further details on the reconstruction process are given in the supplementary information). The simulations reveal similar features to those seen in the experimental Raman maps, shown in the left panels. The simulated fields confirm that the Raman polarization for the TO and LO phonon modes predominantly displays the morphology of the SPhP dipole and monopole resonances, respectively. This surprising discovery is not unreasonable given that the

SPhP dipole is a transverse, in-plane mode and the TO phonon oscillates in-plane (and vice versa for the monopole mode and LO phonon). The Raman mapping of InP nanopillars indicates that

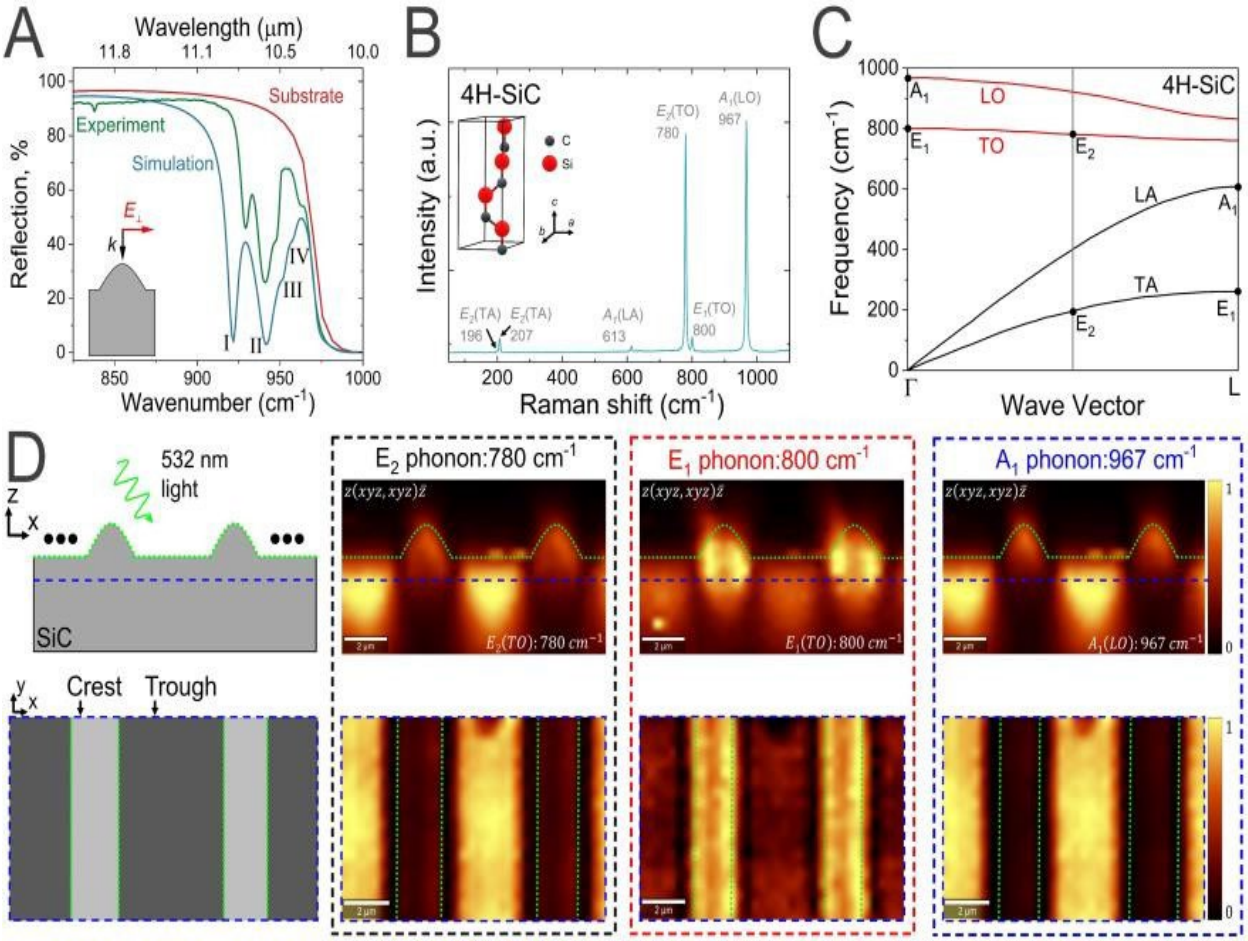


*Figure 4.2* ***1D SiC gratings.*** *(**A**) FTIR reflection spectrum of SiC gratings (red curve) compared to the simulated spectrum obtained using COMSOL (green curve) and the reflection from the SiC substrate (black curve). Inset: illustration of the SiC grating unit cell. (**B**) Representative $z(x, x)\bar{z}$ Raman spectrum of 4H-SiC. All of the Raman-active phonon modes are labeled with their symmetry classification. Inset: Illustration of the 4H-SiC crystal structure. (**C**) Phonon dispersion curve of 4H-SiC based on Raman data. The dots denote all Raman-active phonon modes in the backscattering configuration. (**D**) (Top) x-z and (bottom) x-y unpolarized Raman maps of the three optical phonons in 4H-SiC: E2(TO), E1(TO), and A1(LO). The dotted green lines show the SiC-air interface and the dotted blue lines denote the z-position of the x-y map (~ 1 μm below the SiC substrate).*

the bulk phonons couple to the surface phonon polaritons through the material polarizability, enabling the 3D depth-profiling of SPhP modes in real space with a near-IR probe.

## 4.4 Coupling Between Phonons and SPhPs – SiC

To further demonstrate the power of Raman mapping as a technique to investigate SPhP modes, we fabricated a 1D grating on 4H-SiC with a period of 6 μm, a linewidth of 3.3 μm, and a height of 1.3 μm (see methods for details). The grating structure supports a variety of localized SPhP modes, as shown in the measured (red curve) and simulated (green curve) IR reflection spectrum of the nanostructure shown in Figure 4.2A (a schematic of the unit cell is shown in the inset). In contrast to the symmetric InP pillar structure, the localized SPhP modes on the SiC grating cannot be simply described as monopole or dipole modes and thus possess more complicated fields.

The electric field distributions for all four modes are presented later in Figure 4.10. Nevertheless, we can take the set of SPhP resonances (which we denote as I,II,III, and IV in Figure 4.2A) and use them as the basis for a more complicated Raman reconstruction. Figure 4.2B shows a representative $z(x, x)\bar{z}$ Raman spectrum for 4H-SiC, whose crystal structure is shown in the inset. The wurtzite (hexagonal) structure of 4H-SiC supports 6 Raman-active phonon modes in the backscattering configuration: three acoustic phonons lie in the range 207 $cm^{-1}$ – 613 $cm^{-1}$, and three optical phonons lie in the Reststrahlen band (780 $cm^{-1}$ – 967 $cm^{-1}$), all of which fall into three symmetry classes: $E_2$, $E_1$, and $A_1$, as shown in the phonon dispersion of Fig. 4.2C.

As a first investigation of the Raman modes in the SiC gratings, we collect unpolarized $z(xyz, xyz)\bar{z}$ Raman maps, as presented in Fig. 4.2D. We consider two separate mapping configurations: a cross-sectional view in the x- z plane and a top-down view in the x-y plane (collected at a point ~ 1 μm below the SiC substrate), depicted with schematic illustrations in the left panel of Fig. 4.2D. The right three panels of Fig. 4.2D show the Raman maps for the three optical phonon modes: $E_2$(TO) (dashed black box), $E_1$(TO) (dashed red box), and $A_1$(LO) (dashed pink box).

Figure 4.2D reveals that, as in the InP pillars, Raman maps corresponding to phonons of different symmetry groups produce spatial profiles with distinct phonon localization.

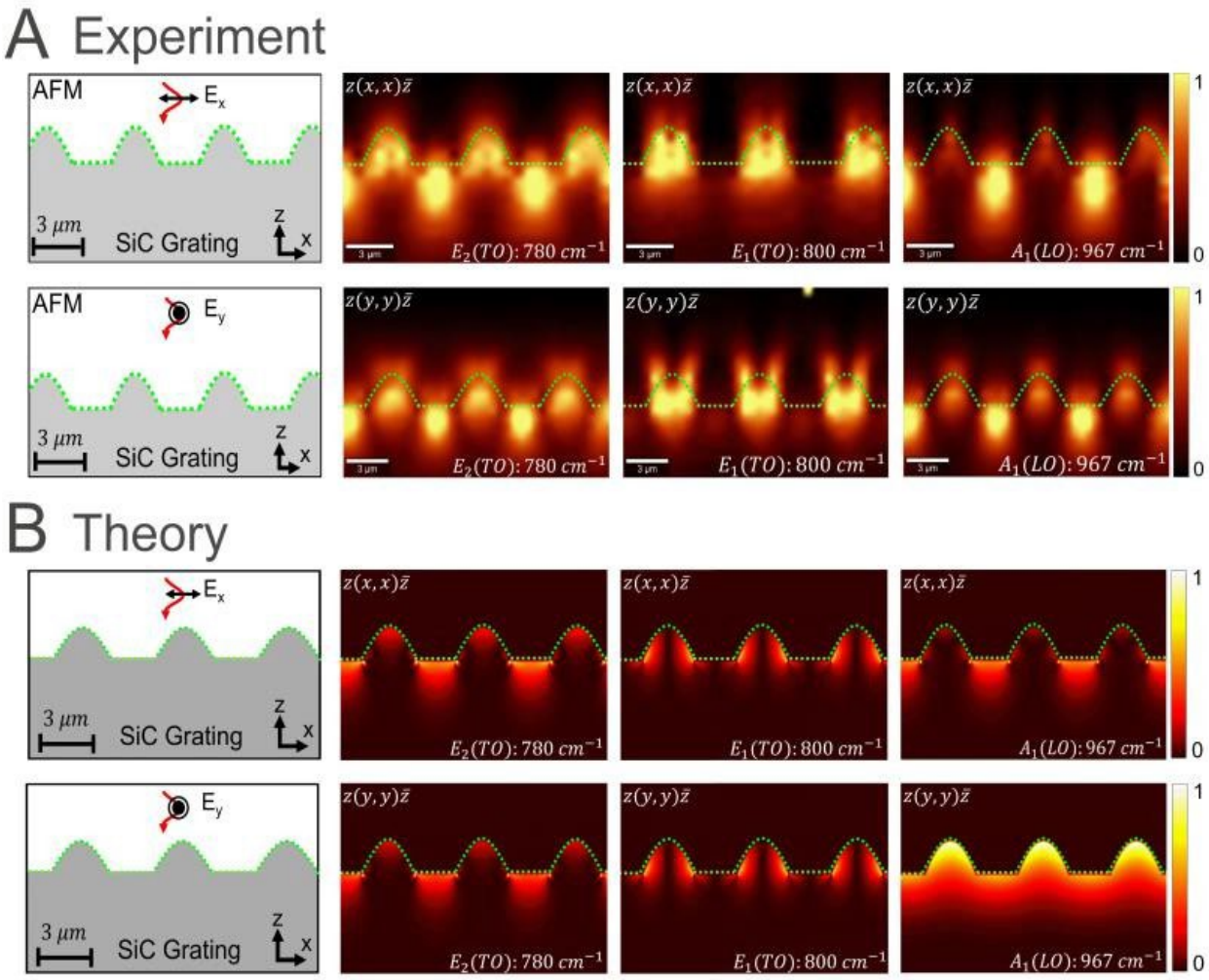


*Figure 4.3 Raman mapping of phonon-SPhP coupling: SiC gratings. (A) (Left) Experimental non-contact AFM topography scans of the grating surface and (right) Raman intensity maps of the three optical phonon modes (E2(TO), E1(TO), A1(LO)) for two geometric configurations ($z(x, x)\bar{z}$ and $z(y, y)\bar{z}$). The outline of the grating is highlighted with dotted green lines. (B) Same for full wave electromagnetic simulations of a 1D SiC grating.*

For a more thorough analysis, we present in Fig. 4.3A Raman intensity maps of the experimentally observed phonon modes $E_2$(TO), $E_1$(TO), and $A_1$(LO) for two different polarizations ($z(x, x)\bar{z}$ and $z(y, y)\bar{z}$, all four polarization combinations are presented later in Figure 4.13). The leftmost panel

of Fig. 4.3A shows atomic force microscopy (AFM) scans of the SiC grating surface, demonstrating the parabolic appearance of the "crest" which rises above the substrate "trough". As in Fig. 4.2D, the experimental Raman maps showed distinct differences among the phonon modes: the $E_2$(TO) phonon has pronounced intensity in both crest and trough areas, the $E_1$(TO) phonon mode has intensity concentrated in the crest area, and the $A_1$(LO) phonon mode has intensity concentrated in the trough area. The x-polarized maps generally resemble the y-polarized maps, with only small variations in the field differentiating both configurations (this is largely due to the high-NA objective used in the experiment)

As shown in Fig. 4.3B we also performed calculations of the time-averaged Raman intensity via Eqs. 4.1-4.6, employing the same model used to calculate the Raman response in the InP pillars.

Simulations of the SPhP eigenmodes in the grating structure were aided by the AFM measurements of the grating to accurately recreate the surface geometry. The simulations reproduce the spatial variation that is observed experimentally, supporting the observation that the E1 mode is concentrated in the crests and the A1 mode is concentrated in the troughs, while the E2 mode has intensity in both regions. The most notable deviation occurs for the $A_1$ map in the $z(y,\ y)\bar{z}$ geometry, where the simulation predicts a more uniform polarization than is observed in the experimental map. Further work will be required to reveal why the selection rules applied to the SPhP modes don't reproduce the experimental map in this case. Nevertheless, the generally good agreement between the polarizability coupling theory and the Raman maps indicates that Raman mapping of SPhP modes is achievable when considering a more extensive set of eigenmodes, phonons, and polarization configurations than used to study the InP pillars

## 4.5 Raman Mapping of Electron-Phonon Coupling

While our work supports the remarkable fact that bulk phonons and SPhP modes interact via polarizability coupling, the effects of electron-phonon coupling are also known to have an

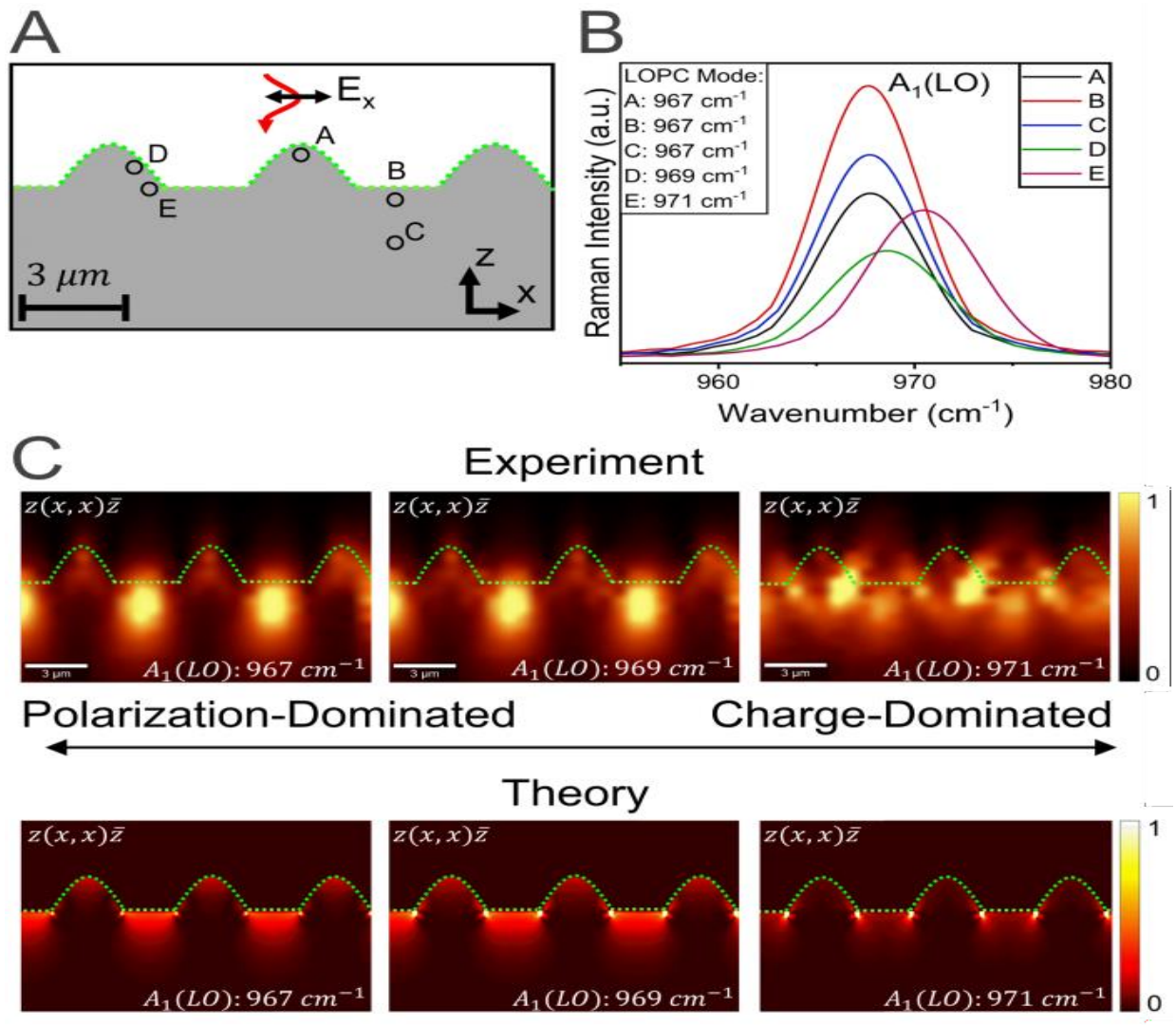


*Figure 4.4**Raman mapping of electron-phonon coupling in 4H-SiC.** (**A**) Schematic of the Raman mapping investigation of electron phonon-coupling. (**B**) Measured Raman spectra taken from different points on an x-z cross section of the grating, as shown in panel (**A**), in the z(x, x)z̄ setup. (**C**) (Top) Experimental and (bottom) theoretical Raman intensity maps of the LO peaks for three spectral positions of the LO peak at 967 $cm^{-1}$, 969 $cm^{-1}$, and 971 $cm^{-1}$.*

important impact on the Raman spectra of SPhP modes[48, 64, 70]. Free carriers interact with phonons via the coupling between the free electron plasma and LO phonons in ionic crystals, known as the longitudinal optical plasmon coupling (LOPC) effect. The LOPC effect is identifia LO peak due to damping from the lossy plasmonic field [83]. The electron-phonon coupling seen

through the line shape of the LO phonon mode is thus a widely used method to investigate the electrical properties of SiC and is frequently employed to estimate the doping density of SiC samples [83].

This well-established role of Raman spectroscopy in investigating the LOPC effect prompts the idea of using Raman mapping as a way of visualizing the charge distribution induced by the surface modes. In Fig. 4.4B, we show Raman spectra obtained from different points in the grating structure - as indicated in the cross-sectional view in Fig. 4.4A. The Raman spectra indicate that the LO mode maintains it spectral position at 967 $cm^{-1}$ for most points in the grating, but near the grating corner (points D and E) the spectral characteristics of the LOPC effect emerge as the LO mode blue shifts to 971 $cm^{-1}$ and broadens. This relatively small shift corresponds to a charge density of $n$= $5.0\times10^{17}$ $cm^{-3}$, more than two orders of magnitude larger than the estimated doping of the SiC substrate layer ($\sim1.0\times10^{15}$ $cm^{-3}$)

We show the experimental Raman maps associated with the LO phonon mode as it shifts from 967 $cm^{-1}$ to 971 $cm^{-1}$ in Fig. 4C. These maps support the observations of Fig. 4.4B, indicating that as the LO mode blueshifts the Raman signal becomes strongly concentrated in the grating corners due to the corresponding concentration of charge. We compare these maps with theoretical simulations including both the polarizability (following the same selection rules basis as before) and the influence of adding the induced charge (more detail on the LOPC simulations is provided in the supplementary information). The simulations further support experimental observations that increasing densities of free carriers concentrate themselves in the grating corners and thus lead to a spectral shift of the Raman signal in these regions. The observations indicate that confocal Raman microscopy can serve as a powerful tool for visualizing the electron-phonon coupling effects in certain material systems.

In this work, we demonstrated the three-dimensional mapping of phonon polariton modes in nanopillars of Indium Phosphide and one-dimensional gratings of 4H-Silicon Carbide using visible and near-infrared confocal Raman microscopy. This mapping technique is enabled by the unexpected coupling of bulk phonon modes to the phonon polaritons via changes in the local

polarizability, described by the Raman selection rules for each phonon mode. In addition, for $A_1$(LO) and $E_1$(TO) in 4H-SiC we observe that free charges also couple to the phonon modes, consistent with the well-known longitudinal optical phonon coupling (LOPC) effect. These observations constitute a method to visualize not only PhP eigenmodes, but also the light-matter interactions between phonons, polaritons, and charge distributions that occur in dielectric nanostructures. This proof-of-principle demonstration is thus promising for the wide range of applications, such as chemical sensing and nonlinear optics, where light-matter interactions are being intensely investigated, as well as in highly anisotropic materials, where volumetric mapping of light-matter interactions is a powerful capability. Furthermore, this work demonstrates a path for extending phonon polaritons physics that have been restricted to wavelengths above 5 μm into the visible regime. For example, the coupling of phonon polaritons to bulk phonons could enable the use of phonon polaritons in applications such surface enhanced Raman scattering (SERS) not previously explored.

## 4.6 Sample preparation

In the following section, we describe the sample preparation procedures for the InP nanopillar structures and the SiC grating samples. InP nanopillar samples were prepared in 300 x 300 μm arrays with varying diameter and pitch. The structures were fabricated on undoped n-type InP, using a SiN hard mask to outline the pillar cross-section. The mask was produced using electron-beam lithography with a fluorine-based inductively coupled plasma etching (ICP). The pillars themselves were then etched into the substrate using a chlorine-based ICP [48]. As discussed earlier, the InP nanopillars used for this investigation had a diameter of 10 μm, height of 1500 nm, and a center-to-center pitch of 20 μm. The SiC grating samples were prepared in 200 x 200 μm arrays with varying pitch and linewidth. The structures were fabricated on an undoped 4H-SiC substrate, which had its surface prepared and activated via a ozone treatment in the Plasma Preen system. The 1D grating pattern was then generated using maskless direct laser writing using a Nanoscribe 3D printer. The nanostructure pattern is applied to a drop of IP-DIP resin. The 3D printed map is then etched into the SiC substrate using a SF6/O2 reactive ion etching process with

O2 being used to remove any remaining polymer resist [45, 84]. The SiC gratings used for this investigation have a center-to-center period of 6 μm, a linewidth of 3.32 μm, and a height of 1.41 μm.

## 4.7 Surface topography measurements:

INP NANOPILLARS SEM IMAGES. Atomic force microscopy (AFM) maps were acquired using an NX10 AFM (Park Systems, South Korea) operating in noncontact mode using a silicon tip (PPP-NCHR; 42 N/m) with a nominal radius of < 10nm. The statistical analysis of the AFM maps was performed using XEI (Park Systems) software. Period, linewidth, and height were measured using a Z-axis cross section for the grating structure.

## 4.8 Reflection Spectroscopy:

Reflectance measurements for the InP nanopillars were carried out using a Bruker 80v spectrometer, coupled with a Bruker Hyperion 1000 IR microscope. For the SiC gratings, reflectance measurements were carried out using a Bruker Tensor 27 FT-IR spectrometer, coupled with a Bruker Hyperion IR microscope. A reverse-Cassegrain microscope objective was used for both experiments to focus unpolarized IR light onto the sample with an angle of incidence that varied from 12° to 23.6°. The same microscope objective was used to collect the reflected light from the nanostructure sample and subsequently focused onto and detected by a HgCdTe detector. Steady-state reflectance measurements were normalized to the reflectance of a gold mirror. Spectra were taken with an average of 80 scans with 3 $cm^{-1}$ resolution acquired from a 150 $\mu m^2$ collection area.

## 4.9 Raman measurements:

Raman spectra were recorded using a WITec Confocal Raman Microscope system (alpha 300R) with high-speed ultrahigh throughput spectrometers (WITec Inc., Germany). For all experiments, Raman signal was collected using a 100x (0.90 NA) Zeiss EC Epiplan-Neofluar objective (Zeiss,

Germany) with a 50 – μm optic fiber, dispersed by a diffraction grating of 600 grooves/mm, and collected on a EMCCD detector. For the investigations on InP, Raman spectra were collected using a frequency-

doubled Nd-YAG laser (WITec) providing excitation at an above-bandgap wavelength of 1064 nm perpendicular to the sample surface. For the SiC gratings, a laser excitation at 532 nm was employed. The linear polarization of both excitation lasers was adjusted using a λ/2 calcite waveplate, along with an identical λ/2 waveplate serving as the analyzer. Rayleigh scattered light was blocked by an edge filter. For the InP experiments, laser power was set to the 15 mW range, and satisfactory signal-to-noise ratio was achieved using an acquisition time of 12 s. For the SiC experiments, laser power was set to the 30 mW range, and satisfactory signal-to-noise ratio was achieved using an acquisition time of 7.5 s. For the InP nanopillars, fifteen confocal 2D (*x*-*y*) Raman maps (20 μm by 20 μm, 30 points per line, and 30 lines per image) from different focal planes (1.5 μm) were acquired at high spectral and spatial resolution by automatically scanning the sample along the z-axis (starting with the focal plane above the nanostructure surface and then focusing the beam progressively deeper into the nanostructure in 1.5 μm intervals). Data acquisition, evaluation, and processing were performed using the WITec Project Management and Image Project Plus software.

## 4.10 Electromagnetic Field Simulations:

We used the finite element method (FEM) software COMSOL Multiphysics to simulate the far-field reflection spectrum from both the InP nanopillars and SiC gratings (Fig. 4.1C and 4.2A, respectively). For these calculations, the reflection spectrum was calculated for an infinite array of the nanostructures with dimensions chosen to match the measured size of both nanostructures. Near-field simulations of the electromagnetic fields (including the polarization fields) are similarly performed using the RF module of COMSOL. Simulations are performed for incident angles of 0°, 32°, and 64°, and the optical fields shown (Fig. 4.1E,F; Fig. 4.3, and Fig 4.4C) consist of

equally weighted maps for each angle.

### 4.10.1 Electron-Phonon Coupling Simulations:

The process of determining the spatial profile of electron-phonon coupling, shown in Fig. 4.4C, requires simulating the distribution of induced charges in the SiC gratings. Volume charge distributions (at point **r** and frequency ω) in the nanostructure are obtained, following the approach of Marty [85, 86], as the divergence of the polarization vector:

$$\rho(\boldsymbol{r}, \omega) = -\nabla \cdot \boldsymbol{P}(\boldsymbol{r}, \omega) \qquad 4.4$$

Maps of the charge distribution measured are reconstructed in the same manner as the polarization fields, as described in the next section. In order to estimate the amount of induced charge in the nanostructures, the shift in the Raman spectra is used to approximately determine the induced charge density. As mentioned in the main text, in the Raman spectrum of polar dielectrics like SiC, the spectral position of the LO phonon peak will blueshift and broaden its full-width half maximum when the dielectric is doped with free carriers (the LOPC effect). This effect occurs because the large dipole moment of the LO phonon can couple to the electron plasma (an effect which becomes more prominent as the doping density increases). Using the Raman spectra, the carrier density of 4H-SiC in the low-doping regime is estimated using the approach of Nakashima, where the blueshift of the LO mode, $\Delta\omega$, is related to the carrier density $n$ via a simple expression [83]:

$$n = 1.25 \times 10^{17} \Delta\omega \qquad 4.5$$

For the bulk SiC substrate, there is no measured blueshift, indicating the very low background doping. Nevertheless, in very concentrated positions in the grating structure, a blueshift of up to $\Delta\omega = 5\ cm^{-1}$ is observed in the Raman spectra (Fig. 4.4B). To test the hypothesis that the local blue shifting is due to the electron-phonon coupling effect, we simulated both the polarization and

charge distribution in the 1D gratings. Using Eq. 4.6 above, we can estimate the induced charge in the nanostructures from the spectral shift in the LO phonon at that location. To obtain the maps shown in Fig. 4.4C, the polarization field of the SPhP modes based on the Raman tensor is computed (identical to Fig. 4.3 for the LO mode), which serves as the baseline for spectra with no blue shifting. For larger carrier densities, the induced charge is computed using Eq.4.4 S1, and the final maps are a combination of both polarization and charge maps.

## 4.11 Reconstruction

The process to reconstruct the maps of SPhP modes (Fig. 4.1D, E, Fig. 4.3, Fig. 4.4C) generally follows the logical approach of EELS reconstruction [69, 87, 88]. Procedurally, the Raman maps are constructed using an eigenmode decomposition, as in EELS, where the overall Raman scattering probability for a given phonon mode can be written as

$$\mathcal{P}_{Raman} = \sum_{k} C_k \mathcal{P}_{Raman}(U_k) \qquad 4.6$$

where the sum is performed over the index *k*, associated with a geometric SPhP eigenmode $u_k$ (such as a monopole in the nanopillars), $C_k$ is a coefficient specific to each geometric eigenmode, and $\mathcal{P}_{Raman}(u_k)$ is the Raman scattering probability generated from each SPhP eigenmode, calculated from the Raman selection rules. Unlike most EELS experiments, we do not seek to algorithmically obtain $u_k$ and $C_k$ that provide the best match to experimental data, although that will likely be a future direction when theoretical knowledge of Raman mapping of SPhP is further investigated. Rather, in our work, we obtain the eigenmodes $u_k$ from the reflection spectrum, sharp dips are identified as eigenmodes and constitute the basis set. Additionally, for simplicity, we arbitrarily set all coefficients $C_k$ to be equivalent (1, in this case), so that each simulated Raman map is an admixture of the Raman scattering probability associated with each SPhP mode. We anticipate that if even more precise methods are used to obtain the eigen basis and coefficients, then the matching between experiment and simulations might be improved substantially,

particularly the effect of the substrate.

## 4.12 Characterization of InP Nanopillar Arrays

The geometry of the InP pillar nanostructures was estimated from SEM imaging. The SEM images in Fig. 4.5 a, b demonstrate two periodic arrays of nanopillars with different characteristic dimensions. Fig. 4.5a shows the SEM image of the nanopillar array used in this paper's investigation of Raman maps, with a measurement of the top diameter overlaid. Fig. 4.5b shows an array of nanopillars with a smaller diameter, which will be investigated in the following data.

Both nanopillar arrays support localized SPhP modes, as demonstrated in Fig. 4.5c,d, which give simulated reflection spectra using the full-wave, 3D electromagnetic simulation approach in COMSOL described in the Materials and Methods. For both nanopillar sizes, comparing the off-array reflection spectrum (black curve) with the on-array reflection spectrum (red curve) reveals that the nanopillars induce reflection dips associated with localized SPhP modes.

The SPhP modes of both nanopillar sizes can be mapped using Raman imaging techniques, as shown in Fig. 4.6. Figure 4.6 shows x-y Raman image cuts for four different nanopillar arrays, showing both the TO and LO mode for each nanopillar size selected. The image size is fixed at 20 μm x 20 μm.

The uppermost array in Fig. 4.6 corresponds to an array with a period of 20 μm and a diameter of 10 μm, which corresponds to the Raman images in the paper. As discussed in the paper, the correspondence between the TO(LO) phonon modes and the dipole(monopole) SPhP modes is evident. The panel below (period of 16 μm and diameter of 8 μm) shows similar images of the localized modes. The next panel below (period of 10 μm and diameter of 5 μm) shows multiple nanopillars within the array. While the obtained maps have become blurrier, the dipole and monopole field distributions remain evident and appear to be similar in each pillar of the array. The bottom panel (period of 6 μm and diameter of 3 μm) shows a map containing almost 12 full pillars. The persistence of monopole and dipole fields appears to be discernible, but the small size has made imaging difficult given the diffraction limitation. Nevertheless, the presence of localized

modes can be verified for nanopillar sizes far smaller than the SPhP wavelength (~30 μm) and is not isolated to larger nanostructures. The largest nanopillars are chosen for the paper since their images are the easiest to visualize.

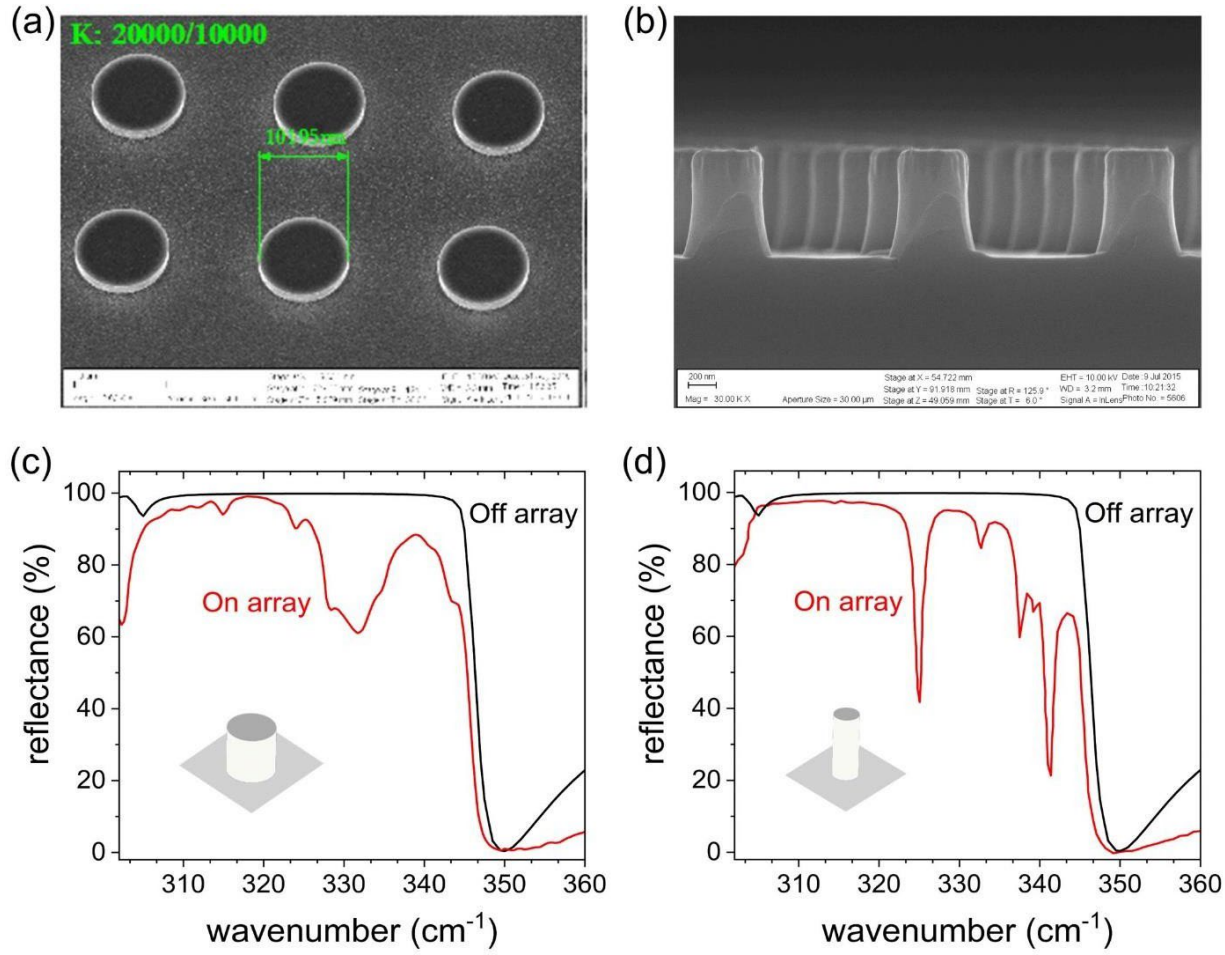


*Figure 4.5 SPhP resonances in InP nanopillars. A. SEM image of the InP nanopillars with 10 μm diameter, used in the paper. B. Cross-sectional SEM image of a nanopillar array with 300 nm diameters, far below the free-space polariton wavelength. C. Off array (black) and On-array (red) reflection spectra for the larger pillar array shown in panel (a) demonstrating the resonances associated with the localized SPhP modes. D. Off array (black) and on array (red) reflection spectra for the smaller pillar array shown in panel (b) demonstrating localized SPhP*

*resonances.*

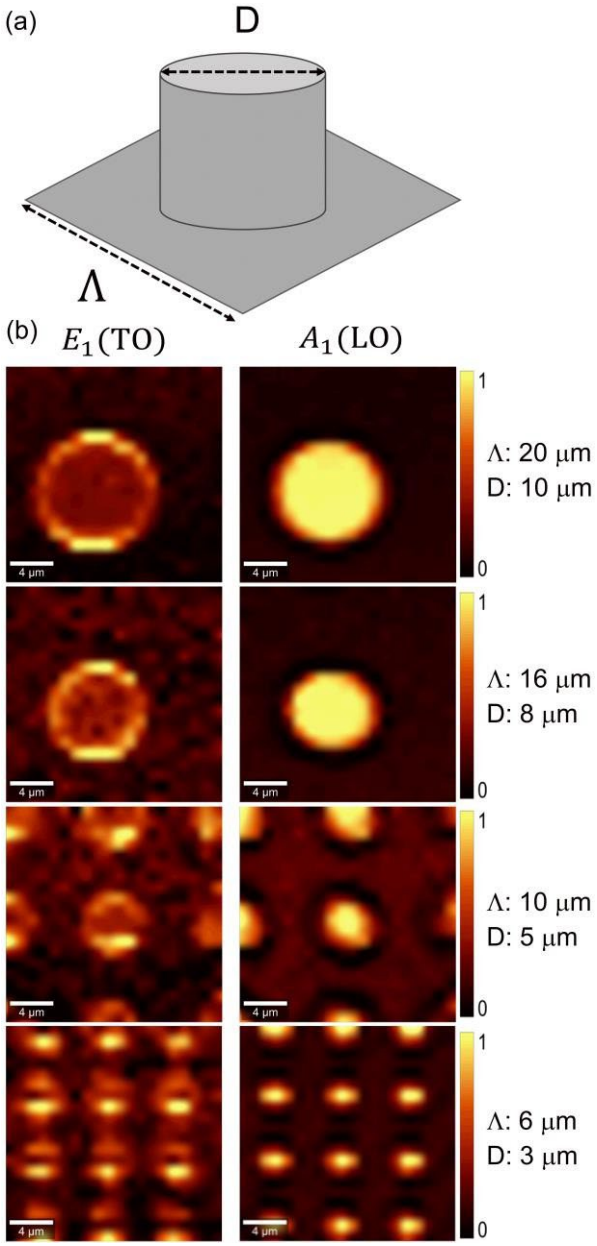


*Figure 4.6 Raman mapping for different nanopillar arrays. A. Sketch of the nanopillar geometry, with diameter (D) and period (Λ) shown. B. Raman images of the TO and LO phonon modes for nanopillars of different sizes. The top panel shows a Λ = 20 μm, D = 10 μm nanopillar, as shown*

*in the paper. Lower panels show nanopillars of decreasing feature sizes, demonstrating the continued confinement of the optical mode, with limited imaging resolution.*

Figure 4.1 gives both x-y and x-z Raman maps for the largest nanopillar array, but x-y Raman scans were also collected for various focal depths in the order to visualize the mode intensity in the nanopillar and within the InP substrate , as depicted schematically in Figure 4.7. As Figure 4.7 Stack Scan of InP nanopillars. (A). Sketch of the experiment, where Raman maps in the x- y plane are collected at a constant z-focus, generating a stack of Raman maps from A to J, focusing progressively deeper. (B) Results of the stack scan measurements for the E1(TO) and A1(LO) phonon modes. The monopole-like LO mode has a similar field profile for almost the entire stack scan but the dipole-like TO mode profile becomes very noisy and more monopole-like as it progresses deeper into the substrate. shows, we start at "Stack A" collected roughly 3.5 μm above the InP substrate and scan progressively down to "Stack J" roughly 1.5 μm into the substrate. Figure 4.7(b) demonstrates the result of these scans for the TO and LO phonons in the 10 μm diameter nanopillar. As the scans focus deeper into the InP substrate, we can visualize the monopole-like and dipole-like modes evolve through the vertical direction. In particular, the dipole-like TO phonon map has its profile fall apart and become noisier, while the monopole-like mode retains a strong profile through Stack J.

The results of the stack scan reinforce Figure 4.1(D) from the paper, where the cross-sectional map shows the TO mode losing its dipole-like field profile ~1.5 μm deep into the substrate, while the monopole remains strong over a larger distance. The results of these stack scans are also largely consistent with other investigations of SPhPs in nanopillars, which have noted the strong interaction of the monopole mode with the material substrate, necessary to maintain its charge neutrality.

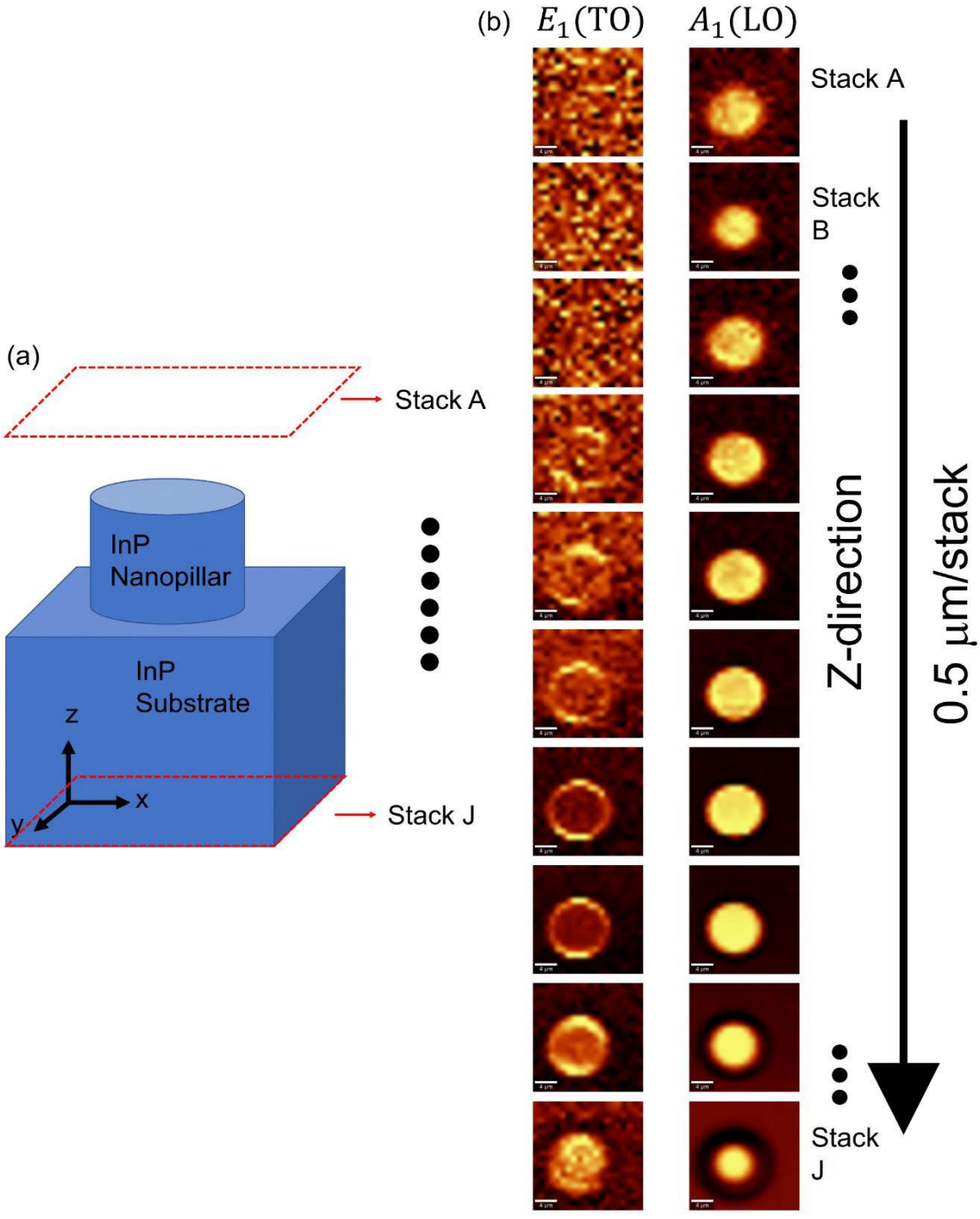
(a)
Stack A
InP
Nanopillar
InP
Substrate
z
x
y
Stack J
(b)
$E_1$(TO)
$A_1$(LO)
Stack A
Stack
B
Stack
J
Z-direction
0.5 μm/stack

*Figure 4.7 Stack Scan of InP nanopillars. (A). Sketch of the experiment, where Raman maps in the x- y plane are collected at a constant z-focus, generating a stack of Raman maps from A to J, focusing progressively deeper. (B) Results of the stack scan measurements for the $E_1$(TO) and $A_1$(LO) phonon modes. The monopole-like LO mode has a similar field profile for almost the entire stack scan but the dipole-like TO mode profile becomes very noisy and more monopole-like as it progresses deeper into the substrate.*

## 4.13 Characterization of One dimensional (1D) SiC Gratings

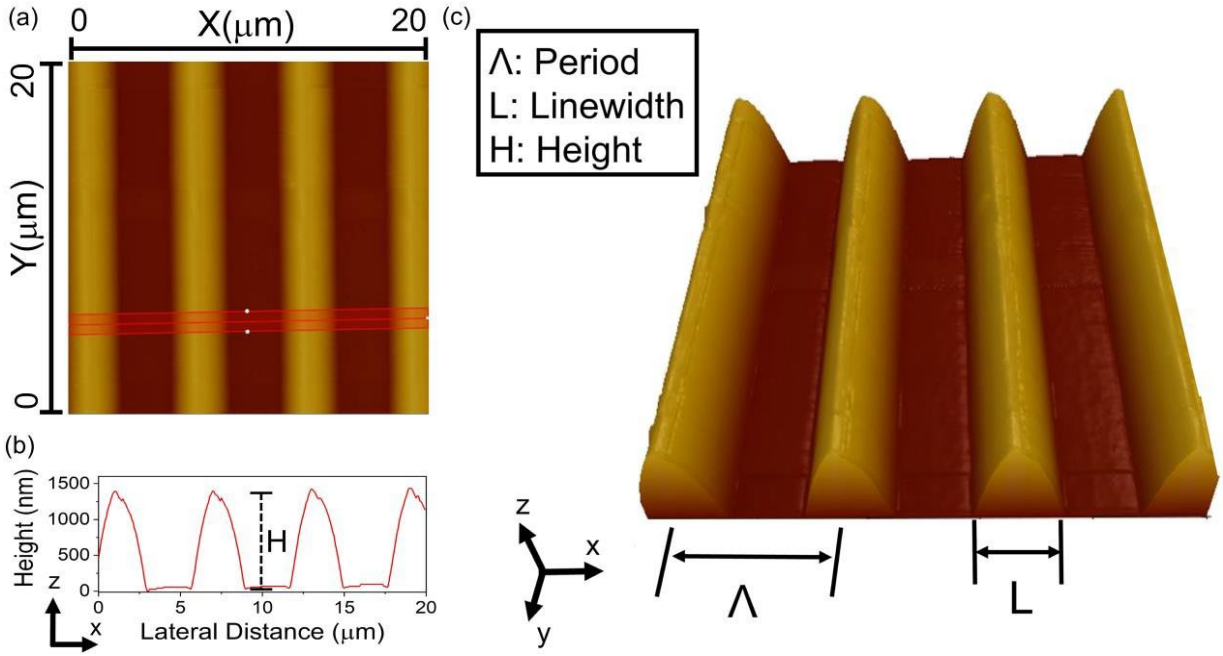


*Figure 4.8 AFM measurements of SiC gratings. (A). x-y AFM scan for 1D grating used in the article, the red line shows the cut where z values are averaged to produce a cross-sectional profile. (B) cross-sectional profile of grating structure in the x-z plane, used to extract all geometric parameters used in modelling. The height H is shown. (C). 3D view of the gratings which gives a clear view of the parabolic geometry produced by the etching process. The period Λ and linewidth L are shown.*

The geometry of the SiC gratings were measured using non-contact atomic force microscopy (AFM). Figure 4.8 AFM measurements of SiC gratings. (A). x-y AFM scan for 1D grating used in the article, the red line shows the cut where z values are averaged to produce a cross-sectional profile. (B) cross-sectional profile of grating structure in the x-z plane, used to extract all geometric parameters used in modelling. The height H is shown. (C). 3D view of the gratings which gives a clear view of the parabolic geometry produced by the etching process. The period Λ and linewidth L are shown. shows the results of the AFM measurements on the grating array used in the article. Fig 4.8(a) shows a x-y view of the AFM showing the location of the y-cut which is used to measure the grating structural parameters. The resulting x-z linescan, shown in Fig. 4.8(b), provides a cross-sectional view of the grating. The AFM scans show the parabolic shape of the gratings, which is a result of the etching process employed on SiC. The cross-sectional scan also allows for a measurement of the average grating height H above the substrate, along with the average period Λ and bottom linewidth L, as shown in the full 3D scan in Fig. 4.8(c). With Λ, L, and H having been measured, we can use those parameters to obtain a parabolic fit for the grating structure of the form $z = ax^2+bx+c$, determining the value for parameters a,b, and c. These fits are then used to recreate the grating geometry used to simulate the SPhP modes in Fig. 4.2(a) and Fig. 4.9.

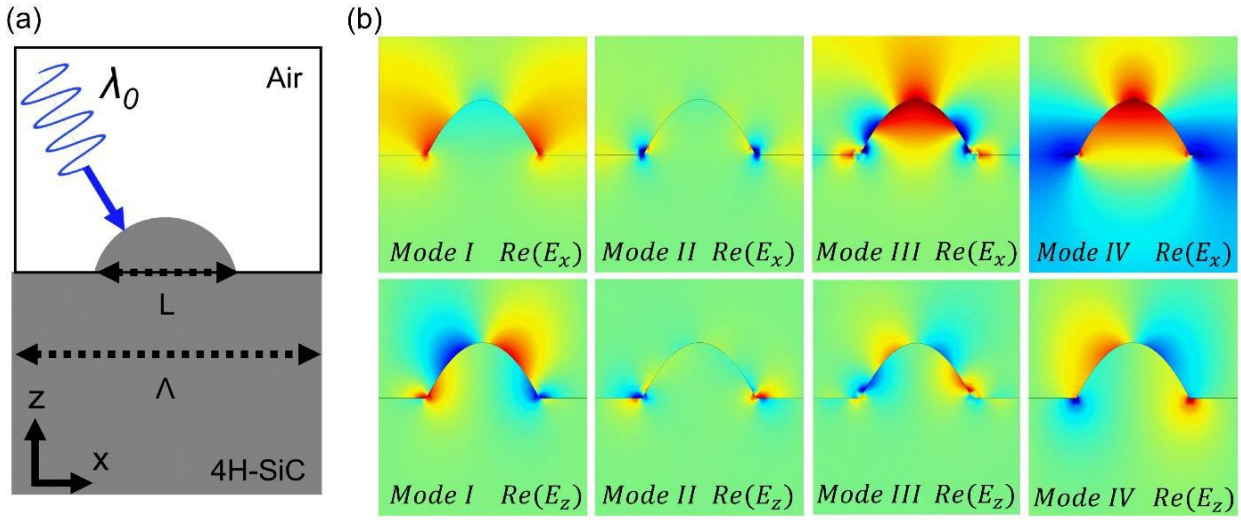


*Figure 4.9 FEM simulations of SPhP modes in SiC gratings. (A). Diagram of the computational geometry used for the modelling. The period Λ and linewidth L obtained in Fig. S4 are used to*

*create the structure. (B). The Re($E_x$) (top) and Re($E_z$) (bottom) distributions of the four SPhP resonances in the SiC gratings. Energies of modes I-IV are shown in Fig. 2(a) in the article.*

In Figure 4.9 we show the electromagnetic fields of the SPhP modes shown in Figure 2(a). Figure 4.9(a) presents a schematic of the computational unit cell. The 4H-SiC grating structure is built using period Λ, linewidth L, and height H as determined in Fig. 4.8. The structure is illuminated by light of wavelength $\lambda_0$, which is then swept to obtain the reflection spectrum. For each of the modes I, II, III, and IV labeled in Figure 2(a), we show the $E_x$ and $E_z$ fields in the nanostructure, demonstrating the subdiffractional confinement of electromagnetic energy by the SPhP modes. These 4 modes were selected to serve as the basis for the eigenmode reconstruction used to produce the simulated Raman maps in Fig. 3(b) and Fig. 4(b).

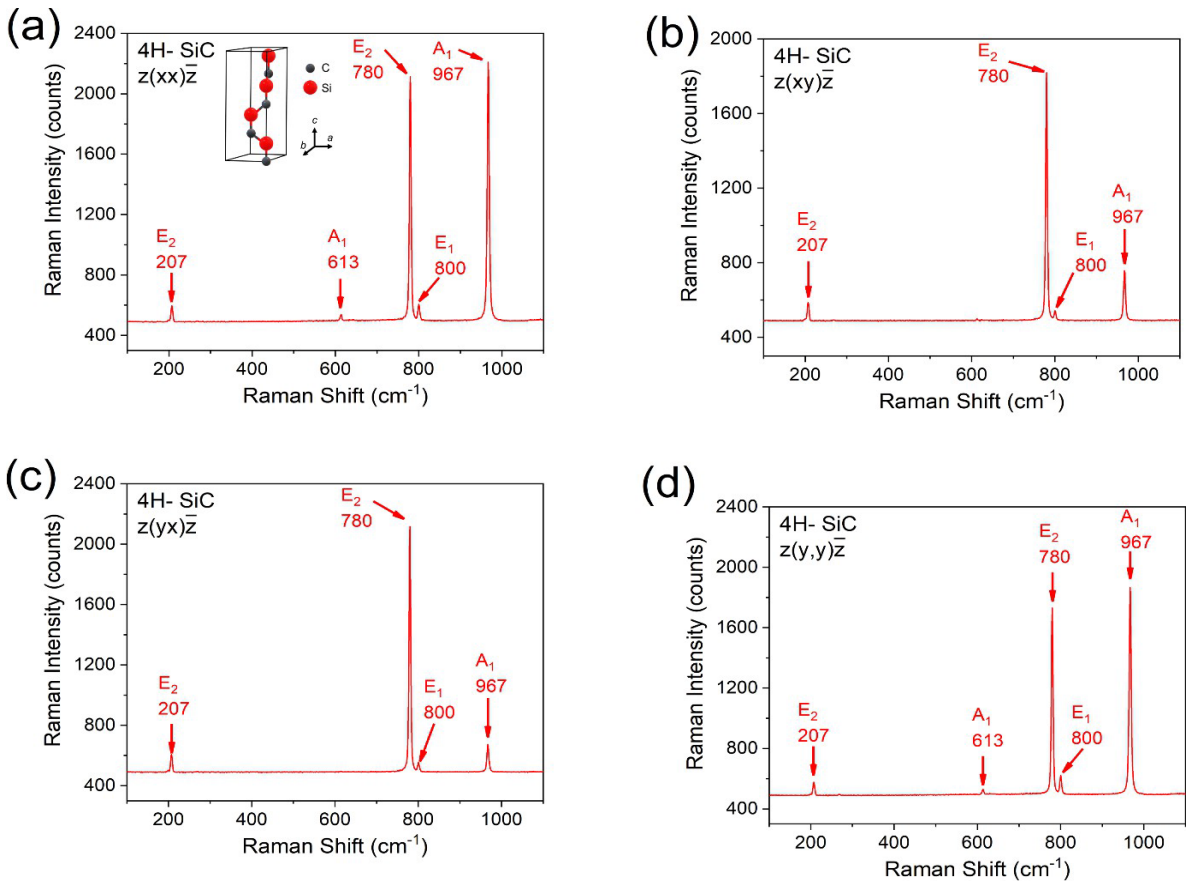

*Figure 4.10 Backscattering Raman spectra of 4H-SiC. We present the backscattering Raman spectra for bulk SiC material in all four polarizer-analyzer configurations: $z(xx)\bar{z}$ (a), $z(xy)\bar{z}$ (b), $z(yx)\bar{z}$ (c), and $z(yy)\bar{z}$ (d). Phonon modes are labeled by their symmetry classification.*

In Fig. 2(b), we show the $z(x,x)\bar{z}$ Raman spectrum for the 4H-SiC substrate in order to present the 6 Raman-active phonon modes measured. Since all four polarizer and analyzer combinations were used to obtain Raman maps of the SPhP modes, we measured the bulk Raman spectrum of 4H-SiC under all four polarizer-analyzer combinations as a reference. Figure 4.10 shows the measured Raman spectra for the $z(x,x)\bar{z}$ (a), $z(x,y)\bar{z}$ (b), $z(y,x)\bar{z}$ (c), and $z(y,y)\bar{z}$ (d) scattering geometries. These Raman scans show that both the parallel (xx and yy) and cross (xy and yx) have similarities. In particular, the parallel polarizations show all 6 Raman- active phonons with similar relative intensities. The cross polarizations lead to considerable decreases in the $E_1$ and $A_1$ phonon intensities, as predicted by the Raman selection rules.

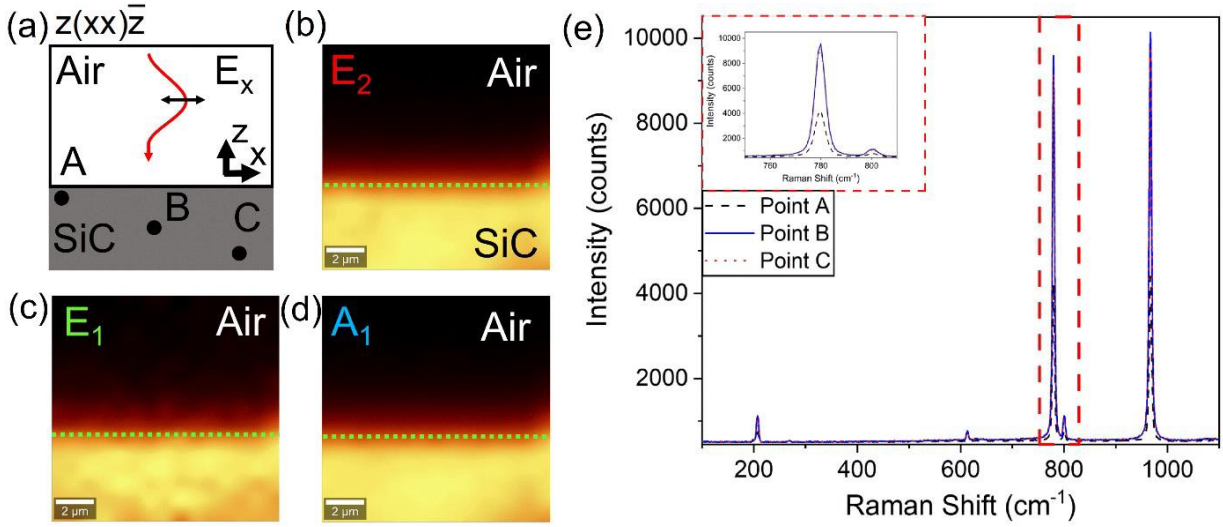


*Figure 4.11 Raman maps of bulk 4H-SiC. (A) Diagram of the experimental measurement. The incoming light is x-polarized incident on the SiC-air interface. Experimental maps of the Raman intensity are obtained for the $E_2$ (panel B), $E_1$ (panel C), and $A_1$ (panel D) phonon modes. (E).*

*Collected Raman spectra at the three points shown in panel (A), the intensities get stronger with increasing focus depth, but relative intensities remain constant.*

In addition to measuring the bulk Raman scattering in all polarizations, we also performed Raman mapping in the bulk SiC substrate. Figure 4.11(a) and Figure 4.12(a) show schematic representations of the SiC scattering geometries for both $z(x, x)\bar{z}$ (S7) and $z(x, x)\bar{z}$ polarization configurations. Using these setups, panels (b),(c), and (d) show the obtained Raman maps for all three optical phonon modes, $E_2$ (red), $E_1$ (green), and $A_1$ (blue). While there are variations in the signal-to-noise ratio among the phonon modes, all the Raman maps display the expected isotropy with uniform distribution, which distinguishes the bulk material from nanostructured 4H-SiC. Finally, Figure 4.11 (e) and Figure 4.12 (e) show the Raman spectra obtained at points A, B, and C in Figure 11,12 (a). There is expected depth dependence to the intensity of the Raman signals, but the relative intensities remain constant for all phonon modes, in contrast to the Raman signals in the SiC gratings, where the relative phonon intensities show high local variation (Fig. 4A, for example).

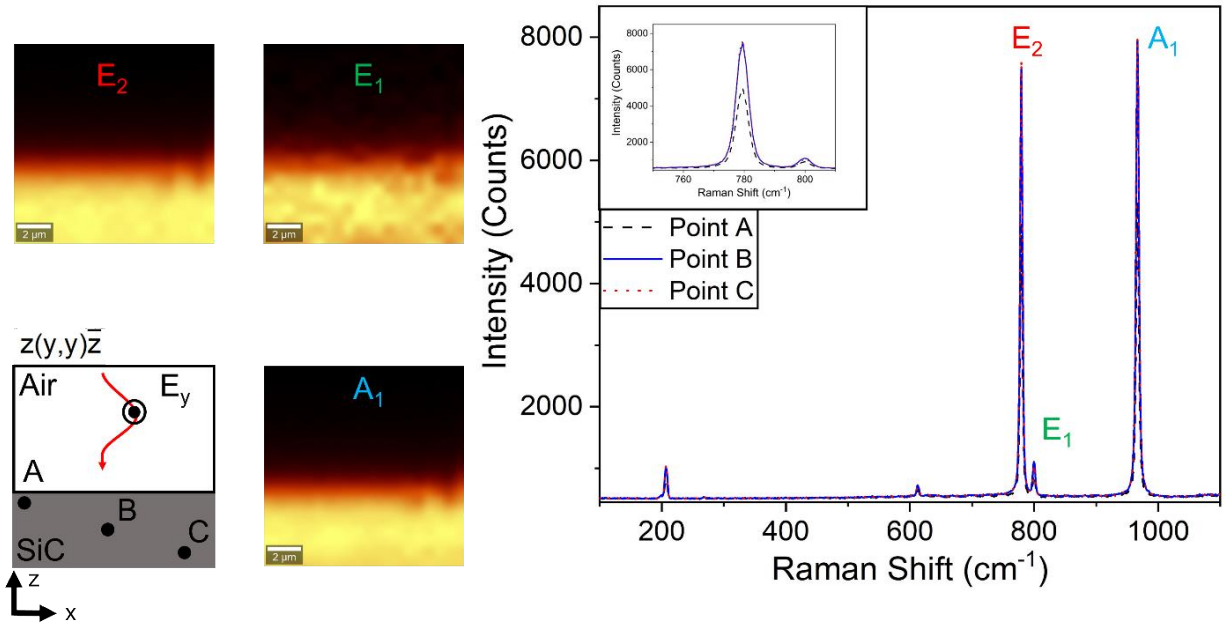

*Figure 4.12 Raman maps of bulk 4H-SiC. (A) Diagram of the experimental measurement. The incoming light is y-polarized incident on the SiC-air interface. Experimental maps of the Raman intensity are obtained for the $E_2$ (panel B), $E_1$ (panel C), and $A_1$ (panel D) phonon modes. (E). Collected Raman spectra at the three points shown in panel (A), the intensities get stronger with increasing focus depth, but relative intensities remain constant.*

As a complement to Fig. 4.9, in Fig. 4.13, we show the results of the Raman maps obtained for the three optical phonon modes in all four polarizer configurations. The left-most boxes denote the phonon symmetry, which all modes in that row correspond to: $E_1$ (green), $E_2$ (red), and $A_1$ (blue). The top panels denote the polarizer-analyzer configuration corresponding to its column and additionally outline the grating geometry with dashed green lines. As in Fig. 4.3, the Raman modes are largely similar across all the polarization configurations. Because the phonon modes mix polarizabilities in different directions, as the angle of incidence increases, the relative strengths of the polarizabilities change with the incident electric field. Thus, the large NA of our microscope objective acts to "smear" the Raman polarizabilities in both x and y polarizations. For a lower NA with a smaller solid angle, the selection rules might be more visually evident.

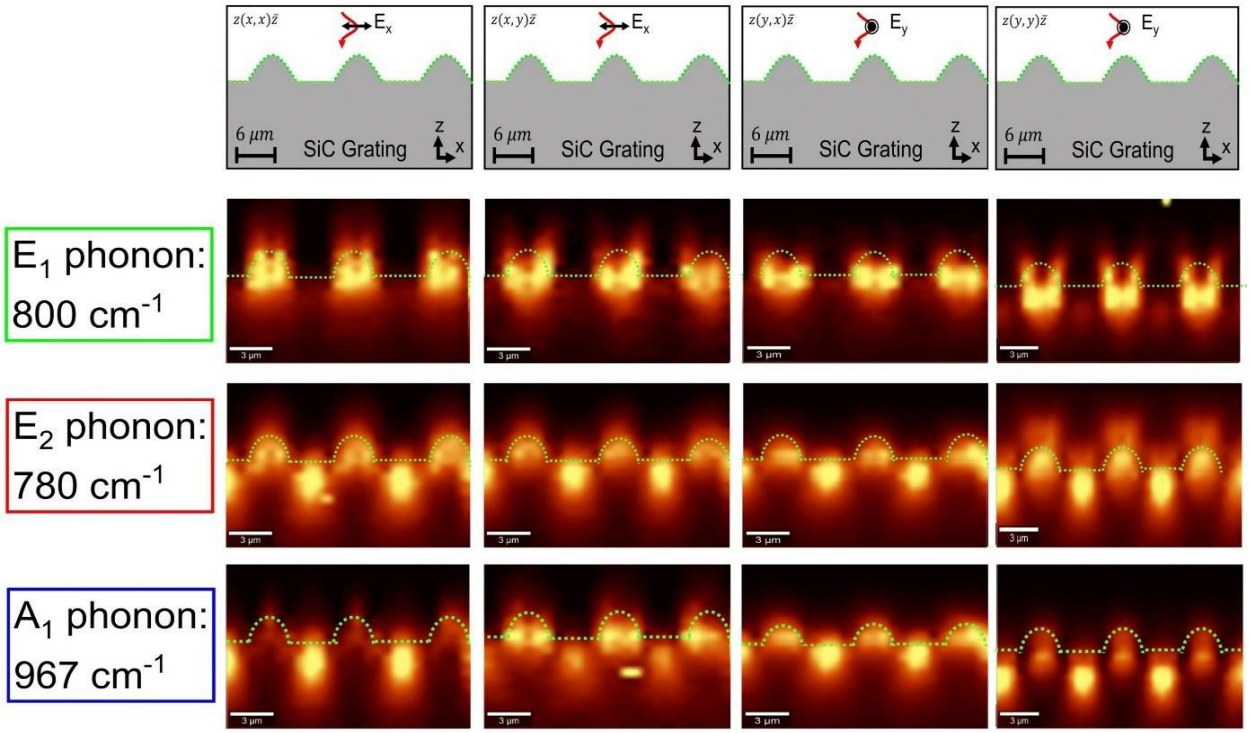


*Figure 4.13 Collected Raman maps in all polarization configurations for the optical phonon modes in the 4H-SiC grating nanostructures. The top row denotes the geometric setup for the Raman experiment, showing all four polarizer and analyzer configurations. The left column gives the three optical phonon modes. These 12 maps comprise all the polarized Raman maps obtained in the backscattering configuration.*

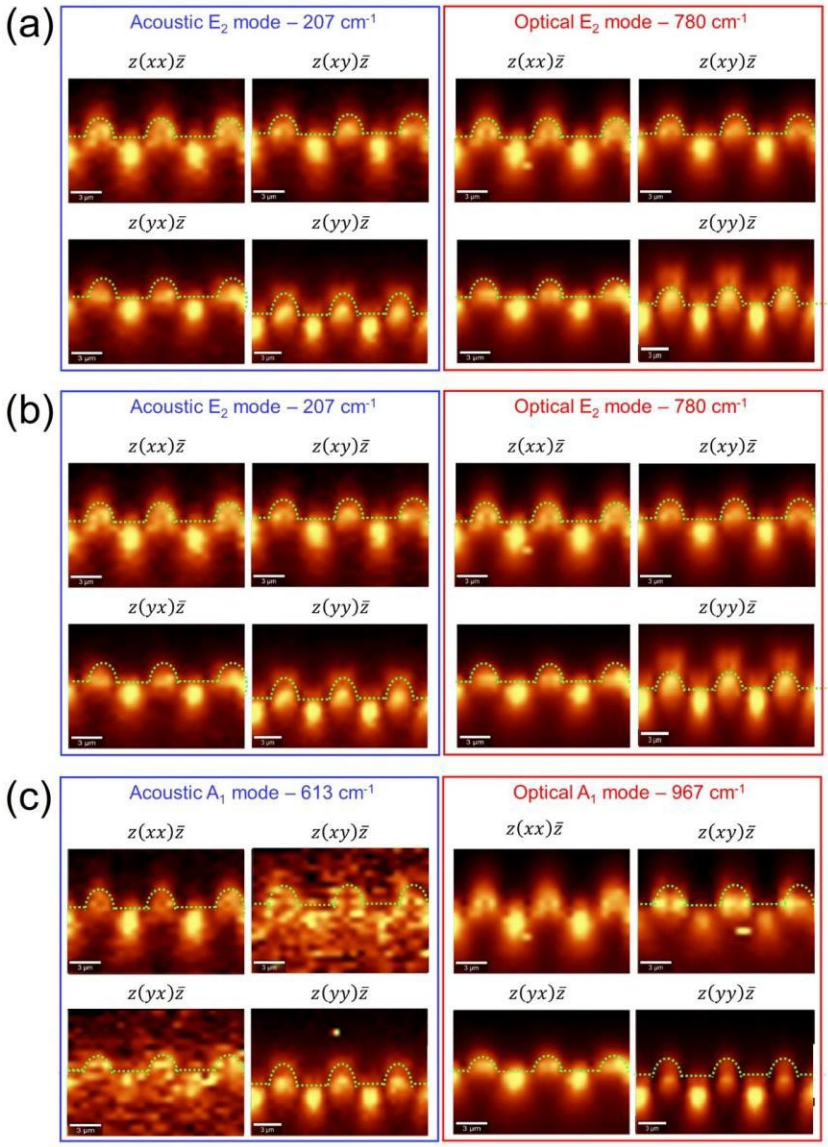


*Figure 4.14 Acoustic Phonon Raman Maps. (A). Collected Raman maps in all polarizer-analyzer configurations for both the acoustic and optical phonon mode with $E_2$ group symmetry, both sets of maps show remarkable agreement. (B). Same as (A) for the $E_2$ symmetry group phonons. (C). Same as (A) for the $A_1$ symmetry group phonons.*

In addition to the optical phonon modes in 4H-SiC and their coupling to the SPhP modes, Raman maps for the three acoustic phonon modes were also obtained, as shown in Fig. 4.2A and Fig. 4.10. Figure 4.14 displays the obtained Raman maps in all polarizer configurations, specifically to compare the optical and acoustic phonon modes for each symmetry classification. As shown in Fig. 4.2(b) and Fig. 4.9, there is one optical phonon and one acoustic phonon each for all three backscattering Raman-active phonon symmetries in 4H- SiC. Figure 4.14 shows the Raman maps for both the acoustic and optical phonon modes in the SiC grating structures for the $E_2$ group symmetry (panel a), $E_1$ group symmetry (panel b), and $A_1$ group symmetry (panel c). The Raman maps of both the acoustic and optical phonon clearly depict similar field distributions in the SiC gratings. Thus, the Raman maps shown in Fig. 4.14 demonstrate the remarkable fact that the coupling between SPhPs and bulk phonon modes applies to the acoustic phonon modes, as well. That is, even though acoustic phonons are thought to play no role in the physics of SPhPs and little role in optical systems in general, our Raman study provides evidence that their interaction with the SPhP modes mirrors that of the optical phonon modes owing to the small Raman polarizability associated with acoustic phonons. This surprising discovery indicates that there is a wider range of material interactions related to SPhp modes than previously thought, including material interactions far outside the Reststrahlen band.

# Chapter 5

## Traveling Surface Phonon Polariton Modes in One-Dimensional Gratings

## 5.1 Introduction to Surface Phonon Polaritons in SiC

As already mentioned, Surface phonon polaritons (SPhPs) are a low-loss alternative to surface plasmon polaritons with the potential for mid-infrared to terahertz nanophotonic devices. One requirement for the development of nanophotonic circuitry is the transport of information (i.e., polaritons) from one circuit component to the next. Traveling surface phonon polaritons in isotropic media presents a potential mechanism to achieve the desired interconnects. While localized surface phonon polaritons have been widely implemented, no traveling surface phonon polaritons in nanostructured isotropic ionic crystals have been demonstrated or explored up to date. In this chapter, we experimentally and theoretically demonstrate traveling surface phonon polaritons in one-dimensional grating. Furthermore, Raman mapping, when compared with phonon distribution based on selection rules, provided additional evidence for the presence of both traveling and localized modes. We provide mechanisms to control the group velocity, propagation length, and confinement of the traveling modes by engineering the geometric parameters of the gratings. Our results show that the group velocity can be tuned up to 4% speed of light in the vacuum, achieving propagation lengths higher than 150 μm and confinement below 2μm.

The field of nanophotonics, particularly the study of surface phonon polaritons (SPhPs), has captured lots of attention in research activities. SPhPs are electromagnetic waves propagating at the interface between materials with negative (metallic-like) and positive (dielectric) permittivity and have enormous potential for use in nanophotonic devices[23, 61, 89]. They offer advantages over surface plasmon polaritons (SPPs) due to their reduced loss, attributed to the higher lifetime of phonons[90, 91] compared to free carrier lifetimes[15, 17, 92]. The availability of phonon

polaritons in the mid-infrared to far-infrared frequency range [18, 21, 93] makes them a good alternative for traditional plasmonic materials in the mid-wave infrared [94, 95].

Polar dielectric materials, such as silicon carbide (SiC), exhibit interesting properties within the frequency range between the transverse optical (TO) and longitudinal optical (LO) modes. The metallic character in this frequency band leads to high reflectivity, originating from the real part of the permittivity becoming negative. This frequency range, known as the Reststrahlen band[21], allows sub-diffraction light confinement [18] and in-plane waves propagating [19] opening up new opportunities for nanophotonic applications.

Many studies have analyzed surface phonon polariton (SPhP) modes on SiC, showing the existence of localized modes on various gratings and structures [21, 96, 97]. However, the true wonder of SPhPs becomes apparent when the idea of traveling modes is explored [98, 99]. Many studies have investigated the generation of propagating squeezed light [99, 100] and have demonstrated the existence of traveling coupled plasmon-phonon polaritons on hyperbolic materials, a class of metamaterials known for their strong optical anisotropy [101, 102]. Hyperbolic metamaterials (HMMs) exhibit unique properties because their permittivity components have opposite signs, causing them to behave like a metal in one direction and a dielectric in another. This property results in light confinement in the nanoscale and supports highly directional phonon polaritons. Thus, the modes travel along specific directions inside the material, forming narrow, beam-like waves[103, 104]. Recent studies on van der Waals (vdW) materials have shown canalized phonon polariton propagation, such as constant-phase ray-like modes in single α-$MoO_3$ slabs[105] and broadband-tunable SPhPs in α-$V_2O_5$ through Na intercalation[106].

In our work, we demonstrate that it is possible to achieve similar directional surface phonon polariton (SPhP) propagation on flat nanostructured silicon carbide (SiC), which is an isotropic material and does not possess built-in anisotropy. In this study, we utilize engineered surface patterns to create the necessary conditions for polariton propagation. With this design, we

successfully guide SPhP waves on the surface by controlling the grating parameters. An advantage of this method is that SiC is CMOS-compatible, making it suitable for integration with optoelectronic devices. Furthermore, since the propagation behavior is achieved through structural design rather than the material's properties, we have greater flexibility and tunability in controlling the propagation length and confinement of the traveling mode.

While various research groups have conducted theoretical and experimental studies on propagating surface phonon polaritons [107-109], experimental evidence demonstrating traveling surface phonon polariton modes on a nanostructured isotropic ionic crystal surface has been absent until now.

This paper observes for the first time the successful excitation and propagation of traveling surface phonon polariton modes on a nanostructured surface of an isotropic ionic crystal. This achievement represents a development towards utilizing SPhPs in novel nanophotonic devices such as metatronincs [110, 111], waveguides [112] or nanoscale optoelectronic devices [113]. Additionally, the effect of different grating parameters on the propagation length and confinement factor is investigated using COMSOL Multiphysics to improve these parameters. The propagation length and confinement of the traveling SPHP mode play an important role in making these findings practical and applicable in nanophotonic applications, especially for advancing waveguides. This study aims to make significant contributions to the field of nanophotonics as the details of SPHPs and their potential applications are explored. It represents a substantial step towards harnessing the unique properties of SPHPs and creating new ways to control light on the nanoscale.

## 5.2 Optical Characterization of SPhPs

In this research, we investigate SPhP modes on a 1D grating etched into 4H SiC. This 1D grating is used to address the momentum mismatch between light photons and surface phonon modes[114]. Arrays of these gratings are made by adjusting the height and pitch, allowing for the

tuning of the SPHP eigenmodes. An AFM image of one of the gratings is displayed in Fig.1a and the cross-sectional view of the grating with its height and period profile is shown in Fig. 1b. To study the eigenmodes of SPhP in this structure, Fourier Transform Infrared (FTIR) reflection measurements were conducted with p-polarized light, incident perpendicularly on the grating at 15° and 75° angles. The results showed two pronounced dips in the reflection spectrum, confirming the successful excitation of SPhP modes.

To measure the grating parameters' impact on the phonon modes, reflection measurements were conducted for different grating configurations. The results are shown in Fig. 5.1c and Fig. 5.1d for angles of incidence of 15° and 75°, respectively, with a constant grating height and varying pitch. All grating configurations exhibited two resonance modes in the reflection spectrum. The higher-energy mode at 945 $cm^{-1}$ remained constant across different grating pitches, while the lower-energy mode at 925 $cm^{-1}$ showed a shift in resonance frequency with changing grating parameters.

To better understand the nature of the phonon modes, we performed angle-resolved reflection measurements for different grating configurations. While changing the grating pitch affects the coupling condition between light and surface modes, it is the angle of incidence that directly alters the in-plane momentum of the incoming light. By analyzing the resonance frequencies of each grating at different angles of incidence, we identified two different behaviors. The higher-energy mode at 945 $cm^{-1}$ remained fixed across all angles, indicating a localized mode confined to a specific spatial region. In contrast, the lower-energy mode at 925 $cm^{-1}$ showed a clear frequency shift with changing angle of incidence, suggesting it is a surface phonon polariton (SPhP) mode traveling along the grating surface.

Notably, the frequency shift in the propagating mode becomes more pronounced as the grating pitch ($\Lambda$) increases. According to the momentum-matching condition $k_{sphp} = k_0 n_d \sin\theta \pm m\frac{2\pi}{\Lambda}$, larger pitches provide smaller reciprocal momentum, making the coupling more sensitive to the angle of incidence. As a result, changes in angle more strongly effect the in-plane momentum, result in a greater and more observable shift in resonance frequency. This behavior aligns with the

dispersive nature of propagating SPhPs and confirms the role of grating pitch in tuning their directional characteristics.

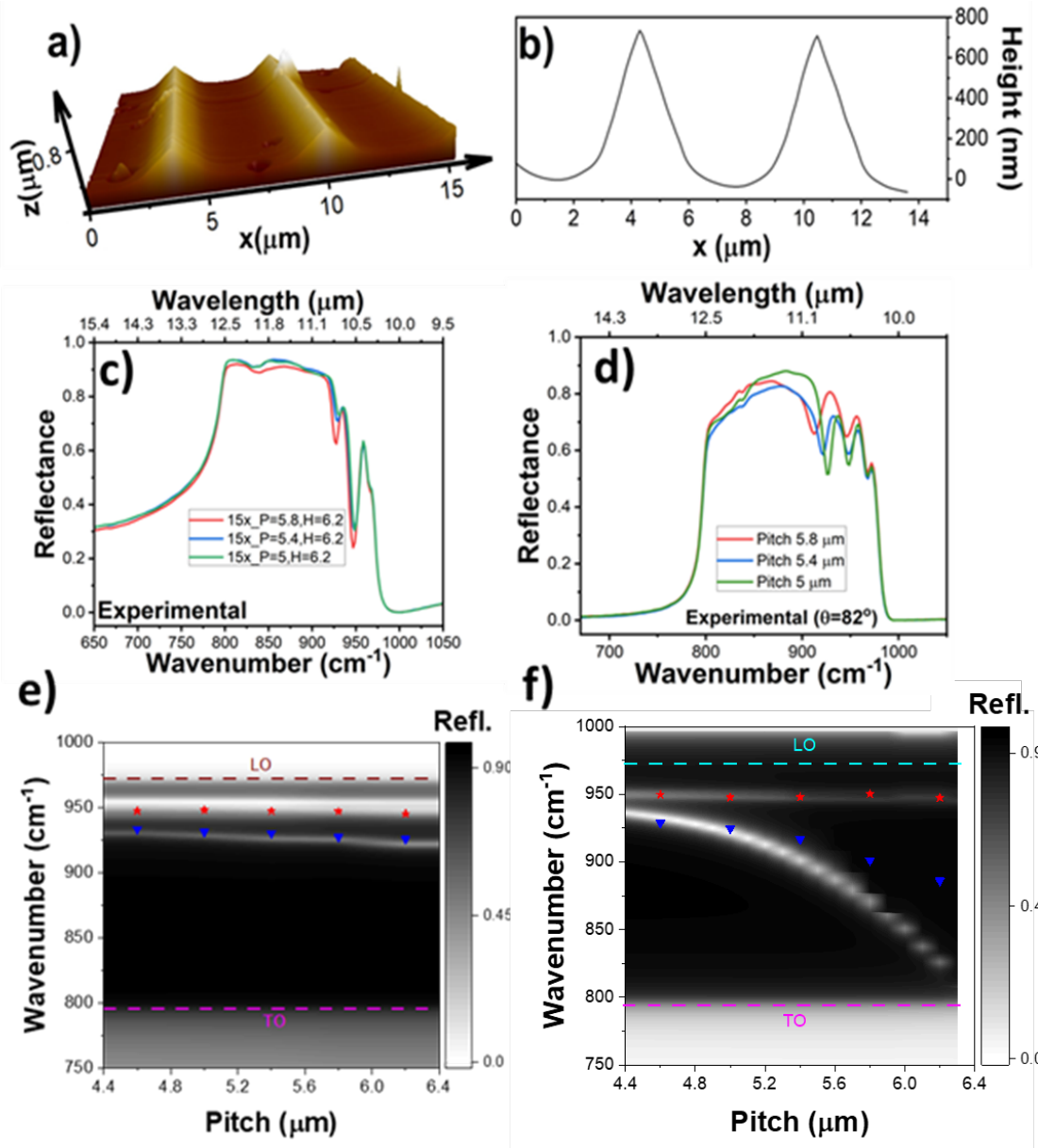

*Figure 5.1(a) AFM image of a 1D grating made of 4H SiC, displaying the surface morphology of the sample. (b) Cross-sectional view of the surface grating. (c-d) Experimental reflection spectrum with p-polarized light at (c) a 15° angle of incidence and (d) a 75° angle of incidence, for a fixed height (0.8 μm), demonstrating resonance position shifts with varying pitches for the lower energy mode.*

To validate the experimental findings of the traveling mode, a full-wave electromagnetic simulation using the finite element method was performed. The simulation kept the height constant while varying the pitch, and the light was incident at angles of 15° and 75°, as in the experimental setup. Figures 1.e and 1.f illustrate the interpolated grayscale intensity plot of the simulation's reflection spectra, with star and triangle symbols marking the experimental results for the two modes. The semiquantitative agreement between the simulated and experimental results supports the accuracy of our measurements and confirms the identification of the traveling SPhP mode. There is, however, some difference between the resonance frequencies of the simulated and experimental results. The separation between the two modes in the simulation is larger in comparison to experimental results. This could be because of the perfect surface considered in the simulation. The flat zero-slope line for the higher energy mode indicates localized behavior for this mode which means that it is confined to a specific region and does not propagate. On the other hand, the lower energy mode shows a negative slope with a positive group velocity, confirming its propagating characteristic. Further information regarding the group velocity for various grating parameters can be found in the supplementary section. The traveling mode's behavior is more noticeable when using a grazing angle objective, which further encourages the study to do experiments at even higher angles of incidence to observe the propagation of this mode even better.

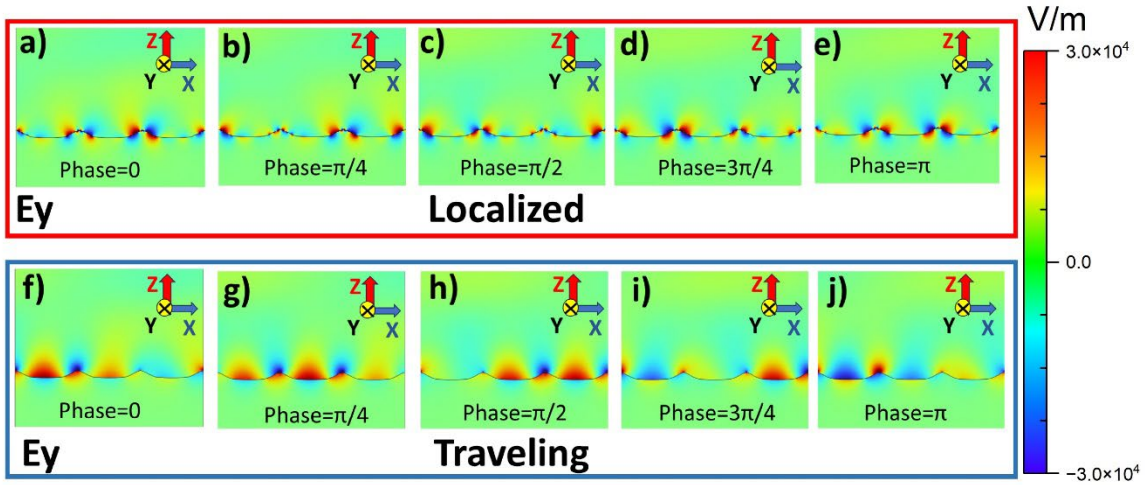


*Figure 5.2.(a) COMSOL Multiphysics simulation illustrating the propagation of the localized mode across the surface of the grating in different phases. The image demonstrates the confinement of the mode predominantly at the top of the grating.*

We used the Finite Element Method simulation to model the near-field distribution of the electromagnetic field. Here, we study the dynamic behaviors of localized and traveling modes and their temporal evolution. The results, presented in Fig. 5.2(a-j), offer a comprehensive view of the electric field in the x-direction and further support earlier observations. It is obvious from the electric field distribution that the mode with higher energy exhibits localized behavior, with a significant portion of the field confined to the tip of the triangular grating while the electric field of the lower energy mode shows traveling behavior, with the field mostly confined to the troughs of the grating, which suggests that the mode can travel across the structure. These results support the earlier finding of traveling mode and provide a solid foundation for exploring the grating's diverse behaviors under varying conditions. The agreement between the simulation results and previous observations enhances the overall reliability and consistency of this research.

## 5.3 Raman mapping of Surface Phonon-Polaritons

Since Raman spectroscopy is a non-contact and non-destructive method, it is considered a strong method for getting a better understanding of Surface Phonon-Polariton (SPHP) behavior [73]. For the Raman measurements conducted in a backscattering configuration with excitation along the c-axis, the observed phonon modes exhibit the C6v symmetry group [24]. This spectral analysis detected the LO peak at 965 $cm^{-1}$ and the TO peak at 778 and 799 $cm^{-1}$.

As demonstrated in the work by Kiernan et al.[115], the spatial distribution of phonon polaritons can be depicted using Raman depth scans. For this purpose, a Raman depth scan was performed on the x-z cross-section of the sample, and the results are shown in Fig. 5.3 for three different phonon symmetries.

The interaction between bulk phonon modes and phonon polariton modes is through polarization phenomena [115]. In this study, a full 3D map of the SPhP electromagnetic field is obtained using FEM simulation, applying the polarizability selection rule to three phonon symmetry modes. To obtain this, the E1, E2, and A1 phonon modes are utilized to investigate the spatial distribution of Raman intensity in a 1D grating, and the polarizability selection rule described in Equation (1) is applied to all Sphp eigenmodes [24].

$$\chi_{A1} = \begin{bmatrix} a & 0 & 0 \\ 0 & a & 0 \\ 0 & 0 & b \end{bmatrix}, \quad \chi_{E1,x} = \begin{bmatrix} 0 & 0 & c \\ 0 & 0 & 0 \\ c & 0 & 0 \end{bmatrix}, \quad \chi_{E1,y} = \begin{bmatrix} 0 & 0 & 0 \\ 0 & 0 & d \\ 0 & d & 0 \end{bmatrix},$$

$$\chi_{E2,1} = \begin{bmatrix} e & 0 & 0 \\ 0 & e & 0 \\ 0 & 0 & 0 \end{bmatrix}, \quad \chi_{E2,2} = \begin{bmatrix} 0 & f & 0 \\ f & 0 & 0 \\ 0 & 0 & 0 \end{bmatrix} \qquad \text{Eq.1}$$

Figure 5.3 compares the simulation and experimental results of the spatial distribution of phonon modes for three different phonon symmetries. As presented in this figure, Raman intensity findings suggest that the Raman signals are a mixture of the polarizabilities of both the traveling and localized modes. The agreement between the polarization behavior of the SPHP mode and the

results of Raman mapping confirms our experimental results on the existence of traveling and localized modes in this 1-D grating structure.

One of the main challenges in designing nanophotonic circuits is identifying equivalent lumped circuit components that function effectively at optical frequencies[116]. Converting these components into optical equivalents is important because of the difficulties in producing subwavelength components and the behavior of light-matter interactions at these frequencies. By analyzing the near-field electric field distribution and Raman mapping of the traveling mode, we find that the electric field concentrates at the trough of the grating and jumps across the triangular-shaped structure, similar to how capacitance builds an electric field between plates.

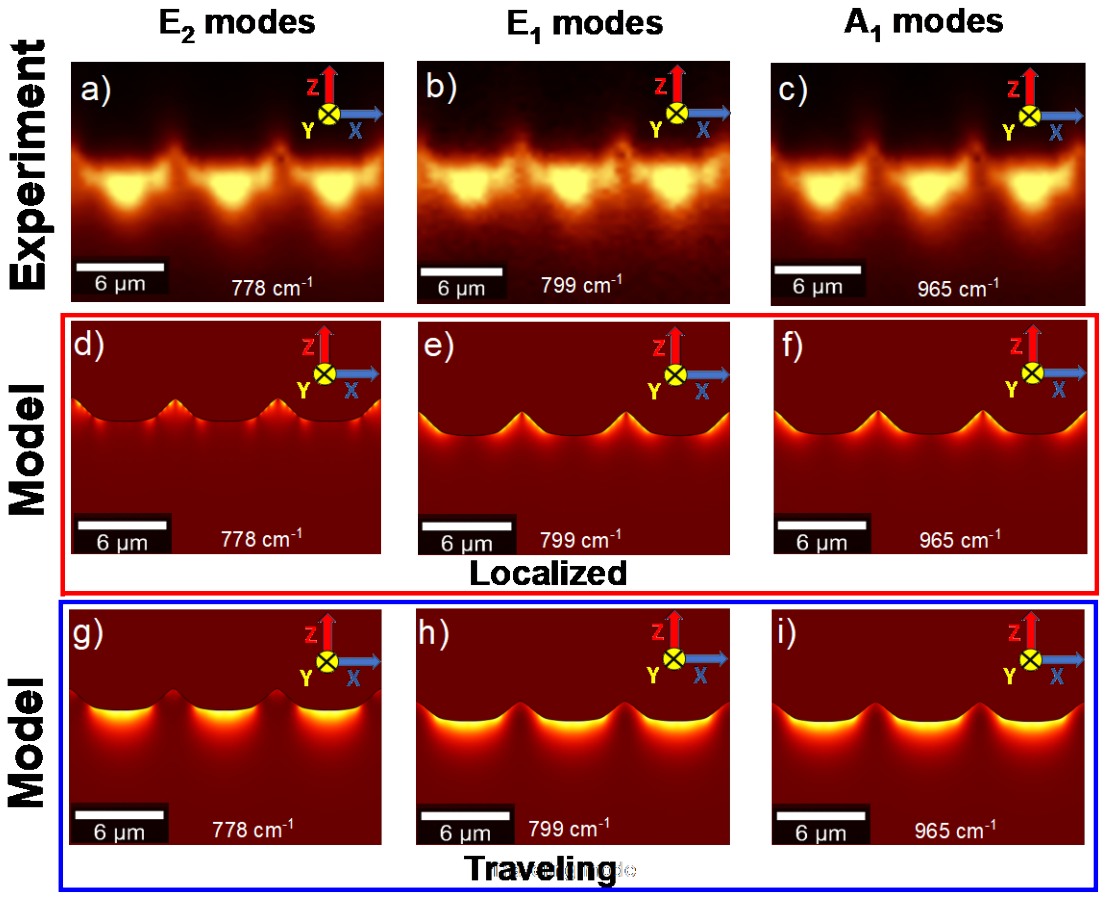

*Figure 5.3 (a-c) Experimental Raman intensity map of three optical phonon modes (E2(TO), E1(TO), A1(LO)) in 4H-SiC 1D grating. (d-f) Theoretical Raman intensity maps of the same phonon modes for localized mode and (g-i) for traveling mode.*

Based on this finding, we conclude that this grating acts as a capacitor in the mid-to-far-IR range and could serve as a capacitive component in nanophotonic circuits. As shown in the supplementary material, by changing grating parameters and dispersion relation, one can modify the reactance and, therefore, the group velocity of light traveling through the grating. This allows us to create slow light for nanophotonics.

## 5.4 Analysis of Surface Phonon Polariton Propagation and Confinement in 1D SiC Grating

Following the discovery of a novel traveling mode in a 1D grating, the propagation length and confinement factor are key parameters of interest. This parameter is critical in realizing the full potential of this structure for diverse applications, including waveguides, nanophotonic devices, and sensors.

In this section, we want to find out how changing grating parameters like grating pitch, height, and width influence the propagation length and confinement, and whether it is possible to control these two factors by grating parameters.

For this purpose, first, we dig into the propagation length, which is computed for a bulk Silicon Carbide (SiC) substrate at the resonance frequency. The plane wave that falls on the substrate decays exponentially in a direction perpendicular to the surface, and the propagation length in the x direction can be obtained by using Equation 2.b[29]

$$k_{sp} = k_0\sqrt{\frac{\varepsilon_1\varepsilon_2}{\varepsilon_1+\varepsilon_2}} \qquad \text{Equation 2.a}$$

$$L_P = \frac{1}{2*Im[k_{sP}]} \qquad \text{Equation 2.b}$$

Here, ksp denotes the propagation constant of the wave at the interface between two materials with permittivities ε1 and ε2, where ε1 refers to air (≈1) and ε2 corresponds to SiC permittivity. Eq. 2b shows that the propagation length Lp is inversely proportional to the imaginary part of ksp. Therefore, an increase in Im(ksp), which means higher loss, results in shorter propagation distances.

Figure 5.4a. shows the propagation length as a function of wavelength, obtained from MATLAB simulation. This plot has a minimum at the wavelength where the real part of the permittivity (Re(ε)) crosses -1. This is the condition for SPhP resonance, and at this point, the light is strongly coupled with the optical phonons at the interface. As a result, the electromagnetic field becomes more confined, leading to a shorter propagation length.

The plot shows that by pushing the resonance frequency toward longer wavelengths, the propagation length increases exponentially. This behavior is important for nanophotonic and mid-IR device applications, where minimizing energy loss and maximizing propagation length are important. The ability to support extremely long SPhP propagation lengths at longer wavelengths offers exciting possibilities for designing low-loss, compact photonic circuits.

By exciting the 1D grating with a dipole as a source point using COMSOL Multiphysics, we can see how long the wave propagates within the structure by looking at the near field electric field. Fig. 4.a shows how grating parameter adjustments can affect the propagation length, providing information about which grating parameters will work best for our particular application requirements. For example, Fig. 4.c compares the propagation lengths for three different pitches: starting from 6 up to 7.5 μm, it is possible to tune the propagation length from 30 to 140 μm. Previous studies on surface plasmon-polariton (SPP) modes have reported propagation lengths of around 20 μm [117] which are mainly limited by metal ohmic losses. Whereas, for SPhPs, propagation lengths larger than 140 μm were achieved in this paper. This improvement is largely due to the absence of ohmic losses in dielectric materials, as phonon damping—the main loss mechanism in SPhPs—is significantly lower than the electron-based losses in SPPs. However, the

long propagation lengths observed here are not only due to low material losses. The specific design of the grating structure, along with careful tuning of its geometrical parameters, also plays an important role in enhancing the SPhP propagation by optimizing the coupling and confinement conditions.

The confinement of the SPHP mode to the surface is another crucial parameter to be considered. This factor indicates how far the electric field extends in the air in a direction perpendicular to the surface and weak confinement of this traveling mode may result in crosstalk in waveguides or optoelectronic integrated circuits. This factor can be calculated with Equation 3.b, where $k_z$ in Eq.3.a is the wave vector in the z-direction [114].

$$k_z = k_0\sqrt{\frac{\varepsilon_1^2}{\varepsilon_1+\varepsilon_2}} \qquad \text{Equation 3.a}$$

$$\delta_z = \frac{1}{\mathrm{Im}[k_z]} \qquad \text{Equation 3.b}$$

The confinement factor for a flat 4H SiC substrate is plotted in Fig 5.4.b with a black dotted line, and it shows that pushing the SPHP mode to higher frequencies results in weaker confinement. Fig 5.4.b also illustrates the effect of adjusting the grating parameters on the confinement factor which follows the same trends as those observed for a flat surface. However, the nanostructure shows slightly weaker confinement compared to the flat substrate. The confinement and propagation length for different grating parameters are obtained by looking at the near-field distribution in the simulated results, as shown in Fig 4.c.

Similar to the propagation length, the plot shows a dip in the confinement factor at the same wavelength where the propagation length reaches its minimum. As previously explained, this is because of strong coupling at the resonance frequency, where the mode becomes highly confined. Moving away from this point, result in weaker confinement and a corresponding increase in propagation length.

This analysis reveals a trade-off between the propagation length and the confinement of polariton modes: increasing propagation length results in weaker confinement, and vice versa. This offers a way to optimize the grating design based on the application to achieve stronger confinement or longer propagation length.

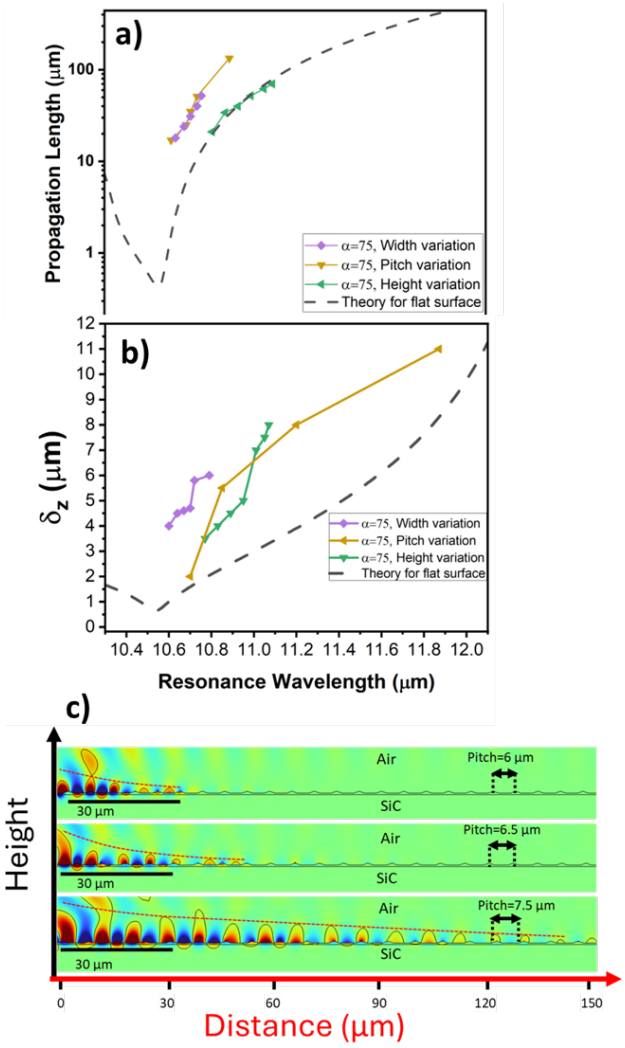


*Figure 5.4 (a) Propagation length for a flat surface is plotted with a black dotted line, along with the effect of varying grating parameters on the propagation length for a 1D grating structure. (b) Similar to (a) but showing the confinement factor. (c) Near-field distribution for three different*

*pitches, illustrating how increasing the pitch affects the propagation length and confinement factor.*

## 5.5 Conclusion

In this work, we report on the investigation of SPhP modes in a 1D grating structure fabricated from 4H-SiC. For the first time, we demonstrated the traveling surface phonon polariton in such a nanostructure. This discovery holds noticeable promise for nanophotonic applications, especially in data transmission, and offers potential for the miniaturization of photonic circuits. Further support is provided for the experimental results by finite element method simulations, where propagations of the traveling mode can be clearly observed in the near-field electric field distribution.

Additionally, Raman measurements, combined with phonon distribution analysis based on selection rules, provided further confirmation of the existence of both traveling and localized modes, showing distinct phonon distributions for each.

Finally, the adjustment of grating parameters allows us to tune the propagation length and confinement of the modes; above 150 μm propagation length is easily achievable, which is a breakthrough in the field of nanophotonics.

## 5.6 Supplementary

In conclusion, this chapter presents the key results of the study. To provide additional context and supporting information, the supplementary section includes all relevant material from the associated publication.

### 5.6.1 Sample preparation

The 1D SiC grating sample was prepared in 200×200 μm arrays with a pitch and height variation from 1 to 6 μm in steps of 0.4 μm. These gratings were fabricated on undoped 4H-SiC substrates

that had been pretreated and activated with $O_2$ plasma preen treatment. The 1D grating pattern was made using a maskless direct laser writing (DLW) approach with the Photonic Professional GT2 Nanoscribe 3D printer [84]. For this process, the polymer IP-Dip2 was used, with a laser power of 20 mW and scanning speed of 10,000 μm/s. After forming the gray mask on the substrate, the grating was etched into the substrate using reactive ion etching (RIE). $SF_6/O_2$ gas was used for the RIE process, where $SF_6$ etched the SiC and $O_2$ removed the polymer. We used the etching recipe mentioned in the paper by Sharac. et al [118] for etching the 4H-SiC.

### 5.6.2 Surface topography measurements:

To analyze the surface topography of the 1D grating, we used Atomic Force Microscopy (AFM). Measurements were performed with an NX10 AFM using a silicon tip (radius < 10 nm) in non-contact mode with a force constant of 88.076 N/m and resonant frequency of 330 KHz. Scans covered a 15 × 15 μm area, capturing detailed surface information across at least two grating pitches. All images were processed with the XEI (Park Systems) software from which the cross-section profiles have been extracted to measure the pitch and height parameters from Fig 1b. These parameters were then used in COMSOL simulations to model the grating surface as accurately as possible. Surface parameters such as pitch and height were confirmed across multiple scan areas to ensure data reliability.

### 5.6.3 Raman measurements:

Raman spectra were collected using a WITec Alpha 300R confocal Raman microscope equipped with a UHTS 600 spectrometer and the results are shown in Fig 3 and Fig S.2. Measurements were done in a backscattering configuration with incident and backscattered light aligned along the c-axis. Excitation was done with a green laser ($\lambda$ = 532 nm), focused on the sample through a Zeiss EC Epiplan Neofluar 100x objective lens (NA = 0.9), producing a spot size of approximately 0.7 μm. The laser power was set to 30 mW on the sample, and with an integration time of 10 seconds, we can achieve a good signal-to-noise ratio. To capture the spectrum over the range 0–1000 $cm^{-1}$, a G2 grating (1800 grooves/mm) with a spectral center at 520 $cm^{-1}$ was used. The backscattered light was collected through the same objective and detected by an EMCCD detector. The Raman

spectra in Fig. S2a show the Raman-active phonons for 4H-SiC, with TO modes at 778 $cm^{-1}$ and 799 $cm^{-1}$, and an LO mode at 965 $cm^{-1}$.

To obtain a Raman image from the cross-section of the grating, as shown in Fig. 3 and Fig. S2, a Raman depth scan was performed by moving the focal point deep into the grating structure. The laser was initially focused 2 μm above the surface, and then the z-stage was incrementally moved into the structure in 0.4 μm steps. The covered scan ranges were 20 μm in the x-direction and 12 μm in the z-direction, at 50 points/line and 30 lines/image. This gave a spatial resolution of 0.4 μm in x and z direction. The sample, along the x-y plane, was controlled by a piezoelectric stage, whereas the objective was varied for motion along the z-axis. At every spot, one Raman spectrum was recorded, and the Raman intensity counts for each of the bulk phonon modes were plotted across the grating. This visualizes phonon modes' spatial distribution, generating a cross-sectional Raman image. Data acquisition and processing was done using WITec Project Five software.

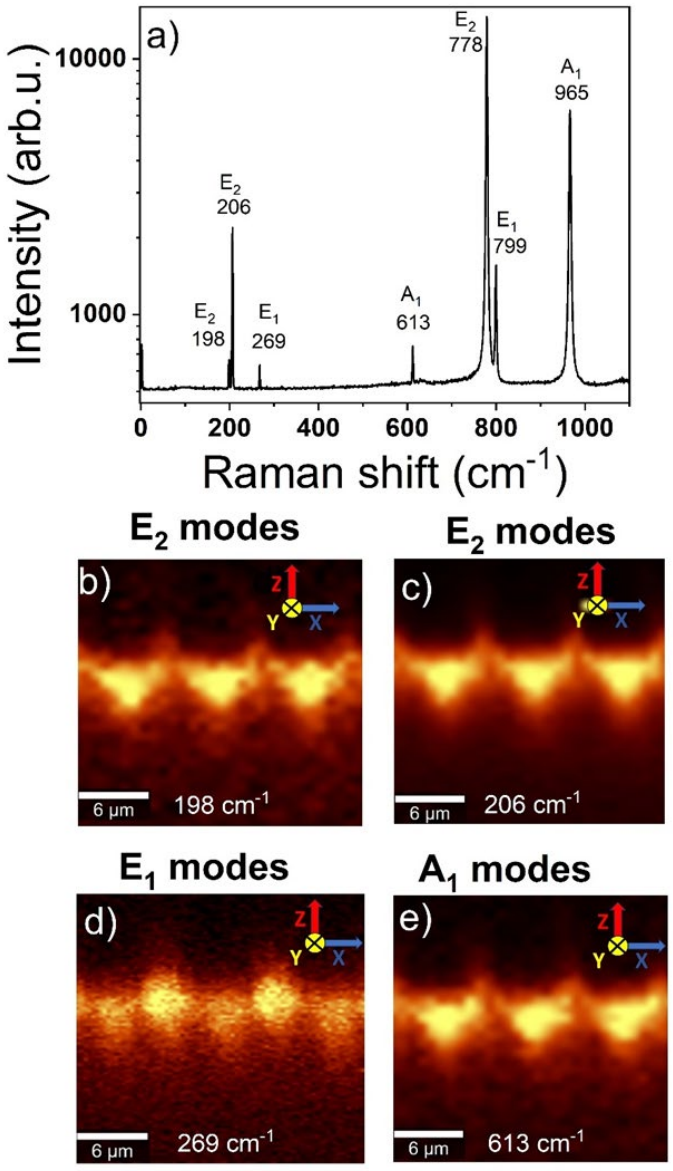


*Figure 5.5 a) Backscattering Raman spectra of 4H-SiC. b-e) Experimental Raman intensity map of additional optical phonon modes (198 $cm^{-1}$, 206 $cm^{-1}$, 269 cm $cm^{-1}$, 613 $cm^{-1}$,) in the 4H-SiC 1D grating, not presented in the main text.*

### 5.6.4 Reflection spectroscopy

The reflection measurements were made by using an FTIR Bruker Tensor 27 with coupled Hyperion IR microscope. The setup included a KBr beamsplitter, covering the spectral range of 7500-370 $cm^{-1}$.

A mercury cadmium telluride (MCT) detector, cooled with liquid nitrogen, was used. IR measurements were made at ambient temperature by using an integration time of 60 seconds, collecting spectra with 100 averaged scans at a resolution of 3 $cm^{-1}$ from a 200 $\mu m^2$ sampling area. A reverse-Cassegrain objective focuses the p- and s-polarized IR light onto the sample at incidence angles between 12° and 23.6°. This objective also collects the reflected light and directs it onto the HgCdTe detector. The polarization of the mid-IR light was employed to achieve s and p-polarized reflections, while Gaussian fitting was used in determining the correct position of the peaks.

The reflection spectrum for two different polarizations is shown in Fig. S1. As shown in this figure, s-polarized light is parallel to grating. Due to a momentum mismatch between incident light and surface phonon modes, no SPHP modes are excited. The excitations of SPHP modes are indicated by dips in the Reststrahlen band. We confirm that no SPHP mode was excited, because there is no dip of s-polarized light in this band. On the other hand, for p-polarized light, whose polarization is perpendicular to the grating, several dips appear in the Reststrahlen band, indicating the excitation of SPHP modes.

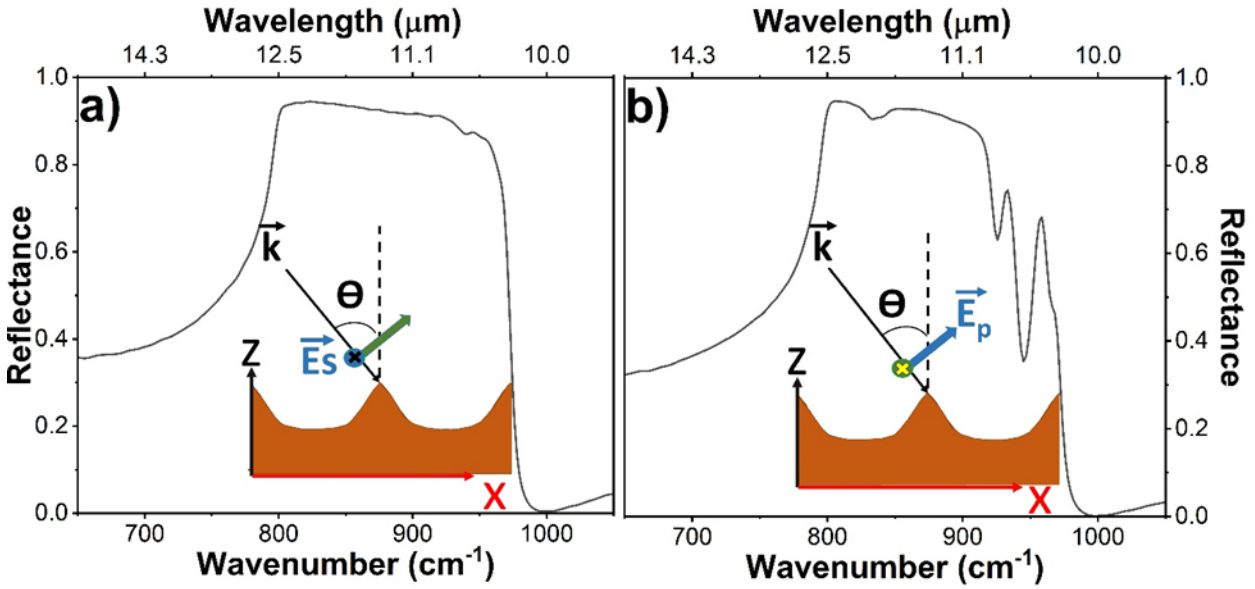


*Figure 5.6 The excitation of the sample with s-polarized light, aligned parallel to the grating, showing only the Reststrahlen band. b) The excitation of the sample with p-polarized light, perpendicular to the grating, displaying the excitation of two Surface Phonon Polariton (SPhP) modes.*

### 5.6.5 Electromagnetic field simulation

The far-field reflection and near-field electromagnetic field simulations were performed using the finite element method (FEM) within COMSOL Multiphysics® software. The RF module is used for these simulations and the grating surface was illuminated by p-polarized and s-polarized plane wave excitations applied from the top edge of the simulation environment at 15 and 75-degree angles of incidence, corresponding to the average angles used in the experimental setup. For the propagation length simulation, instead of using port excitation, we applied a dipole moment to simulate laser excitation of the sample. We then measured the distance at which the electric field decays to 1/e of its initial amplitude.

The dimensions collected from AFM imaging were used for grating geometry and the optical constants of 4H-SiC were determined through ellipsometry. To accurately simulate the experimental setup, which includes multiple periods of the grating, we modeled just one period of the SiC grating, using periodic boundary conditions to create the effect of an infinitely long grating. Air was set as the surrounding medium to approximate real-world conditions.

### 5.6.6 Supplementary experimental data

As described in the main section, these 1D gratings can behave like capacitors in the mid-to-far infrared range, therefore we can create slow light in optoelectronic devices [119]. This slowing of light occurs because of a significant reduction in group velocity, coming from the extreme dispersion within the grating structure. Such slow light is important for enhancing light-matter interactions and can support time-domain processing of optical signals [120]. In this section, I present the dispersion relation of the traveling mode for three different grating structures, with constant height and pitch while varying the grating base width. Fig. S3 shows that reducing the grating base width and bringing the capacitor plates closer result in even slower light propagation. This shows that grating's geometry can directly affect the dispersion relation and its ability to slow light. This slowed group velocity is important for applications where enhanced light-matter interactions are desired, such as in optical sensing, signal processing, or certain nonlinear optics. By controlling the geometry of the grating, we can tune the dispersion and therefore the effective propagation speed of the traveling modes within the structure, tailoring the photonic response for specific optoelectronic applications.

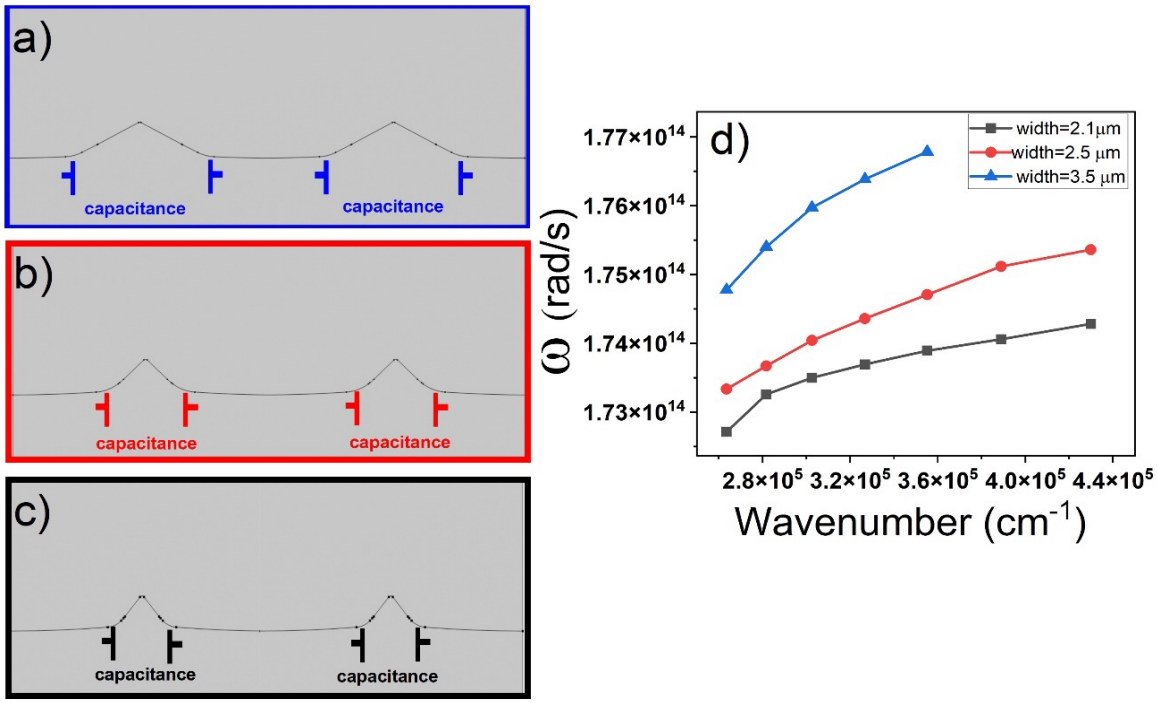


*Figure 5.7 a-c) Illustration of the 1D grating structure acting as a capacitor, with constant height and pitch while varying the base width. The effect of grating geometry on the dispersion relation of traveling modes is depicted in part (d). Reducing the grating base width effectively brings the "capacitor plates" closer together, resulting in a significant reduction in the group velocity of light.*

# Chapter 6

## Anomalous Electron-Phonon coupling of the Transverse optical phonon mode with $E_2$

The interaction between electrons and phonons plays an important role in determining the optical, electrical, and thermal properties of semiconductors [121, 122]. In polar semiconductors such as 4H–SiC, the long-range interaction between free charge carriers and optical phonons is important for high-power and high-frequency electronic applications. Typically, this interaction is investigated through the phenomenon of longitudinal optical phonon (LO) coupling with the carrier plasma, a phenomenon that is well known and has been extensively studied[123]. In contrast, transverse optical phonon (TO) modes are usually not considered to be affected by free carriers, since they lack the long-range Frolich interaction [124, 125].

In this chapter, experimental results are presented that show that this assumption is not always true for the 4H–SiC structure. Raman spectroscopy performed on doped 4H–SiC epitaxial layers shows that the frequency of the $E_1$(TO) phonon mode shifts in a regular manner with increasing doping concentration. This finding could be an indication of the existence of some kind of interaction between free carriers and transverse optical phonons, a phenomenon that has not been reported for this material so far.

## 6.1 Theoretical Background on Phonon–Plasmon Interactions and TO Phonon Assumptions

In polar semiconductors, the interaction of phonons with free carriers can affect the optical and electronic properties of the material [121]. These interactions are described by electron–phonon coupling (EPC), which includes short-range interactions like deformation potentials, and long-range electrostatic interactions through polarization fields caused by lattice vibrations [126]. One of the well-known electron-phonon coupling modes in polar materials is the coupling of

longitudinal optical phonons (LO) with plasmons [127]. In doped semiconductors, the free charge carriers such as electrons collectively oscillate with the electric field generated by the LO phonons. This coupling produces new hybrid modes called LO phonon-plasmon coupled (LOPC) modes [128]. The frequency of such modes depends on the specific carrier concentration, effective mass, and dielectric properties of the material and appears in the form of characteristic peaks in Raman or infrared spectra [129]. This interaction, described by the Frohlich theory [130, 131], arises from the coupling of the longitudinal optical phonons (LO) with the electric field caused by charge fluctuations in a material. In the long-wavelength limit, the phonons can produce a macroscopic electric field that will couple to free electrons or holes in the material. However, transverse optical phonons (TO) do not create such a field, and therefore, they should not be affected by the charge carrier concentration and do not participate in electron coupling.

In Raman spectroscopy, this interaction leads to a distinct splitting of the LO mode with increasing carrier concentration, such that the mode splits into two branches: an upper branch $\omega_+$ that has properties similar to the LO mode, and a lower branch $\omega_-$ that is more plasmon-like [132]. These properties provide a powerful tool for determining the carrier density in doped samples [83]. However, TO phonons have generally been considered unaffected by doping in bulk materials. Since TO modes involve atomic displacements perpendicular to the propagation direction and do not induce macroscopic polarization, conventional wisdom suggests that they do not couple to free charge carriers in the long-wavelength regime. This assumption has shaped both theoretical models and the interpretation of Raman spectra for decades.

Nevertheless, recent theoretical studies challenge this perspective. While the macroscopic electric field component of TO modes vanishes, short-range interactions such as deformation potential coupling, local dielectric screening, or lattice disorder may still influence TO mode behavior. Furthermore, anisotropic crystal structures like 4H–SiC, which exhibit directional dependence in their dielectric response, may have weak but non-negligible coupling between TO phonons and carriers under certain conditions [133].

Building on this framework, in doped samples of 4H–SiC and 6H–SiC, the phonon-plasmon coupling affects the $A_1$(LO) phonon mode. As the doping level increases, this interaction causes a shift in the frequency of the $A_1$(LO) mode and also a broadening (increasing the linewidth) of this peak in the Raman spectrum.

To understand these phenomena, one must examine the dielectric response of the material. The frequency-dependent dielectric function ε(ω) in a polar semiconductor containing free carriers is modeled as [124]:

$$\varepsilon(\omega) = \varepsilon_\infty \left(1 + \frac{\omega_{Lo-}^2\, \omega_{To}^2}{\omega_{To}^2 - \omega^2 - i\omega\Gamma} - \frac{\omega_p^2}{\omega^2 + i\omega\gamma}\right)$$

In this equation, $\varepsilon_\infty$ is the high-frequency dielectric constant; $\omega_{Lo}$ and $\omega_{To}$ are the longitudinal and transverse optical phonon frequencies, respectively. $\omega_p = \sqrt{\frac{ne^2}{\varepsilon_0 m^*}}$ is the plasma frequency, where n is the carrier concentration and $m^*$ is the effective mass. $\Gamma$ represents the phonon damping rate, and $\gamma$ is the plasmon damping rate.

When the dielectric function value becomes zero, phonon-plasmon coupled modes are created:

$$Re[\varepsilon(\omega)] = 0$$

At these frequencies, LO phonon modes interact with free carriers, resulting in the formation of two combined modes: a higher-frequency mode that behaves like an LO phonon ($\omega_+$ branch), and a lower-frequency mode that exhibits plasmonic properties ($\omega_-$ branch) [134]. An increase in doping level results in a higher plasma frequency ($\omega_p$). As a result, the upper branch shifts to higher frequencies, and the lower branch shifts to lower frequencies. This interaction appears as a blue shift of the $A_1$(LO) mode in Raman spectra. In theory, both $\omega_+$ and $\omega_-$ branches are expected to be seen, but practically, the lower branch ($\omega_-$) is damped due to its plasmonic nature and is rarely seen in the Raman spectrum. Therefore, the highest spectral intensity corresponds to the upper branch ($\omega_+$), which is seen as the main peak in the spectrum.

At the same time, the stronger electron-phonon interaction leads to an increase in phonon damping, through a process called Landau damping, where phonons decay to electron–hole excitations. This increases the imaginary part of the dielectric function ε(ω) and consequently the width of the Raman peaks [133]. In other words, the stronger electron–phonon coupling reduces the phonon lifetime and increases its linewidth. This can be described and modeled using the equation of coupled phonon-plasmon modes.

$$\omega_{\pm}^2 = \frac{1}{2}(\omega_{Lo}^2 + \omega_P^2) \pm \frac{1}{2}\sqrt{\left(\omega_{Lo}^2 + \omega_p^2\right)^2 - 4\omega_{LO}^2\omega_{TO}^2}$$

As doping increases, the plasma frequency ($\omega_p$) increases, causing the higher branch ($\omega_+$) to shift to higher frequencies and the lower branch ($\omega_-$) to appear at lower frequencies.

This coupling mechanism has been studied in materials such as GaAs [134], ZnO [129], and SiC. Burton et al. [124] studied electron–phonon coupling in SiC and showed that increasing the doping results in a blue shift and broadening of the $A_1$(LO) mode. This behavior has been used as a non-destructive method for measuring charge carrier concentration [83]. Unlike longitudinal (LO) modes, transverse (TO) modes are not coupled strongly to free charge carriers, because these modes do not produce a macroscopic electric field at long wavelengths. In the Fröhlich model, it is assumed that lattice vibrations produce a macroscopic polarization field. However, in TO modes, such a field is not produced due to the direction of atomic displacement. For this reason, models such as the Fröhlich model and the dielectric medium approximation predict that the coupling between TO modes and charge carriers is very weak and even negligible. Experiments have also confirmed this. For example, Chakraborty et al.[125] observed in monolayer $MoS_2$ that with increasing electron doping, the $A_{1g}$ mode (which behaves like the $A_1$(LO) mode) shifts and broadens towards lower frequencies, while the $E_{2g}$ mode (analogous to the $E_1$(TO) mode in SiC in terms of symmetry and polarization) remains almost unchanged. This behavior indicates that the TO modes are practically unaffected by doping. For this reason, TO modes are usually considered

to be less sensitive probes of doping and are used more than LO modes in Raman or infrared spectroscopy to investigate the effect of doping and obtain the relevant parameters.

However, as we show in the following sections, our experimental results on doped 4H–SiC epitaxial films indicate that the resonance frequency of the $E_1$(TO) phonon mode shifts with increasing doping and only under certain polarization configurations, a behavior that has previously been reported only for the $A_1$(LO) mode. This shift indicates that there is electron–phonon interaction for the $E_1$(TO) mode, which contradicts the common belief that TO modes are insensitive to free charge carriers. Although the exact origin of this coupling is still not fully understood, the lack of a shift observed in the $E_2$(TO) mode means that such an effect cannot arise due to lattice strain or crystalline defects in the form of atomic vacancies or impurities. This observation, contrary to previous reports, is consistent with recent theoretical predictions by Macheda et al.[133], where it was suggested that TO modes can also couple to charge carriers via short-range mechanisms, outside the classical Froehlich model.

## 6.2 Experimental Evidence of $E_1$(TO) Mode Coupling

We investigated a series of five n-type doped 4H–SiC epilayer samples grown on undoped 4H–SiC substrates. Each sample consists of a high-purity, undoped substrate layer, upon which an epilayer with a specific doping level was grown. The doping concentrations of the epilayers vary across the samples and are summarized in Table 6.1.

| Name | Name used in paper | Nd ($cm^{-3}$) |
|---|---|---|
| C2130617 | A | $1 \times 10^{14}$ |
| C2121217 | B | $5 \times 10^{17}$ |
| C2130612 | C | $5 - 6 \times 10^{17}$ |
| C2130611 | D | $1\times 10^{18}$ |
| C2130620 | E | $5 \times 10^{18}$ |

*Table 6.1doping concentrations for the investigated 4H–SiC epilayer samples.*

In this work, we studied the effect of doping on different phonon modes by performing Raman measurements on samples with different doping in two polarization geometries: parallel ($z(xx)\bar{z}$) and perpendicular ($z(xy)\bar{z}$) polarizations.

In the parallel polarization setup ($z(xx)\bar{z}$ or $z(yy)\bar{z}$), the scattered light is polarized parallel to the incident light, along the same in-plane direction (either x or y). In contrast, in the perpendicular polarization configuration ($z(xy)\bar{z}$), the polarization of the scattered light is perpendicular to the incident light. In order to change the polarization of the incident light, a half-wave plate was placed along the path of the incident laser beam, as depicted in Figure 6.1. The half-wave plate rotates the polarization direction of the incident light, and we are able to tune the polarization state of the incident beam to the desired direction.

The polarization of the scattered light at the detection end was controlled by an analyzer (a linear polarizer), which was placed in the path of the scattered light just before the entrance slit of the spectrometer. The analyzer selects the polarization component of the scattered light that arrives at the detector. By appropriately aligning the half-wave plate and analyzer, we can reach the desired parallel ($z(xx)\bar{z}$) or perpendicular ($z(xy)\bar{z}$) polarization configurations.

Using this optical setup, we can excite Raman modes under different polarization configurations and analyze how each mode behaves at different doping concentrations.

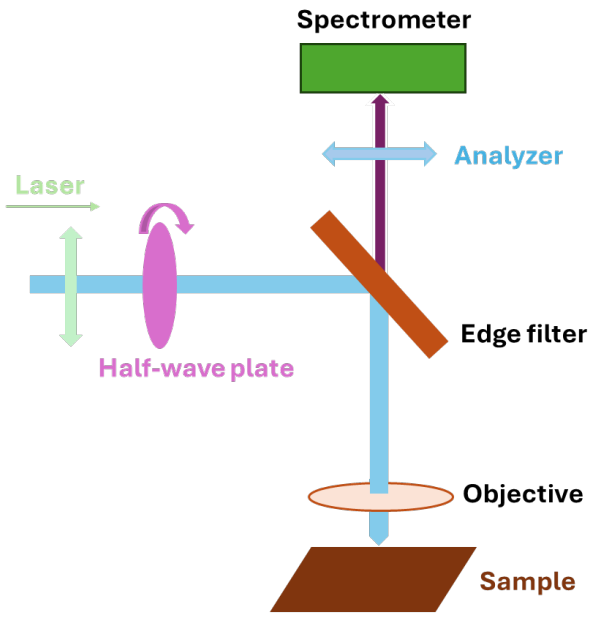


*Figure 6.1 Raman setup for polarization control using a half-wave plate and analyzer to achieve parallel and perpendicular polarization.*

Figure 6.2 shows the Raman spectrum of Sample A measured under both parallel and perpendicular polarization configurations. The results show a clear polarization dependence for several phonon modes, although in some cases deviations from ideal theoretical predictions are observed. The $A_1$(TO) mode at around 613 $cm^{-1}$ appears prominently in the parallel polarization configuration and is strongly suppressed in the perpendicular polarization state, a behavior consistent with Raman selection rules. The $E_1$(TO) mode at around 799 $cm^{-1}$, which is theoretically forbidden in the parallel configuration, is observed in our measurements stronger in the parallel than in the perpendicular mode. The $A_1$(LO) mode at around 966 $cm^{-1}$ is also seen in both configurations, but its intensity is higher in the parallel polarization state.

These trends are generally consistent with the Raman selection rules derived from the symmetry of the 4H–SiC crystal and its Raman tensors. In particular, the $A_1$ modes have a diagonal Raman

tensor and are allowed in parallel polarization configurations such as z(xx)$\bar{z}$ and suppressed in crossed or perpendicular configurations such as z(xy)$\bar{z}$. On the other hand, the $E_1$(TO) mode has an off-diagonal Raman tensor and, by symmetry, is allowed in the perpendicular configuration (z(xy)$\bar{z}$) and forbidden in the parallel configuration (z(xx)$\bar{z}$).

However, the unexpected enhancement of the $E_1$(TO) mode in the parallel configuration may be due to several experimental factors. First, the effects of the high numerical aperture (NA), which is due to the focusing cone of the microscope objective lens, create a range of incident angles such that the electric field vector is no longer perfectly aligned with the optical axis. This can result in polarization mixing and partial excitation of theoretically forbidden modes. Also, heavy doping could bring about local distortions in the structure that result in relaxation of symmetry restrictions and activation of phonon modes forbidden otherwise. Other factors, such as polarization leakage or misalignment of the crystal relative to its crystallographic axes, can also lead to violations of the selection rules.

These effects have been recognized in previous research as sources of deviation from ideal polarization-dependent behavior in Raman spectroscopy, especially in doped semiconductor or high-NA systems.[135, 136].

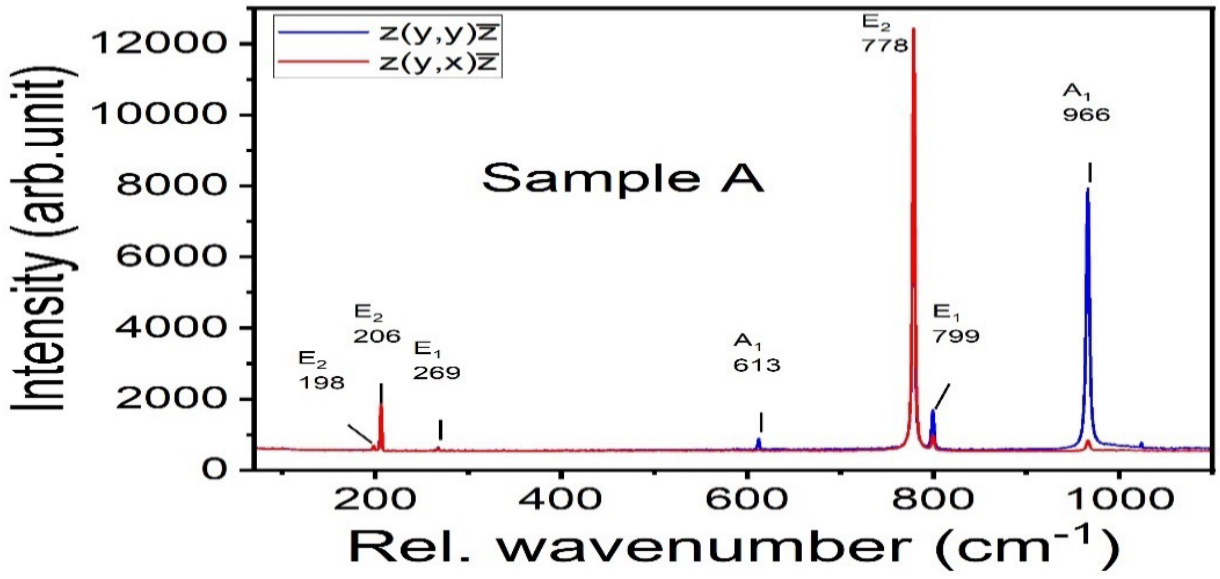

*Figure 6.2 Raman spectrum of Sample A under parallel (z(xx)$\bar{z}$) and perpendicular (z(xy)$\bar{z}$) polarization configurations.*

Figures 6.3b–o show Raman depth scan images for sample A, including three different phonon modes: $E_2$(TO), $E_1$(TO), and $A_1$(LO), with parallel and perpendicular polarization configurations. These scans allow for the analysis of the phonon behavior in the doped epitaxial layer and undoped substrate regions.

The $E_2$(TO) mode, which is nonpolar and does not couple to free carriers, is used as a reference. Its Raman intensity remains relatively uniform in both the epitaxial and substrate regions and in all configurations. This uniformity indicates that the measurement system is stable and that the observed variations in the other modes are due to physical modifications such as doping, rather than to instrument errors.

In contrast, the $A_1$(LO) mode exhibits a significant intensity difference between the epitaxial layer and the substrate. The bright region in the epilayer is clearly visible, while the substrate is dark. This effect is explained by the Froulich interaction—the long-range coupling between LO phonons and free carriers. With increasing doping, the frequency of the LO mode shifts to higher values (blueshifts), and since the Raman measurement is set to the frequency value corresponding to the undoped material (~966 $cm^{-1}$), this shift appears as a change in relative intensity: the epilayer appears brighter, while the substrate signal is weaker. This is a visual indication of the phonon frequency changes and carrier concentration.

A more subtle effect is observed in the $E_1$(TO) mode. Although this mode is considered to be symmetrically forbidden in the parallel polarization configuration, it appears with considerable intensity in the epilayer and is even stronger than in the perpendicular configuration. This finding suggests that the symmetry selection rules are not fully preserved, and this may be due to finite numerical aperture (NA), crystal misalignment, or polarization leakage in the instrument. In Raman systems with high numerical aperture, the angular spread of the laser beam after passing

through the lens can cause partial depolarization, resulting in a deviation of the polarization state at the sample surface from the ideal. These effects, which have been reported in previous papers [137-139], can make the "forbidden" modes weakly observable. Also, the enhanced intensity of the $E_1$(TO) mode in the epilayer, observable in the parallel configuration, indicates the possibility of a frequency shift due to doping. However, this shift is smaller than that observed for the $A_1$(LO) mode. This behavior challenges the conventional assumption that TO phonons are insensitive to doping. However, recent theoretical work [133] suggests that short-range interactions such as deformation potential coupling or local cladding effects can cause observable coupling between TO phonons and free carriers under certain conditions.

Altogether, these results provide a better understanding of electron–phonon interactions in polar semiconductors. While LO phonon–plasmon coupling remains the dominant mechanism, our results suggest that $E_1$(TO) mode in anisotropic crystals such as 4H–SiC, can exhibit doping sensitivity. This result is strengthened in the following sections by detailed spectral analyses.

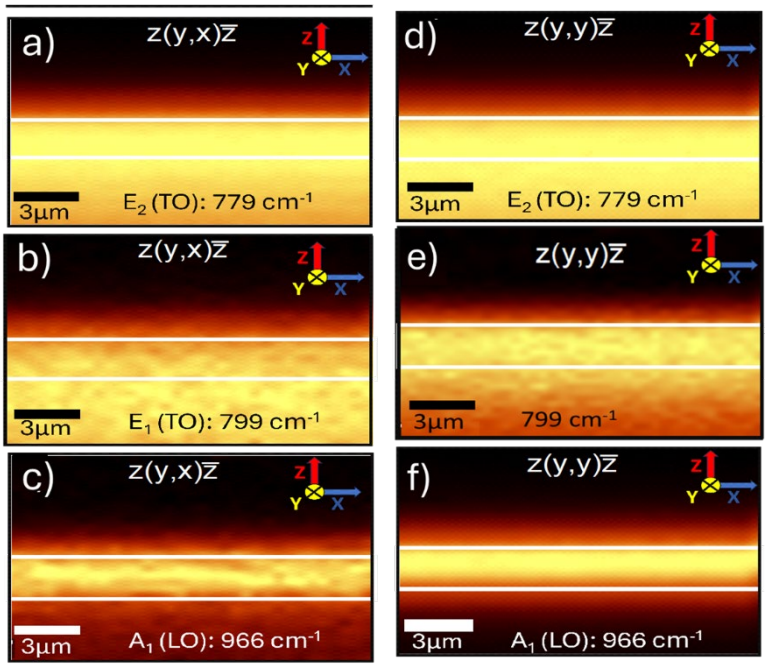

*Figure 6.3* ***Raman depth scans of sample A.*** *(a–f) Depth-resolved Raman images of the $E_2$(TO), $E_1$(TO), and $A_1$(LO) modes under parallel and perpendicular polarizations. $E_2$(TO) shows uniform intensity in both epilayer and substrate, serving as a reference. $A_1$(LO) exhibits strong epilayer–substrate contrast due to LO–plasmon coupling. The $E_1$(TO) mode, while weakly visible in parallel polarization due to relaxed selection rules, shows enhanced intensity in the epilayer, consistent with coupling of TO phonons to free carriers.*

To complement the polarization-resolved depth scan results, Figures 6.4a-f show the Raman spectra of the $E_1$(TO), $E_2$(TO), and $A_1$(LO) modes in both parallel and perpendicular polarization configurations in six samples with different n-type doping concentrations. These spectra reveal several important trends. First, the $E_2$(TO) phonon mode, which arises from vibrations of the center of the nonpolar region, does not show a significant change with increasing doping. This stability is to be expected, since the $E_2$(TO) modes are not coupled to electric fields or free carriers and can therefore be used as a reliable internal reference for assessing spectral changes in other modes.

In contrast, the $E_1$(TO) mode clearly shows a downward shift in wavenumbers (redshift) with increasing doping concentration. This effect is particularly prominent in the parallel polarization configuration, although this mode is theoretically forbidden under ideal symmetry conditions in this configuration. This observed shift supports the hypothesis of weak coupling between transverse optical phonons and free carriers, a phenomenon that is usually not considered in the conventional Frelich theory. The data also show that short-range interaction mechanisms, such as deformation potential coupling or carrier screening effects, become more important at higher doping concentrations.

On the other hand, the $A_1$(LO) mode exhibits an upward shift (blue shift), accompanied by spectral broadening and a decrease in intensity with increasing doping. These changes are consistent with the LO phonon–plasmon coupling (LOPC) theory. As the free carrier density increases, the longitudinal optical phonon couples to the plasmon, forming hybrid phonon–plasmon modes. This coupling leads to a blue shift of the LO-like branch ($\omega_+$) as the plasma frequency increases with

doping. The spectral broadening is due to plasmon damping, such as Landau damping, which reduces the phonon lifetime. At the same time, the decrease in spectral intensity probably reflects the redistribution of spectral weight, strengthening of the screening effect, and increased scattering losses, which reduce the Raman cross section.

These spectral changes not only confirm the polarization-resolved imaging results in Figs. 6.2a–f, but also provide valuable quantitative insights into the reconstruction of phonon modes in 4H–SiC under different doping conditions. In particular, the observed shift in the $E_1$(TO) mode reinforces the need to revise conventional models of the interaction of transverse phonons with carriers in polar semiconductors.

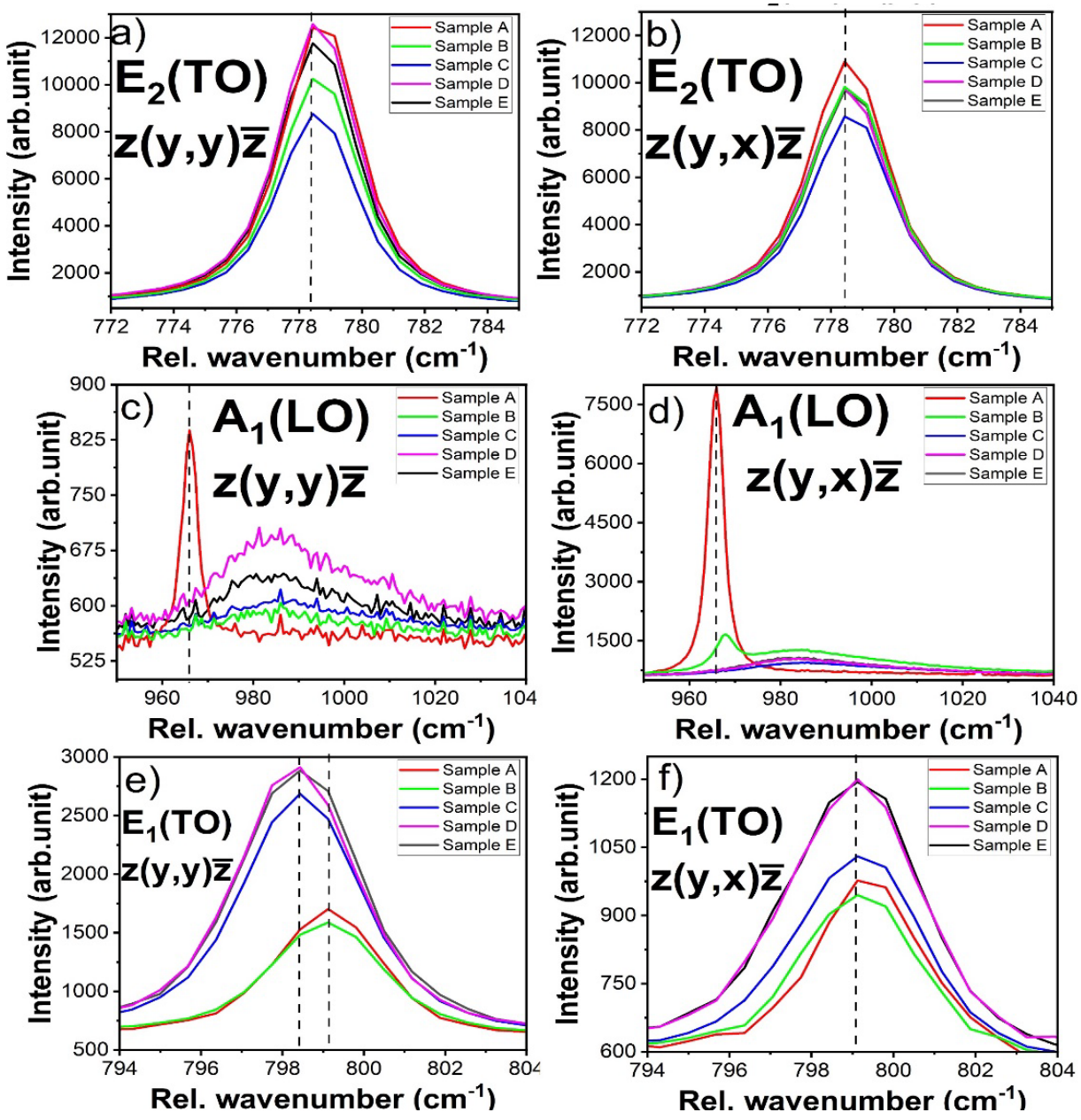


*Figure 6.4* ***Raman spectra of phonon modes versus doping concentration.*** *(a–f) Raman spectra of the $E_1$(TO), $E_2$(TO), and $A_1$(LO) modes in parallel and perpendicular polarizations for six n-type 4H–SiC samples with doping concentrations listed in Table 1.*

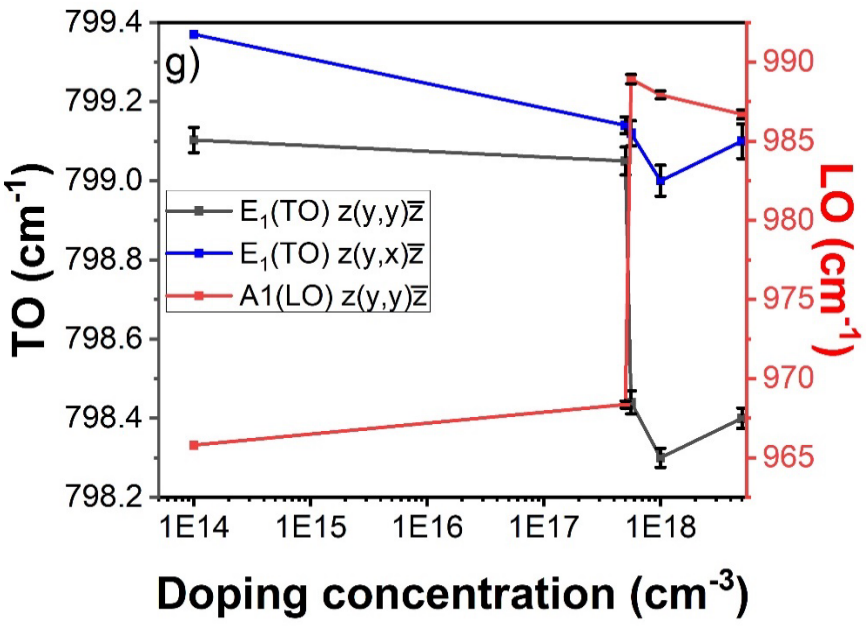


*Figure 6.5* ***Doping dependence of Raman peak positions.*** *Peak positions of the $A_1$(LO) and $E_1$(TO) modes as a function of n-type doping concentration, extracted from Lorentzian fits of the spectra of six samples shown in Figure 6.5.*

Figure 6.5 shows the shift of the Raman peak positions of the $A_1$(LO) and $E_1$(TO) phonon modes as a function of doping concentration. These values are extracted from the spectra of six samples with different levels of n-type doping. The data points show the peak positions obtained by Lorentzian fitting, and the error bars indicate the uncertainty in determining these peaks. The red curve shows the behavior of the $A_1$(LO) mode in the parallel polarization configuration (z(y,y)$\bar{z}$). With increasing doping concentration, this mode exhibits a clear blue shift, consistent with the LO phonon–plasmon coupling (LOPC) theory. This blue shift reflects the formation of hybrid phonon–plasmon modes, such that the LO-like branch ($\omega_+$) moves to higher frequencies with increasing carrier density and thus plasma frequency.

The black and blue curves represent the $E_1$(TO) mode in the parallel ($z(y,y)\bar{z}$) and perpendicular ($z(y,x)\bar{z}$) polarization configurations, respectively. In the parallel polarization configuration, the $E_1$(TO) peak shows a systematic redshift with increasing doping. This result confirms that the TO mode may be affected by the weak electron-phonon interaction under certain conditions, which is in conflict with the Frolich theory. This result agrees with previous experimental results and is supported with a recent theoretical paper by Macheda et al [133]. Unlike the parallel configuration, the frequency of the $E_1$(TO) mode in the perpendicular polarization remains relatively constant across all doping concentrations. This stability indicates that in a symmetry-allowed geometry, the $E_1$(TO) mode is less affected by doping-related effects. Any displacement shifts observed in the forbidden configurations may be due to factors such as symmetry breaking, polarization leakage, or numerical aperture (NA) effects in the optical system. These results highlight the generally different behavior of each phonon mode in different polarization configurations and doping conditions, and provide valuable insight into electron–phonon interactions of each mode in 4H–SiC.

In a series of complementary experiments, we further examined phonon behavior in undoped 4H–SiC samples patterned with surface gratings. This study expands on our previous work [140], which demonstrated that nanoscale surface structuring, particularly parabolic gratings, can cause localized charge buildup even without intentional doping. These surface-accumulated charges have a significant impact on the Raman response by creating localized electric fields. To further investigate this effect, Raman depth scans were performed using unpolarized excitation on nanostructured SiC samples.

The resulting Raman maps, shown in Figure 6.6, revealed a spatially non-uniform phonon distribution, with bright and dark areas varying depending on the selected wavenumber. These patterns correlate with expected charge accumulation sites dictated by the grating topography, confirming that the surface-induced electrostatic potential acts analogously to doping. Specifically, consistent with the results of the previous section, we find that the $A_1$(LO) mode exhibits increasing intensity (brightening) in regions of higher charge density as the wavenumber shifts upward (blue

shift), in agreement with LO–plasmon coupling. Meanwhile, the $E_1$(TO) mode shows enhanced intensity in charge-accumulated regions as the wavenumber shifts downward (red shift), providing further evidence that TO phonons in SiC can couple to free carriers under conditions of strong local field modulation.

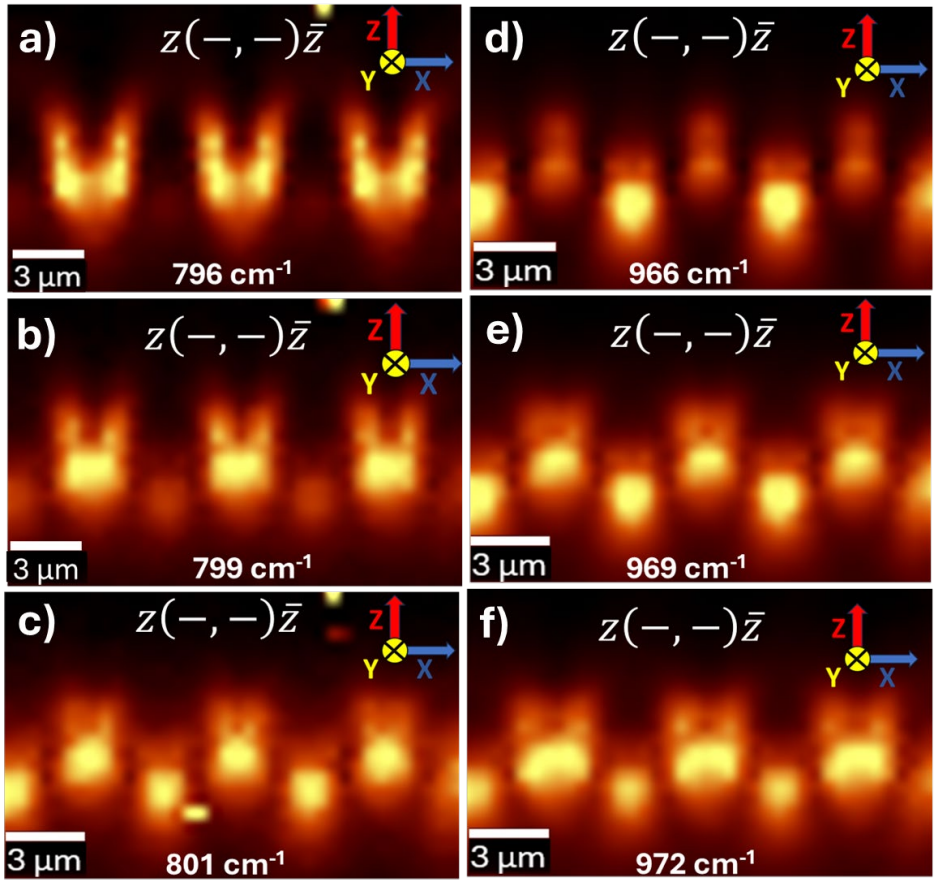


*Figure 6.6* ***Raman depth scans of 1D-grating SiC.*** *Depth-resolved maps of $A_1$(LO) and $E_1$(TO) modes at selected wavenumbers. Brightness increases at the grating crests, with $A_1$(LO) intensifying at higher wavenumbers and $E_1$(TO) at lower wavenumbers, consistent with charge accumulation and TO–carrier coupling.*

Altogether, these results provide further experimental evidence that the $E_1$(TO) mode in 4H–SiC couples to free carriers, in contrast to the conventional expectation that only LO phonons participate in carrier–phonon interactions. The grating-induced charge distribution thus serves as an independent confirmation of TO–carrier coupling, complementing the doping-dependent measurements presented earlier.

In this work, through a series of different experiments, we demonstrate that the $E_1$(TO) mode in 4H–SiC couples to free carriers—a result that contrasts with the traditional expectation that TO phonons are insensitive to carrier interactions. This finding not only advances the understanding of electron–phonon coupling in polar semiconductors but also suggests a practical application: the $E_1$(TO) mode can serve as a non-destructive probe for very high carrier densities, where the $A_1$(LO) mode becomes strongly broadened and thus less reliable for analysis.

# Chapter 7

# Conclusion and future works

In conclusion, this thesis has reviewed the physics of phonon polaritons in 4H-SiC through a combination of experimental and theoretical studies. Despite significant advances in understanding these excitations, there are still opportunities to improve the mapping, control, and understanding of the behavior of phonon polaritons in complex nanostructures. In this work, we employed Raman spectroscopy, nanofabrication, and modeling to investigate how localized and traveling surface phonon polaritons (SPhPs) can be mapped, manipulated, and coupled to other excitations.

Chapter 4 addresses these opportunities by demonstrating the three-dimensional mapping of phonon polariton modes in Indium Phosphide nanopillars and one-dimensional gratings of 4H-SiC using visible and near-infrared confocal Raman microscopy. This mapping is enabled by the coupling of bulk phonon modes to surface phonon polaritons through changes in local polarizability, as described by Raman selection rules. For the $A_1$(LO) and $E_1$(TO) modes in 4H-SiC, coupling to free carriers was also observed, consistent with the well-known longitudinal optical phonon coupling (LOPC) effect. These results provide a method to visualize not only phonon polariton eigenmodes but also the light–matter interactions between phonons, polaritons, and charge distributions, extending the physics of phonon polaritons to shorter wavelengths below 5 μm and offering promising applications in chemical sensing, nonlinear optics, and studies of anisotropic materials.

Chapter 5 presented the first experimental and theoretical evidence of traveling SPhPs in a one-dimensional 4H-SiC grating. These traveling modes can be used in mid-infrared nanophotonic applications, particularly for data transmission and the miniaturization of photonic circuits. Finite element method simulations support the experimental findings, showing clear near-field

propagation of the traveling modes. Raman measurements combined with phonon distribution analysis confirm the existence of both localized and traveling modes with distinct phonon distributions. By tuning the grating parameters, the propagation length and confinement of these modes can be controlled, so that propagation lengths can go beyond 150 μm, representing a significant advance in the field.

The final section investigates the coupling between transverse optical phonons (TO) and free carriers in doped 4H-SiC epitaxial films. For the $E_1$(TO) mode, a systematic frequency shift with increasing carrier concentration was observed. This reveals a behavior of electron–phonon interactions that was not previously expected, which provides deeper insight into light–matter interactions at the nanoscale.

In summary, these results advance our understanding of SPhPs in polar dielectrics in areas such as 3D mapping of localized states, control of propagating states, and investigation of carrier–phonon interactions. The ability to visualize, manipulate, and tune these modes opens new ways for the design of low-loss and functional nanophotonic systems with applications in mid-infrared sensing, optical communications, and quantum photonics.

## Future work

This dissertation has advanced the study of surface phonon-polaritons (SPhPs) in SiC nanostructures and their potential for mid-infrared photonic applications. Despite these contributions, there are still many opportunities for further theoretical and experimental research to deepen our understanding, improve device performance, and broaden their applications. Continuing this research could deepen our understanding of the dynamics of SPhPs, improve device performance, and expand their application in areas such as sensing and integrated photonics.

In Chapter 5, the existence of a traveling mode supported by a one-dimensional SiC lattice was demonstrated. As a suggestion for future research, a detailed theoretical investigation can be carried out to determine how much the propagation length of this traveling mode can be increased by optimizing the lattice parameters. Tuning parameters such as lattice period, width, and height can have a significant impact on the achievable propagation distance. Furthermore, since the required experimental setup for measuring the propagation length was not available during this dissertation, establishing the necessary instruments to directly measure the propagation length of the traveling mode in 1D SiC gratings will be an important step toward experimental validation.

Another promising direction is to demonstrate a waveguide-like structure based on the same 1D grating platform as shown in Figure 7.1. Such a structure can confine the traveling surface phonon polariton (SPhP) mode and guide light along a defined path. Ongoing work in our group is focused on exploring how thin such waveguides can be fabricated, aiming to determine the minimum width that still supports efficient light guiding. In addition to the width, the design of these waveguides also incorporates the gap between adjacent structures, as illustrated in Fig. 7.1. A key direction is to study how variations in both the waveguide width and the inter-waveguide gap influence the traveling SPhP mode and its propagation length. Understanding these dependencies is important not only for optimizing waveguide performance but also for extending this design toward practical applications in integrated optical circuitry.

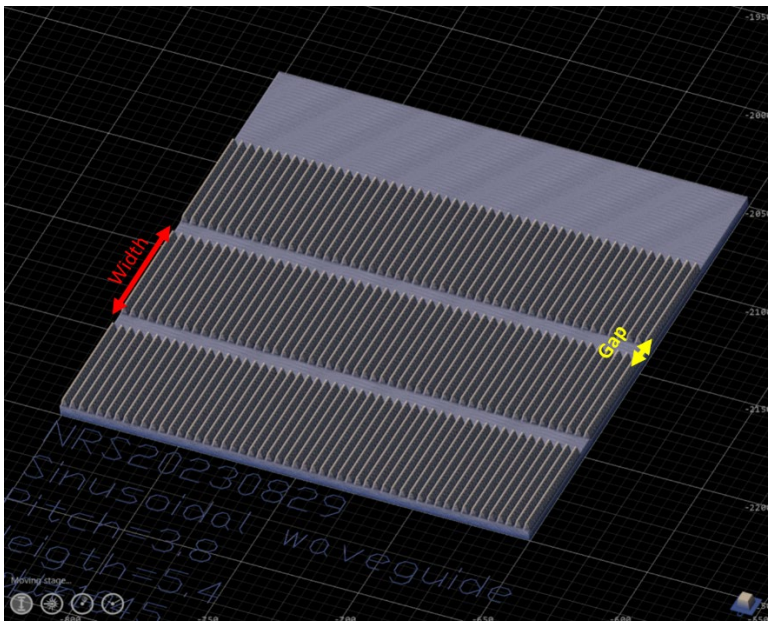


*Figure 7.1 1D SiC waveguide showing the width (red) and gap (yellow) parameters.*

In Chapter 4, Raman mapping was used to visualize the distribution of SPhP modes within the SiC substrate. However, this method was not applied to study the enhanced fields outside the nanostructured surface. As a future research direction, placing an additional polar dielectric material with phonon resonances on top of the nanostructured substrate can provide a platform to probe and map the field distribution outside the base material. Such an approach could reveal the enhancement of phonon modes extending beyond the grating, offering new opportunities for mid-IR chemical sensing applications where the interaction of evanescent fields with analytes is crucial.

# References


1. Novotny, L. and B. Hecht, *Principles of nano-optics*. 2006, Cambridge ; New York: Cambridge University Press. xvii, 539 p.
2. Altug, H., et al., *Advances and applications of nanophotonic biosensors.* Nature Nanotechnology, 2022. **17**(1): p. 5-16.
3. Yu, N.F. and F. Capasso, *Flat optics with designer metasurfaces.* Nature Materials, 2014. **13**(2): p. 139-150.
4. Gansel, J.K., et al., *Gold Helix Photonic Metamaterial as Broadband Circular Polarizer.* Science, 2009. **325**(5947): p. 1513-1515.
5. Karim, F., T.B. Smith, and C.L. Zhao, *Review of optical detection of single molecules beyond the diffraction and diffusion limit using plasmonic nanostructures.* Journal of Nanophotonics, 2018. **12**(1).
6. Mivelle, M., et al., *Nanophotonic Approaches for Nanoscale Imaging and Single-Molecule Detection at Ultrahigh Concentrations.* Microscopy Research and Technique, 2014. **77**(7): p. 537-545.
7. Andersen, U.L., *Photonic chip brings optical quantum computers a step closer.* Nature, 2021. **591**(7848): p. 40-41.
8. Menabde, S.G., et al., *Real-space imaging of acoustic plasmons in large-area graphene grown by chemical vapor deposition.* Nature Communications, 2021. **12**(1).
9. Folland, T.G., et al., *Probing polaritons in the mid- to far-infrared.* Journal of Applied Physics, 2019. **125**(19).
10. Maier, S.A., *Plasmonics: fundamentals and applications*. 2007, New York, U.S.A: Springer Science & Business Media.
11. Ritchie, R.H., et al., *Surface-Plasmon Resonance Effect in Grating Diffraction.* Physical Review Letters, 1968. **21**(22): p. 1530-&.
12. Shi, H.F., et al., *Beam manipulating by metallic nano-slits with variant widths.* Optics Express, 2005. **13**(18): p. 6815-6820.

13. Rawashdeh, A., et al., *High-Quality Surface Plasmon Polaritons in Large-Area Sodium Nanostructures.* Nano Letters, 2023. **23**(2): p. 469-475.

14. Aftab, M., et al., *Surface Plasmon Excitation: Theory, Configurations, and Applications.* Plasmonics, 2024. **19**(4): p. 1701-1719.

15. Khurgin, J.B. and A. Boltasseva, *Reflecting upon the losses in plasmonics and metamaterials.* Mrs Bulletin, 2012. **37**(8): p. 768-779.

16. Khurgin, J.B. and G. Sun, *In search of the elusive lossless metal.* Applied Physics Letters, 2010. **96**(18).

17. Khurgin, J.B. and G. Sun, *Scaling of losses with size and wavelength in nanoplasmonics and metamaterials.* Applied Physics Letters, 2011. **99**(21).

18. Caldwell, J.D., et al., *Low-loss, infrared and terahertz nanophotonics using surface phonon polaritons.* Nanophotonics, 2015. **4**(1): p. 44-68.

19. Foteinopoulou, S., et al., *Phonon-polaritonics: enabling powerful capabilities for infrared photonics.* Nanophotonics, 2019. **8**(12): p. 2129-2175.

20. Peter Y. Yu , M.C., *Fundamentals of semiconductors: physics and materials properties*. 1999, New York, NY: Springer.

21. Caldwell, J.D., et al., *Low-Loss, Extreme Subdiffraction Photon Confinement via Silicon Carbide Localized Surface Phonon Polariton Resonators.* Nano Letters, 2013. **13**(8): p. 3690-3697.

22. Wang, T., et al., *Optical Properties of Single Infrared Resonant Circular Microcavities for Surface Phonon Polaritons.* Nano Letters, 2013. **13**(11): p. 5051-5055.

23. Chen, Y.G., et al., *Spectral Tuning of Localized Surface Phonon Polariton Resonators for Low-Loss Mid-IR Applications.* Acs Photonics, 2014. **1**(8): p. 718-724.

24. Ashraf, H., *Investigation of the Symmetries of the Phonons in 4H and 6H-SiC by Infrared Absorption and Raman Spectroscopy.* 2005.

25. Castelletto, S., et al., *Silicon Carbide Photonics Bridging Quantum Technology.* Acs Photonics, 2022. **9**(5): p. 1434-1457.

26. M. Werner, G.K., H. Möller, M. Eickhoff, P. Gluche, M. Adamschik, C. Johnston, P.R. Chalker, *High-temperature sensors based on SiC and diamond technology.* 1999: p. 141–190.

27. Soo, M.T., K.Y. Cheong, and A.F.M. Noor, *Advances of SiC-based MOS capacitor hydrogen sensors for harsh environment applications.* Sensors and Actuators B-Chemical, 2010. **151**(1): p. 39-55.

28. D. N. MIRLIN, V.M.A., and D. L. MILLS, *Modern problems in condensed matter sciences*. 1982, North-Holland Pub. Co. : Sole distributors for the USA and Canada, Elsevier Science Pub. Co: Amsterdam ; New York. p. volumes : illustrations.

29. Maier, S., *Plasmonics: Fundamentals and Applications*. 2007, Springer.

30. I.F.Almog, M.S.B., andV.Bulovic *The Lorentz Oscillator and its Applications.*

31. Otto, A., *Excitation of nonradiative surface plasma waves in silver by the method of frustrated total reflection.* Zeitschrift f¨ur Physik A Hadrons and nuclei, 1968.

32. Maradudin, A.A., et al., *Modern plasmonics*. Handbook of Surface Science Volume 4. 2014, Burlington: Elsevier Science.

33. Schuller, J.A., et al., *Plasmonics for extreme light concentration and manipulation (vol 9, pg 193, 2010).* Nature Materials, 2010. **9**(4).

34. Loewen, E.G. and E. Popov, *Diffraction gratings and applications*. Optical engineering 58. 1997, New York: Marcel Dekker.

35. Liu, W., et al., *Specialty optical fibers and 2D materials for sensitivity enhancement of fiber optic SPR sensors: A review.* Optics and Laser Technology, 2022. **152**.

36. Mancini, A., *Surface Phonon Polaritons in Silicon Carbide Nanostructures Revealed by Near-field Imaging and Spectroscopy*. 2023: München, Ludwig-Maximilians-Universität.

37. Brenner, S.C. and L.R. Scott, *The mathematical theory of finite element methods*. 3rd ed. Texts in applied mathematics. 2008, New York, NY: Springer. xvii, 397 p.

38. Kohlmann, M., *Grating Coupling To Surface Phonon Polaritons*, in *Department of Physics Technische Universit¨at Berlin*. 2018.

39. Kittel, C., *Solid state physics*. Vol. 3. 1955: Shell Development Company Emeryville.

40. Smith, E., et al., *Modern Raman Spectroscopy : A Practical Approach*. 2005, Hoboken: Wiley.

41. Brüesch, P., *Phonons : theory and experiments*. Springer series in solid-state sciences 34. 1982, Berlin ; New York: Springer-Verlag. 1 v. : ill.

42. Cardona, M., *Fundamental Reflectivity Spectrum of Semiconductors with Zinc-Blende Structure.* Journal of Applied Physics, 1961. **32**: p. 2151-&.

43. Albrecht, A.C., *On the theory of Raman intensities.* The Journal of chemical physics, 1961. **34**(5): p. 1476-1484.

44. Long, D.A., *The Raman effect : a unified treatment of the theory of Raman scattering by molecules*. 1st ed. 2002, Chichester ; New York: Wiley.

45. Sharac, N., G. Iyer, and J. Tischler. *3D-printed infrared metamaterials*. in *Quantum Sensing and Nano Electronics and Photonics XVI*. 2019. SPIE.

46. Khurgin, J.B., *How to deal with the loss in plasmonics and metamaterials.* Nature Nanotechnology, 2015. **10**(1): p. 2-6.

47. Ellis, C.T., et al., *Aspect-ratio driven evolution of high-order resonant modes and near-field distributions in localized surface phonon polariton nanostructures.* Scientific Reports, 2016. **6**.

48. Dunkelberger, A.D., et al., *Active tuning of surface phonon polariton resonances via carrier photoinjection.* Nature Photonics, 2018. **12**(1): p. 50-+.

49. Spann, B.T., et al., *Photoinduced tunability of the reststrahlen band in 4*

*-SiC.* Physical Review B, 2016. **93**(8).

50. Brar, V.W., et al., *Hybrid Surface-Phonon-Plasmon Polariton Modes in Graphene/Monolayer h-BN Heterostructures.* Nano Letters, 2014. **14**(7): p. 3876-3880.

51. Lu, G.Y., et al., *Engineering the Spectral and Spatial Dispersion of Thermal Emission via Polariton-Phonon Strong Coupling.* Nano Letters, 2021. **21**(4): p. 1831-1838.

52. Li, D.H., et al., *Hybridized Exciton-Photon-Phonon States in a Transition Metal Dichalcogenide van der Waals Heterostructure Microcavity.* Physical Review Letters, 2022. **128**(8).

53. Qian, C.J., et al., *Coupling of MoS2 Excitons with Lattice Phonons and Cavity Vibrational Phonons in Hybrid Nanobeam Cavities.* Physical Review Letters, 2023. **130**(12).

54. To, Q., et al., *Surface plasmon-phonon-magnon polariton in a topological insulator-antiferromagnetic bilayer structure.* Physical Review Materials, 2022. **6**(8).

55. Neuner, B., et al., *Midinfrared Index Sensing of pL-Scale Analytes Based on Surface Phonon Polaritons in Silicon Carbide.* Journal of Physical Chemistry C, 2010. **114**(16): p. 7489-7491.

56. Li, P.N., et al., *Infrared hyperbolic metasurface based on nanostructured van der Waals materials.* Science, 2018. **359**(6378): p. 892-+.

57. Taubner, T., et al., *Near-field microscopy through a SiC superlens.* Science, 2006. **313**(5793): p. 1595-1595.

58. Razdolski, I., et al., *Resonant Enhancement of Second-Harmonic Generation in the Mid-Infrared Using Localized Surface Phonon Polaritons in Subdiffractional Nanostructures.* Nano Letters, 2016. **16**(11): p. 6954-6959.

59. Lu, Y., et al., *Giant enhancement of THz-frequency optical nonlinearity by phonon polariton in ionic crystals.* Nature Communications, 2021. **12**(1).

60. Mancini, A., et al., *Near-Field Spectroscopy of Cylindrical Phonon-Polariton Antennas.* Acs Nano, 2020. **14**(7): p. 8508-8517.

61. Gubbin, C.R.a.D.L., Simone and Folland, Thomas G, *Surface phonon polaritons for infrared optoelectronics.* AIP Publishing, 2022. **131**.

62. Gubbin, C.R., et al., *Hybrid longitudinal-transverse phonon polaritons.* Nature Communications, 2019. **10**.

63. Hajian, H., et al., *Tailoring far-infrared surface plasmon polaritons of a single-layer graphene using plasmon-phonon hybridization in graphene-LiF heterostructures.* Scientific Reports, 2018. **8**.

64. Beechem, T.E., et al., *Influence of spatial dispersion on spectral tuning of phonon-polaritons.* Physical Review B, 2019. **100**(20).
65. Ocelic, N. and R. Hillenbrand, *Subwavelength-scale tailoring of surface phonon polaritons by focused ion-beam implantation.* Nature Materials, 2004. **3**(9): p. 606-609.
66. Li, P.N., et al., *Hyperbolic phonon-polaritons in boron nitride for near-field optical imaging and focusing.* Nature Communications, 2015. **6**.
67. Krivanek, O.L., et al., *Vibrational spectroscopy in the electron microscope.* Nature, 2014. **514**(7521): p. 209-+.
68. Lagos, M.J., et al., *Mapping vibrational surface and bulk modes in a single nanocube.* Nature, 2017. **543**(7646): p. 529-+.
69. Li, X.Y., et al., *Three-dimensional vectorial imaging of surface phonon polaritons.* Science, 2021. **371**(6536): p. 1364-+.
70. Jin, C.H., et al., *Interlayer electron-phonon coupling in WSe*

*/hBN heterostructures.* Nature Physics, 2017. **13**(2): p. 127-131.
71. Chow, C.M., et al., *Unusual Exciton-Phonon Interactions at van der Waals Engineered Interfaces.* Nano Letters, 2017. **17**(2): p. 1194-1199.
72. Viner, J.J.S., et al., *Insights into hyperbolic phonon polaritons in*

*-BN using Raman scattering from encapsulated transition metal dichalcogenide layers.* Physical Review B, 2021. **104**(16).
73. Bergeron, A., et al., *Probing hyperbolic and surface phonon-polaritons in 2D materials using Raman spectroscopy.* Nature Communications, 2023. **14**(1).
74. Steele, J.A., P. Puech, and R.A. Lewis, *Polarized Raman backscattering selection rules for (*

*)-oriented diamond- and zincblende-type crystals.* Journal of Applied Physics, 2016. **120**(5).
75. Hohenester, U., *Nano and Quantum Optics.* Graduate Texts in Physics, 2020.
76. Lourenço-Martins, H. and M. Kociak, *Vibrational Surface Electron-Energy-Loss Spectroscopy Probes Confined Surface-Phonon Modes.* Physical Review X, 2017. **7**(4).

77. Lagos, M.J., et al., *Excitation of long-wavelength surface optical vibrational modes in films, cubes and film/cube composite system using an atom-sized electron beam.* Microscopy, 2018. **67**.

78. Frizyuk, K., et al., *Enhancement of Raman scattering in dielectric nanostructures with electric and magnetic Mie resonances.* Physical Review B, 2018. **97**(8).

79. Sirleto, L., A. Vergara, and M.A. Ferrara, *Advances in stimulated Raman scattering in nanostructures.* Advances in Optics and Photonics, 2017. **9**(1): p. 169-217.

80. Zhang, Q., et al., *Exciton-phonon coupling in individual ZnTe nanorods studied by resonant Raman spectroscopy.* Physical Review B, 2012. **85**(8).

81. Ivanov, V.G., et al., *Phonon and magnon Raman scattering in CuB*

*O.* Physical Review B, 2013. **88**(9).

82. Dmitriev, P.A., et al., *Resonant Raman scattering from silicon nanoparticles enhanced by magnetic response.* Nanoscale, 2016. **8**(18): p. 9721-9726.

83. Nakashima, S., et al., *Determination of free carrier density in the low doping regime of 4*

*-SiC by Raman scattering.* Applied Physics Letters, 2008. **93**(12).

84. Thiel, M., et al., *Direct laser writing of three-dimensional submicron structures using a continuous-wave laser at 532 nm.* Applied Physics Letters, 2010. **97**(22).

85. Marty, R., et al., *Charge distribution induced inside complex plasmonic nanoparticles.* Optics Express, 2010. **18**(3): p. 3035-3044.

86. Baffou, G., C. Girard, and R. Quidant, *Mapping Heat Origin in Plasmonic Structures.* Physical Review Letters, 2010. **104**(13).

87. Qi, R.S., et al., *Probing Far-Infrared Surface Phonon Polaritons in Semiconductor Nanostructures at Nanoscale.* Nano Letters, 2019. **19**(8): p. 5070-5076.

88. Hauer, R., et al., *Tomographic Reconstruction of Quasistatic Surface Polariton Fields.* Acs Photonics, 2022.

89. Alexander M Dubrovkin, B.Q., Harish NS Krishnamoorthy, Nikolay I Zheludev, and Qi Jie Wang, *Ultraconfined surface phonon polaritons in molecular layers of van der waals dielectrics.* Nature communications, 2018.

90. Yu PY, C.M., *Fundamentals of semiconductors: physics and materials properties.* New York, NY: Springer, 1999.

91. Bohren CF, H.D., *Absorption and scattering of light by small particles.* John Wiley & Sons, 2008.

92. Bosman, M., et al., *Surface Plasmon Damping Quantified with an Electron Nanoprobe.* Scientific Reports, 2013. **3**.

93. Rephaeli, E., A. Raman, and S.H. Fan, *Ultrabroadband Photonic Structures To Achieve High-Performance Daytime Radiative Cooling.* Nano Letters, 2013. **13**(4): p. 1457-1461.

94. Atwater, H.A. and A. Polman, *Plasmonics for improved photovoltaic devices (vol 9, pg 205, 2010).* Nature Materials, 2010. **9**(10): p. 865-865.

95. Ahn, S., E. Hwang, and H. Min, *Inelastic carrier lifetime in a coupled graphene/electron-phonon system: Role of plasmon-phonon coupling.* Physical Review B, 2014. **90**(24): p. 245436.

96. Li, Y.H., et al., *Manipulation of surface phonon polaritons in SiC nanorods.* Science Bulletin, 2020. **65**(10): p. 820-826.

97. Gubbin, C.R., S.A. Maier, and S. De Liberato, *Theoretical investigation of phonon polaritons in SiC micropillar resonators.* Physical Review B, 2017. **95**(3).

98. Baron, A., et al., *Compact Antenna for Efficient and Unidirectional Launching and Decoupling of Surface Plasmons.* Nano Letters, 2011. **11**(10): p. 4207-4212.

99. López-Tejeira, F., et al., *Efficient unidirectional nanoslit couplers for surface plasmons.* Nature Physics, 2007. **3**(5): p. 324-328.

100. Liu, J.S.Q., et al., *A submicron plasmonic dichroic splitter.* Nature Communications, 2011. **2**.

101. Liu, Y.M., et al., *Compact Magnetic Antennas for Directional Excitation of Surface Plasmons.* Nano Letters, 2012. **12**(9): p. 4853-4858.

102. Yoxall, E., et al., *Direct observation of ultraslow hyperbolic polariton propagation with negative phase velocity.* Nature Photonics, 2015. **9**(10): p. 674-+.
103. Breslin, V.M., et al., *Hyperbolic phonon polariton resonances in calcite nanopillars.* Optics Express, 2021. **29**(8): p. 11760-11772.
104. Caldwell, J.D., et al., *Sub-diffractional volume-confined polaritons in the natural hyperbolic material hexagonal boron nitride.* Nature Communications, 2014. **5**.
105. Teran-Garcia, E., et al., *Real-Space Visualization of Canalized Ray Polaritons in a Single Van der Waals Thin Slab.* Nano Lett, 2025. **25**(6): p. 2203-2209.
106. Taboada-Gutiérrez, J., et al., *Broad spectral tuning of ultra-low-loss polaritons in a van der Waals crystal by intercalation.* Nature Materials, 2020. **19**(9): p. 964-+.
107. Ambrosio, A., et al., *Selective excitation and imaging of ultraslow phonon polaritons in thin hexagonal boron nitride crystals.* Light-Science & Applications, 2018. **7**.
108. Jiang, Y.Y., et al., *Group-Velocity-Controlled and Gate-Tunable Directional Excitation of Polaritons in Graphene-Boron Nitride Heterostructures.* Laser & Photonics Reviews, 2018. **12**(5).
109. Ciattoni, A., et al., *Polariton excitation in epsilon-near-zero slabs: Transient trapping of slow light.* Physical Review A, 2013. **87**(5).
110. Engheta, N., *Circuits with light at nanoscales: optical nanocircuits inspired by metamaterials.* Science, 2007. **317**(5845): p. 1698-702.
111. Alù, A. and N. Engheta, *Tuning the scattering response of optical nanoantennas with nanocircuit loads.* Nature Photonics, 2008. **2**(5): p. 307-310.
112. Dai, S., et al., *Subdiffractional focusing and guiding of polaritonic rays in a natural hyperbolic material.* Nature Communications, 2015. **6**.
113. Basov, D.N., M.M. Fogler, and F.J.G. de Abajo, *Polaritons in van der Waals materials.* Science, 2016. **354**(6309).
114. Hu, G.W., et al., *Phonon Polaritons and Hyperbolic Response in van der Waals Materials.* Advanced Optical Materials, 2020. **8**(5).

115. Arledge, K.E., Chase T. Ellis, Nazli Rasouli Sarabi, Vincent R. Whiteside, Chul Soo Kim, Mijin Kim, Daniel C. Ratchford, Michael A. Meeker, Binbin Weng, and Joseph G. Tischler, *Mapping phonon polaritons with visible light.* 2024.

116. Caglayan, H., et al., *Near-Infrared Metatronic Nanocircuits by Design.* Physical Review Letters, 2013. **111**(7).

117. Iqbal, T., *Propagation length of surface plasmon polaritons excited by a 1D plasmonic grating.* Current Applied Physics, 2015. **15**(11): p. 1445-1452.

118. N. Sharac, G.R.S.I., J. G. Tischler, *3D Printed Infrared Metamaterials.* Quantum Sensing and Nano Electronics and Photonics XVI. Vol. 10926. SPIE, 2019, 2019. **10926**.

119. Shi, F.L., et al., *Pseudospin-polarized slow light waveguides with large delay-bandwidth product.* Communications Physics, 2024. **7**(1).

120. Ginsberg, N.S., S.R. Garner, and L.V. Hau, *Coherent control of optical information with matter wave dynamics.* Nature, 2007. **445**(7128): p. 623-626.

121. Giustino, F., *Electron-phonon interactions from first principles.* Reviews of Modern Physics, 2017. **89**(1).

122. Quan, Y.J., S.Y. Yue, and B.L. Liao, *Impact of Electron-Phonon Interaction on Thermal Transport: A Review.* Nanoscale and Microscale Thermophysical Engineering, 2021. **25**(2): p. 73-90.

123. Chernikov, A., et al., *Phonon-assisted luminescence of polar semiconductors: Frohlich coupling versus deformation-potential scattering.* Physical Review B, 2012. **85**(3).

124. Burton, J.C., et al., *Spatial characterization of doped SiC wafers by Raman spectroscopy.* Journal of Applied Physics, 1998. **84**(11): p. 6268-6273.

125. Chakraborty, B., et al., *Symmetry-dependent phonon renormalization in monolayer MoS*

*transistor.* Physical Review B, 2012. **85**(16).

126. Falkovsky, L.A., *Electron-phonon interaction and coupled phonon-plasmon modes.* Journal of Experimental and Theoretical Physics, 2003. **97**(4): p. 794-805.

127. Burstein, E., A. Pinczuk, and S. Iwasa, *Raman Scattering by Coupled Plasmon-Longitudinal-Optical-Phonon Modes in Zincblende-Type Crystals.* Physical Review, 1967. **157**(3): p. 611-&.

128. Olego, D. and M. Cardona, *Raman-Scattering by Coupled Lo-Phonon Plasmon Modes and Forbidden to-Phonon Raman-Scattering in Heavily Doped P-Type Gaas.* Physical Review B, 1981. **24**(12): p. 7217-7232.

129. Ding, K., et al., *Longitudinal optical phonon-plasmon coupled modes of degenerate Al-doped ZnO films.* Applied Physics Letters, 2012. **101**(3).

130. Frohlich, H., *Electrons in Lattice Fields.* Advances in Physics, 1954. **3**(11): p. 325-&.

131. Verdi, C. and F. Giustino, *Frohlich Electron-Phonon Vertex from First Principles.* Physical Review Letters, 2015. **115**(17).

132. Yuasa, T., et al., *Raman scattering from coupled plasmon-LO-phonon modes in n-type AlxGa1-xAs.* Phys Rev B Condens Matter, 1986. **33**(2): p. 1222-1232.

133. Macheda, F., P. Barone, and F. Mauri, *Electron-Phonon Interaction and Longitudinal-Transverse Phonon Splitting in Doped Semiconductors.* Physical Review Letters, 2022. **129**(18).

134. Mooradian, A. and G.B. Wright, *Observation of the Interaction of Plasmons with Longitudinal Optical Phonons in GaAs.* Physical Review Letters, 1966. **16**(22): p. 999-1001.

135. Tuschel, D., *Molecular Spectroscopy Workbench The Effect of Microscope Objectives on the Raman Spectra of Crystals.* Spectroscopy, 2017. **32**(9): p. 14-23.

136. Adar, F., *Raman Polarization Measurements: Keeping Track of the Instrumental Components' Behavior.* Spectroscopy, 2017. **32**(2): p. 14-22.

137. Froehlicher, G. and S. Berciaud, *Raman spectroscopy of electrochemically gated graphene transistors: Geometrical capacitance, electron-phonon, electron-electron, and electron-defect scattering.* Physical Review B, 2015. **91**(20).

138. Bremard, C., et al., *The Effect of High-Numerical-Aperture Objectives on Polarization Measurements in Micro-Raman Spectrometry.* Applied Spectroscopy, 1985. **39**(6): p. 1036-1039.

139. Deb, S.K., M.L. Bansal, and A.P. Roy, *Calculation of Error in Depolarization Ratio Measurement Due to Finite Collection Angle in Laser Raman-Spectroscopy.* Applied Spectroscopy, 1984. **38**(4): p. 500-504.
140. Arledge, K.E., et al., *Mapping Phonon Polaritons with Visible Light.* arXiv preprint arXiv:2404.13759, 2024.